

---


Electronic Theses and Dissertations, 2004-2019

---

2006

## Direct Nonlinear Optics Measurements Of Raman Gain In Bulk Glasses And Estimates Of Fiber Performance

Robert Stegeman  
*University of Central Florida*

 Part of the [Electromagnetics and Photonics Commons](#), and the [Optics Commons](#)  
Find similar works at: <https://stars.library.ucf.edu/etd>  
University of Central Florida Libraries <http://library.ucf.edu>

This Doctoral Dissertation (Open Access) is brought to you for free and open access by STARS. It has been accepted for inclusion in Electronic Theses and Dissertations, 2004-2019 by an authorized administrator of STARS. For more information, please contact [STARS@ucf.edu](mailto:STARS@ucf.edu).

---

### STARS Citation

Stegeman, Robert, "Direct Nonlinear Optics Measurements Of Raman Gain In Bulk Glasses And Estimates Of Fiber Performance" (2006). *Electronic Theses and Dissertations, 2004-2019*. 907.  
<https://stars.library.ucf.edu/etd/907>

DIRECT NONLINEAR OPTICS MEASUREMENTS OF RAMAN GAIN IN  
BULK GLASSES AND ESTIMATES OF FIBER PERFORMANCE

by

ROBERT ANTHONY MICHAEL STEGEMAN

B.S. University of Florida, 2000  
M.S. University of Central Florida, 2003

A dissertation submitted in partial fulfillment of the requirements  
for the degree of Doctor of Philosophy  
in the Department of Optics  
in the College of Optics and Photonics  
at the University of Central Florida  
Orlando, Florida

Spring Term  
2006

Major Professor: Peter Delfyett Jr.

© 2006 Robert A. Stegeman

## ABSTRACT

The need for more bandwidth in communications has stimulated the search for new fiberizable materials with properties superior to fused silica which is the current state-of-the-art. One of the key properties is Raman gain by which a pump beam amplifies a signal beam of longer wavelength. An apparatus capable of directly measuring the spectral dependence and absolute magnitude of the material Raman gain coefficient using nonlinear optics techniques has been built. Using radiation from a 1064 nm Nd:YAG laser as the pump and from a tunable Optical Parametric Generator and Amplifier as the signal, the Raman gain spectrum was measured for different families of glass samples with millimeter thickness.

A number of glass families were investigated. Tellurites with added oxides of tungsten, niobium, and thallium produced the largest Raman gain coefficients of any oxide family reported to date, typically 30-50 times higher than that of fused silica. On the other hand, phosphate families were found with spectrally broad Raman gain response, 5 times broader than fused silica and flat to  $\pm 3$ dB over the full spectral range in some compositions. Although the chalcogenides were found to photodamage easily, coefficients 50 - 80 times that of fused silica were measured.

Finally, a numerical study was undertaken to predict the theoretical performance and noise properties of tellurite fibers for communications. Included in the computer modeling were linear loss; the interaction among multiple pumps and signals; forward and/or backward propagating pump beams; forward, backward and double Rayleigh scattering; noise properties of amplifiers; excess noise, etc. This led to a comparison of the optical signal-to-noise characteristics for Raman gain in a tellurite versus a silica fiber.

*To: Dedicated to my family, especially the man I have the honor of calling my advisor and Dad.*

## ACKNOWLEDGMENTS

There are many people who have made this thesis possible, through both scientific collaborations and contributions as well as spiritual and emotional support. It has been an amazing journey to be part of this project and have my name on publications with great names in nonlinear optics and glass science.

My committee has been wonderful in their support and patience in finding dates and times to assemble for the necessary formalities in achieving this degree. I am thankful for having advisors who initially marched me in the right direction, but also allowed me to “play” in areas that interested me once the sails were set.

My research partner, Dr. Clara Rivero, deserves her own space in this section. Her ability to bring me up to date on understanding the developments in glass science and her perpetual abundance of energy and excitement surrounding this work makes it an absolute pleasure to have worked with her. We made a great team, productive in our research and our ability to publish quality results and emphatically convince the rest of the community that we know what we are doing in our labs.

Dr. Peter Delfyett – I owe you one. You let me try things in the lab and gave me the right direction to guide my program. Sharing your enthusiasm for science is something that others have to experience to believe!

Dr. Kathleen Richardson fueled my desire to fully understand some of the mystery behind the magic of glass science. My growing understanding of the successful marriage between materials and devices is owed in large part to her.

This work would not have been possible without collaboration with Dr. Thierry Cardinal and Dr. Philippe Thomas in France to obtain tellurite samples for this project. Very nice scientific samples were consistently available for characterization at CREOL. Laetitia Petit and her students also provided several samples which are discussed in the thesis.

Dr. Roger Stolen afforded me the opportunity to visit and participate in his research while at Virginia Tech. It was very instrumental to view a working fiber drawing tower and work with his students on attempts to fabricate high Raman gain fibers.

Dr. George Stegeman, whom I also have the pleasure of calling Dad, has once again proven his merits in this project. His vision of making Raman gain measurements on bulk samples was proven a reality in his labs. The ability to make wise suggestions and provide the occasional shot in the arm during slow times enabled a lot of hard work to pay off in the form of this thesis. On a higher level, his patience, organization, and tenacity have been a great example of how to deal with stubborn, arrogant, and misguided UCF officials – thank God CREOL and its employees does not fall into this category.

John Hitt, you have some incompetent people under your wings that you need to consider cleansing from UCF. Unwittingly, perhaps unknowingly, you leave me little choice but to bring it to the attention of the general public. The time to level the playing field is now.

On the personal side, my family and friends have been sources of immense comfort and reassurance during this journey. The tenacity and resourcefulness of my brother, John, during my struggle with UCF officials has been a wonderful surprise. David Morgan deserves special mention for his help in the lab and his ability to bring my mind away from my work every so often.

The end of this journey signifies the beginning of new one back “home” in Tucson.

## TABLE OF CONTENTS

LIST OF FIGURES .....	x
LIST OF TABLES .....	xvi
LIST OF ACRONYMS/ABBREVIATIONS .....	xvii
CHAPTER ONE: INTRODUCTION.....	1
CHAPTER TWO: THEORETICAL CONSIDERATIONS OF RAMAN GAIN AND RAMAN SCATTERING.....	10
2.1    Theory of Raman Gain and Spontaneous Raman Scattering: Single Raman Active Species .....	11
2.1.1    Raman Gain .....	14
2.1.2    Spontaneous Raman Scattering.....	19
2.1.3    Inhomogeneously Broadened Line Shapes.....	21
2.1.4    Summary: Single Raman Active Species .....	23
2.2    Raman Physics in Multi-component Glasses.....	25
CHAPTER THREE: EXPERIMENTAL APPARATUS, MEASUREMENT TECHNIQUES AND DATA ANALYSIS .....	31
3.1    Raman Gain: Finite Cross-section Beams and Pulsed Fields .....	31
3.2    Description of the Experimental Apparatus.....	35
3.3    Raman Gain Measurements and Data Analysis.....	44
3.4    Application to Fused Silica and Multi-component Glasses.....	46



CHAPTER FOUR: RAMAN GAIN MEASUREMENT OF PHOSPHATE AND CHALGONIDE GLASSES .....	48
4.1 Borophosphate Raman Gain Data.....	49
4.2 Binary Phosphate-Niobate Raman Gain Data.....	52
4.3 Cation Exchange Phosphate Raman Gain Data .....	55
4.4 Raman Gain Data on Broadband Phosphates for Attempts Towards Spectrally Flattened Gain Profiles .....	59
4.5 Raman Gain Measurements of Chalcogenide Glasses.....	63
CHAPTER FIVE: RAMAN GAIN MEASUREMENTS IN TELLURITE GLASSES.....	68
5.1 Raman Gain Measurements of Binary Tellurium-Thallium Oxide Glass .....	69
5.2 Raman Gain Measurements of Tellurite Glass with Ternary Lewis $ns^2$ Lone Pair Electrons .....	73
5.3 Raman Gain Measurements of Tellurite Glasses with Lewis $ns^2$ Lone Pair Electrons and $d^0$ Ions of $Ti^{4+}$ , $Nb^{5+}$ , and $W^{6+}$ .....	78
5.4 Raman Gain Measurements of Tellurite Glass with $d^0$ Ions.....	83
5.5 “The Controversy” .....	85
CHAPTER SIX: TELLURITE FIBER PERFORMANCE - NUMERICAL ANALYSIS .....	96
6.1 Background and Theory.....	96
6.2 Application of Numerical Model .....	107
6.3 Considerations for Fiber Design Parameters .....	116
CHAPTER SEVEN: SUMMARY AND CONCLUSIONS .....	117
7.1 Instrumentation Development.....	117
7.2 Broadband Glasses.....	117

7.3	Chalcogenide Glasses .....	118
7.4	Tellurite Glasses.....	119
7.5	Numerical Simulations.....	121
7.6	Suggestions for the Future .....	121
APPENDIX A: COMPUTER CODE USED IN CHAPTER 6 .....		123
LIST OF REFERENCES.....		135

## LIST OF FIGURES

Figure 1.1.	Telecommunication bandwidth available for erbium doped fiber and silica fiber amplifiers and the available bandwidth possible with the new "AllWave" fibers.....	1
Figure 1.2.	Schematic of Raman gain in which a pump photon (dark blue) is stimulated by incident signal photons (red) to break up into a additional signal photons and an optical phonon (green) in a Raman active medium (light blue) .....	3
Figure 1.3.	Upper, schematic of a uniform Raman gain spectrum. Middle, input signals (red arrows). Lower, amplified signals by the Raman gain spectrum in the upper figure .....	3
Figure 1.4.	Raman gain spectrum of fused silica for a pump wavelength of 1064 nm [11] .....	5
Figure 2.1.	Schematic representation of the stimulated Raman (gain) process (left) and 90°-geometry spontaneous Raman scattering process (right).....	12
Figure 2.2.	The Raman gain response versus the frequency shift from the pump wave.....	18
Figure 2.3.	Example of the absorption spectrum of the compound $85\text{TeO}_2 - 15\text{WO}_3$ which shows the tails of the absorption edge due to different component species extending different distances into the visible part of the spectrum. The locations of three important pump wavelengths are also indicated .....	30
Figure 3.1.	Pump and probe beam interactions in Raman gain measurements. The Rayleigh range of the probe beam is 1.4 cm at the longest wavelengths tested, which enables a plane wave approximation in millimeter thick bulk samples .....	34
Figure 3.2.	Major equipment used in experimental apparatus for Raman gain measurements. A detailed explanation is given in the text.....	35

Figures 3.3 (a) & (b). Autocorrelation traces of the 1064 nm pump beam with (a) LiNbO <sub>3</sub> crystal and (b) KTP crystal .....	36
Figures 3.4 (a) – (h). Spectra obtained from the OPG/OPA .....	39
Figures 3.5 (a) – (f). Autocorrelations of OPG/OPA pulses with a slight frequency chirp.....	40
Figure 3.6. Pulse width variation as a function of wavelength from OPG/OPA .....	40
Figure 3.7. Raman gain spectrum of 3.18 mm thick pure fused silica sample.....	47
Figure 4.1. Optical band edge for the borophosphate family .....	50
Figure 4.2 (a) – (c). Raman gain spectrum of borophosphate compositions of [(100 - x)NaPO <sub>3</sub> - xNa <sub>2</sub> B <sub>4</sub> O <sub>7</sub> ]:TiO <sub>2</sub> /Nb <sub>2</sub> O <sub>5</sub> = 1 where (a) x = 13, (b) x = 10, and (c) x = 5%. Overlaid are the spontaneous Raman spectrum taken at 632.8 nm. Values for TiO <sub>2</sub> and Nb <sub>2</sub> O <sub>5</sub> are 5% mol for this glass family.....	51
Figure 4.3. Wavelength dependence of the absorption coefficient of the binary phosphate-niobate family .....	53
Figures 4.4 (a) - (d). Raman gain spectra of the binary phosphate niobate glasses with increasing niobate content. The spontaneous Raman spectra were taken at 514.5 nm and were overlaid over and normalized to the Raman gain data.....	54
Figure 4.5. Absorption band edge of cation exchange glasses with compositions given in the legend of the figure .....	56
Figures 4.6 (a) – (e). Raman gain of spectra of (a) 14.9Na <sub>2</sub> O – 29.8CaO – 29.8P <sub>2</sub> O <sub>5</sub> – 25.5Nb <sub>2</sub> O <sub>5</sub> , (b) 14.9Na <sub>2</sub> O – 29.8BaO – 29.8P <sub>2</sub> O <sub>5</sub> – 25.5Nb <sub>2</sub> O <sub>5</sub> , (c) 35Na <sub>2</sub> O – 35P <sub>2</sub> O <sub>5</sub> – 30Nb <sub>2</sub> O <sub>5</sub> , (d) 17.5Na <sub>2</sub> O – 17.5K <sub>2</sub> O – 30Nb <sub>2</sub> O <sub>5</sub> , and (e) 35K <sub>2</sub> O – 35P <sub>2</sub> O <sub>5</sub> – 30Nb <sub>2</sub> O <sub>5</sub> .....	57

Figure 4.7.	Raman active modes of various binary phosphate glasses. 80NaPO <sub>3</sub> – 20Sb <sub>2</sub> O <sub>3</sub> (black line) displays the desired Raman active mode near $\Delta\nu = 13 - 15$ THz. The spontaneous Raman was data taken with a 633 nm pump wavelength .....	60
Figure 4.8.	Absorption band edge of borophosphate glass with constant Sb <sub>2</sub> O <sub>3</sub> content and increasing TiO <sub>2</sub> and Nb <sub>2</sub> O <sub>5</sub> content .....	61
Figures 4.9 (a) & (b).	Raman gain curves of (a) 45[85NaPO <sub>3</sub> – 4.5Na <sub>2</sub> B <sub>4</sub> O <sub>7</sub> – 10.5Na <sub>2</sub> O] – 20TiO <sub>2</sub> – 20Nb <sub>2</sub> O <sub>5</sub> – 15Sb <sub>2</sub> O <sub>3</sub> and (b) 55[95NaPO <sub>3</sub> – 5Na <sub>2</sub> B <sub>4</sub> O <sub>7</sub> ] – 15TiO <sub>2</sub> – 15Nb <sub>2</sub> O <sub>5</sub> – 15Sb <sub>2</sub> O <sub>3</sub> . The spontaneous Raman spectrum obtained with a pump wavelength of 633 nm is overlaid for comparison .....	62
Figure 4.10.	Apparatus used for Raman gain measurements on bulk glass samples .....	64
Figures 4.11 (a) & (b).	(a) Absorption spectrum and (b) the Raman gain curve of 18Ge – 5Ga – 7Sb – 70S. The spontaneous Raman data was obtained at 633 nm and is normalized to the peak of the measured Raman gain spectrum using 1064 nm pumping.....	66
Figures 4.12 (a) – (d).	The pulsed 1064 nm incident pump is plotted versus the transmitted signal energy in chalcogenide samples with (a) 70S, (b) 50S – 20Se, (c) 20S – 50Se, and (d) 70Se. The photodarkening effect clearly takes place as the heavier selenium atoms replace the sulfur atoms in the glass network.....	67
Figure 5.1.	Absorption spectra of a series of binary TeO <sub>2</sub> – TlO <sub>0.5</sub> glasses.....	70
Figure 5.2.	Raman gain data points for the $\Delta\nu = 20$ THz and $\Delta\nu = 21.3$ THz peaks and absolute spontaneous Raman cross-section taken at 1064 nm overlaid for comparison for 50TeO <sub>2</sub> – 50TlO <sub>0.5</sub> .....	71
Figure 5.3.	Schematic of the Lewis ns <sup>2</sup> lone electron pair in TeO <sub>2</sub> glasses .....	73
Figure 5.4.	Absorption coefficient of three ternary tellurite glasses.....	74

Figures 5.5 (a) - (h). Raman gain curves with the spontaneous Raman spectrum overlaid and normalized to the peak of the Raman gain for (a)  $59.5\text{TeO}_2 - 25.5\text{TlO}_{0.5} - 15\text{PbO}$ , (b)  $63\text{TeO}_2 - 27\text{TlO}_{0.5} - 10\text{PbO}$ , (c)  $64\text{TeO}_2 - 16\text{TlO}_{0.5} - 20\text{PbO}$ , (d)  $66.5\text{TeO}_2 - 28.5\text{TlO}_{0.5} - 5\text{PbO}$ , (e)  $68\text{TeO}_2 - 17\text{TlO}_{0.5} - 15\text{PbO}$ , (f)  $70\text{TeO}_2 - 10\text{TlO}_{0.5} - 20\text{PbO}$ , (g)  $72\text{TeO}_2 - 18\text{TlO}_{0.5} - 10\text{PbO}$ , and (h)  $85\text{TeO}_2 - 10\text{TlO}_{0.5} - 5\text{PbO}$  ..... 76

Figures 5.6 (a) - (d). Raman gain curves and normalized spontaneous Raman spectra for (a)  $75\text{TeO}_2 - 10\text{TiO}_2 - 15\text{Bi}_2\text{O}_3$ , (b)  $80\text{TeO}_2 - 12.5\text{TiO}_2 - 7.5\text{Bi}_2\text{O}_3$ , (c)  $80\text{TeO}_2 - 10\text{TiO}_2 - 10\text{Bi}_2\text{O}_3$  and (d)  $85\text{TeO}_2 - 10\text{TiO}_2 - 5\text{Bi}_2\text{O}_3$  ..... 79

Figures 5.7 (a) & (b). Raman gain curves of (a)  $75\text{TeO}_2 - 10\text{TiO}_2 - 15\text{Bi}_2\text{O}_3$  and (b)  $75\text{TeO}_2 - 12\text{ZnO} - 5\text{PbO} - 3\text{PbF}_2 - 5\text{Nb}_2\text{O}_5$ . The network resonance near  $\Delta\nu = 13.5$  THz is enhanced by the presence of  $\text{TiO}_2$  for similar amounts of  $\text{TeO}_2$  ..... 80

Figures 5.8 (a) – (e). Raman gain curves with the spontaneous Raman spectrum obtained at 633 nm overlaid and normalized to the peak in the Raman gain curve for (a)  $55\text{TeO}_2 - 40\text{TlO}_{0.5} - 5\text{TiO}_2$ , (b)  $65\text{TeO}_2 - 30\text{TlO}_{0.5} - 5\text{TiO}_2$ , (c)  $75\text{TeO}_2 - 20\text{TlO}_{0.5} - 5\text{TiO}_2$ , (d)  $80\text{TeO}_2 - 10\text{TlO}_{0.5} - 10\text{TiO}_2$ , and (e)  $80\text{TeO}_2 - 5\text{TlO}_{0.5} - 15\text{TiO}_2$  ..... 81

Figures 5.9 (a) – (c). Spontaneous Raman cross-section of binary glasses obtained at 1064 nm and spontaneous Raman data normalized to the peak in the Raman gain spectrum obtained at 1064 nm using direct NLO measurements..... 82

Figures 5.10 (a) – (c). Raman gain spectrum with spontaneous Raman scattering spectrum overlaid and normalized to the peak in the Raman gain spectrum for (a)  $85\text{TeO}_2 - 15\text{WO}_3$ , (b)  $85\text{TeO}_2 - 10\text{Nb}_2\text{O}_5 - 5\text{MgO}$ , and (c)  $90\text{TeO}_2 - 10\text{TiO}_2$ . Raman gain spectrum of fused silica is also overlaid and multiplied by a factor of 10..... 84

Figure 5.11.	VV Polarized Experimental Spontaneous Raman Spectrum of samples W (85TeO <sub>2</sub> – 15WO <sub>3</sub> ) and Nb (85TeO <sub>2</sub> – 10Nb <sub>2</sub> O <sub>5</sub> – 5MgO), normalized to SiO <sub>2</sub> .....	89
Figure 5.12.	VV Polarized Spontaneous Raman Spectrum of samples W and Nb, normalized to SiO <sub>2</sub> . Excitation wavelength 514 nm.....	90
Figure 5.13.	Estimated multi-wavelength Raman gain coefficient at the peak Raman vibration (TeO <sub>4</sub> units at 665 cm <sup>-1</sup> ( $\Delta\nu = 20$ THz)), and W-O vibration (at 920 cm <sup>-1</sup> ( $\Delta\nu = 27.6$ THz)) respectively, normalized to SiO <sub>2</sub> . The dash line is used as a guide to the eye. The solid lines represent the $(n^2(\lambda)-1)^2$ approximation to the dispersion which is clearly inadequate when approaching the electronic band edge.....	91
Figure 5.14.	UV-Vis-NIR absorption spectra of samples W, Nb, and SiO <sub>2</sub> . Notice that 195 nm is the lowest wavelength resolution of the Cary500 Spectrophotometer.....	92
Figure 5.15.	Spontaneous Raman spectra of 85TeO <sub>2</sub> – 15WO <sub>3</sub> obtained at different wavelengths, normalized to the peak Raman gain value at 665 cm <sup>-1</sup> ( $\Delta\nu = 20$ THz), measured with 1064 nm pumping.....	94
Figure 6.1.	Rayleigh scattering of an optical wave due to an imperfection in a waveguide.	102
Figure 6.2.	Rayleigh scattering coefficients for various silica-based FRAs [1].....	103
Figure 6.3.	OSNR due to DRS of the signal at 1550 nm in a silica-based FRA. Circles + dotted line is a 9 km span, Squares + solid line is a 15 km span, triangles denote dual stage span with 9 km in each stage [55].....	105
Figure 6.4.	Theoretical predictions of OSNR in silica core fiber (SCF) and dispersion shifted fiber (DSF) when operated as a FRA [57].....	106
Figure 6.5.	Theoretical (solid lines) and experimental results of OSNR inside SCF and DSF when operated as a FRA for various pump powers [57] .....	107

Figures 6.6 (a) & (b). Loss spectrum and small-signal Raman gain coefficient for composition $78\text{TeO}_2 - 5\text{ZnO} - 12\text{Li}_2\text{O} - 5\text{Bi}_2\text{O}_3$ [25].....	113
Figure 6.7. Theoretical improvement in OSNR of a tellurite FRA vs. silica FRA. Open symbols represent the silica FRA, filled symbols represent the tellurite FRA.....	114
Figure 6.8. Power penalty for different amounts of net Raman gain for tellurite and silica FRAs [25].....	115



## LIST OF TABLES

<b>Table 4.1.</b>	Raman gain coefficients for the three main Raman active vibrations in the NaPO <sub>3</sub> – Nb <sub>2</sub> O <sub>5</sub> glass system .....	55
<b>Table 4.2.</b>	Peak Raman gain coefficient found in the family 18Ge – 5Ga – 7Sb – (70-x)S – xSe with x = 0, 2, and 5% .....	66
<b>Table 5.1.</b>	Raman gain coefficients for binary TeO <sub>2</sub> – TiO <sub>0.5</sub> glass system at Δν = 20 THz and Δν = 21.3 THz and optical surface damage thresholds at 1064 nm .....	72
<b>Table 5.2.</b>	Peak Raman gain coefficients near Δν = 21.3 THz and Δν = 20 THz and surface optical damage thresholds of ternary tellurite glasses with Lewis ns <sup>2</sup> lone pair holders.....	77
<b>Table 5.3.</b>	Main peak Raman gain coefficients and surface optical damage thresholds for ternary Lewis ns <sup>2</sup> and d <sup>0</sup> ion tellurite glasses.....	83
<b>Table 5.4.</b>	Calculated and experimentally measured material Raman gain coefficient with 1064 nm pumping, at the peak Raman resonance at 665 cm <sup>-1</sup> (Δν = 20 THz).....	92
<b>Table 6.1.</b>	Parameters used to obtain OSNR estimates for tellurite and silica FRAs .....	112

## LIST OF ACRONYMS/ABBREVIATIONS

ASE	Amplified spontaneous emission
CCD	Charge Coupled Device (Detector Array)
CW	Continuous wave
CREOL	Center for Research and Education in Optics and Lasers
DRS	Double Raleigh scattering
EDFA	Erbium doped fiber amplifier
EM	Electro-magnetic
FRA	Fiber Raman amplifier
KTP	Potassium Titanyl Phosphate
Nd:YAG	Niodinium:Yittrium Aluminum Garnate
NF	Noise figure
NLO	Nonlinear optics
NTT	Japanese Telephone Company
OPG/OPA	Optical Parametric Generator/Optical Parametric Amplifier
OSNR	Optical Signal to Noise Ratio
SHG	Second Harmonic Generation
SNR	Signal to Noise Ratio
$T_g$	Glass Transition Temperature
$T_F$	Glass Fixation Temperature
$T_x$	Crystallization Temperature

## CHAPTER ONE: INTRODUCTION

Modern communications networks are being faced with increasing traffic which doubles approximately every two years. This has put enormous pressure on the communications industry to make available progressively more communications channels. The options being pursued are currently focused on extending the wavelength range available for communications via optical fibers and to find new compression and more efficient coding techniques. For the former approach, one of the recent breakthroughs has been the development of improved fiber fabrication techniques which have eliminated the water absorption band centered near 1400 nm and have therefore opened up the previously available bandwidth from 1460 nm – 1620 nm to now extend from 1260 nm - 1620 nm [1]. The absorption spectrum of this “AllWave” fiber is shown in Figure 1.1.

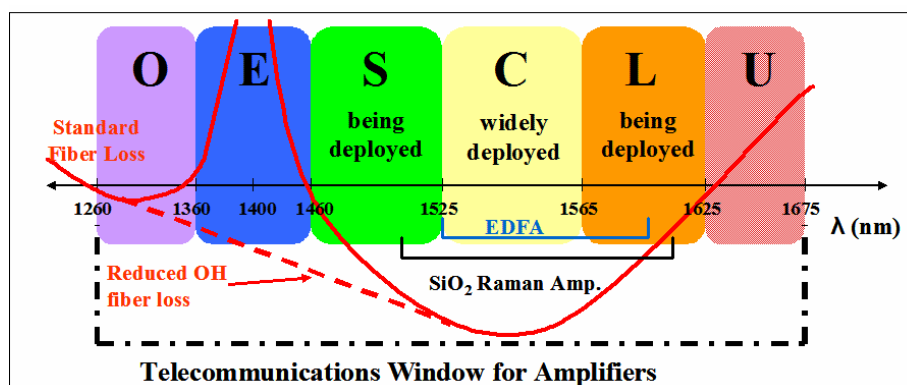


**Figure 1.1.** Telecommunication bandwidth available for erbium doped fiber and silica fiber amplifiers and the available bandwidth possible with the new "AllWave" fibers.

It is clear from Figure 1.1 that the existing amplifiers cover only a small fraction of the available wavelength range. The Erbium Doped Fiber Amplifier (EDFA) only

covers a small fraction of the total wavelength range in the C- and L-bands [2]. The most viable alternative for amplification appears to be Raman gain. This amplification process was first proposed in the early days of fiber optics but its performance characteristics were quickly surpassed by those of EDFAs in the days when bandwidth was not a pressing issue and the EDFA bandwidth was sufficient. Furthermore, the diode laser powers required for pumping EDFAs were significantly less than those required for pumping silica fiber Raman amplifiers, and were a better match to available diode pump lasers. Nevertheless there was a continuing undercurrent of interest in the properties of new glasses which might improve the Raman gain performance by offering higher gains and broader bandwidths than silica fiber to ultimately supplant the EDFAs. There were many pioneering papers by Lines and others who considered various glass families both theoretically and experimentally [3-6]. The understanding of the important glass properties became quite advanced, especially in considering the mechanisms which lead to propagation losses in fibers and enhanced Raman gains [7-8].

In Raman gain, a signal beam is amplified by a pump beam of shorter wavelength as shown in Figure 1.2. The signal beam stimulates a pump photon to split into a signal beam photon and a vibrational excitation (optical phonon), thus amplifying coherently the signal beam [9]. The process involves exciting the vibrational modes of the amplifying medium which take up the energy difference between the pump photons and the signal photons. This excess energy is eventually lost to heat in the medium.

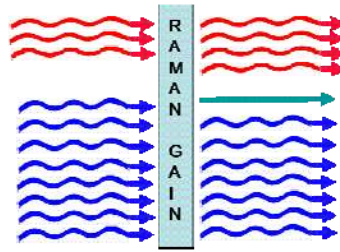


**Figure 1.2.** Schematic of Raman gain in which a pump photon (dark blue) is stimulated by incident signal photons (red) to break up into a additional signal photons and an optical phonon (green) in a Raman active medium (light blue)

In an isolated molecule, dilute gas, or a single crystal, these vibrational modes are spectrally very narrow and hence only signals whose difference in frequency from the pump laser coincided with the vibrational frequency could be amplified. However, in disordered media such as glasses, there is a distribution of the peak vibration frequencies leading to continuous Raman gain spectra. The goal is find a glassy medium in which the material Raman gain coefficient,  $g_{RG}$ , has as large a uniform spectrum as possible so that signals at different frequencies are amplified uniformly as shown in Figure 1.3. The goal is also to make the spectrum as spectrally broad as possible to amplify over as wide a bandwidth,  $\Delta\lambda_{RG}$ , as possible.

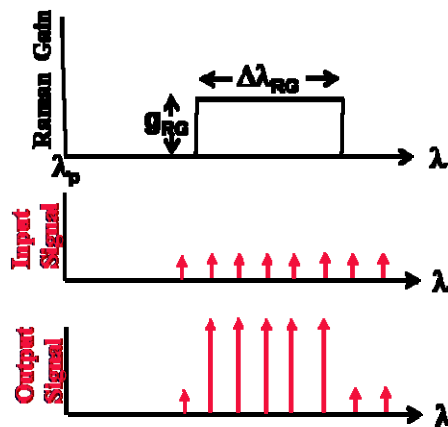


**Figure 1.3.** Upper, schematic of a uniform Raman gain spectrum. Middle, input signals (red arrows). Lower, amplified signals by the Raman gain spectrum in the upper figure

Raman gain has a very important advantage relative to EDFAs. For an EDFA the range of wavelengths that can be amplified is fixed in wavelength to the specific bandwidth of the laser transitions involved as shown in Figure 1.1 [2]. In Raman gain, the pump laser can be put at any convenient wavelength, subject of course to the availability of pump diodes at that wavelength, so that any signal wavelength region can in principle be covered to the extent of the  $\Delta\lambda_{\text{RG}}$  bandwidth. However, even when using Raman gain, it is not possible to cover the whole bandwidth made available by “AllWave” fibers and it will be necessary to use multiple pump wavelengths spaced throughout the wavelength range of signals used. This of course is not possible with EDFAs. Finally, the last advantage of using EDFAs, namely the availability of laser pumps at the required power levels, has been overcome. Diode pump technology has advanced over the years and now the required pumps for Raman gain are readily available [10].

The medium used for Raman gain amplification to date has been fused silica, typically doped with germanium [9]. There are a number of disadvantages to using fused silica and one very important advantage. The peak Raman gain of silica, shifted back to a 1064 nm pump wavelength for easy comparison to the data shown later in this thesis, is  $g_{\text{RG}} = 0.9 \times 10^{-13}$  m/W, very low on the scale of what could be available in glasses in general [11]. Furthermore, as shown below in Figure 1.4, the Raman gain spectrum is dominated by a single peak giving only about 14 THz of useful bandwidth, with a full width half max of this peak lending approximately 5 - 7 THz of bandwidth. It was predicted by Lines that glasses could easily be found with larger Raman gain coefficients and broader spectral widths [3-6]. On the other hand, because the band edge of silica is in the UV region of the spectrum, the propagation losses are very low at communication

wavelengths. In fact, for long haul communications the ratio of  $g_{RG}/\alpha$  is very large for silica where  $\alpha$  is the attenuation coefficient. It is not clear, even now, that the glasses studied here will optimize this figure of merit, principally because the attenuation in glasses is not well known at these wavelengths. Also, for the cases in which absorption has been measured in fibers of new glass compositions, the fiber fabrication techniques were not optimized. Experience with fused silica has shown that it takes a massive effort to truly optimize attenuation.

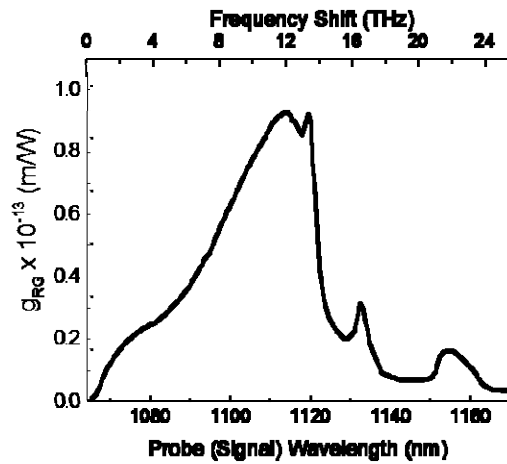


**Figure 1.4.** Raman gain spectrum of fused silica for a pump wavelength of 1064 nm [11]

For the reasons discussed above, interest in new glasses for Raman gain has continued for 25 years and has recently had a rebirth [6,12-21]. During the 1970s and right up to the present time the main characterization technique used to evaluate the Raman gain spectrum was spontaneous Raman scattering. In this method, light is scattered in all directions by thermally excited (“noise”) vibrational modes. The scattered light is gathered over a finite solid angle by collection optics, frequency resolved in a

spectrometer and then detected usually by cooled photomultiplier tubes. Because absolute calibration of such measurements is difficult and prone to many uncertainties, usually a fused silica Raman spectrum is taken under the same experimental conditions and the ratio of a Raman peak in the test glass spectrum to the main silica feature measured is reported [21]. Since the silica spectrum is well-known and understood, and because the corrections to the test spectrum usually involve just the refractive index, this procedure serves to give an estimate of the Raman gain in the test glass. Even this procedure requires great care in application as was found in this work [22].

More accurate is a direct evaluation of the Raman gain, i.e. the injection of a signal into the glass to co-propagate with the pump followed by the measurement of the output signal [23-25]. Given that the magnitude of the material Raman gain coefficients in glasses are small, this is most easily performed with continuous wave lasers in fibers because of the long fiber lengths available. However, this necessitates the fabrication of a fiber and this process is too expensive and time consuming to be repeated many times for studying Raman gain spectra versus details of glass structure and composition for many different glass compositions.

The theory of these characterization processes, spontaneous Raman scattering and direct Raman gain measurement is presented in Chapter 2 in some detail and compared. Discussed first is the single molecule case, next the Raman processes in disordered media, and finally resonant enhancement of both processes.

In Chapter 3 a new technique for directly measuring the absolute value of the Raman gain in millimeter-sized, bulk glass samples will be described [26]. The small values of the typical Raman gain coefficients are compensated for by using high power



pulsed lasers. The details of the apparatus and measurement technique will be described. This apparatus was calibrated against the known spectrum of fused silica shown in Figure 1.4 at the same pump wavelength and agreement was obtained within the experimental uncertainty for both the peak value and the spectral shape.

One of the problems addressed in Chapter 4 is how to broaden the Raman gain bandwidth relative to that of fused silica. This involves choosing glasses without a single dominant Raman line like that observed in fused silica. Preferred are glasses with many Raman lines of comparable magnitude. The most commonly encountered problem is to find glasses with sufficient Raman intensity for frequency shifts between 11 and 15 THz to produce a quasi-uniform broadband gain. The candidate glasses studied were combinations of phosphates and borates with small additions of  $d^0$  ions (via  $\text{TiO}_2$  and  $\text{Nb}_2\text{O}_5$ ).  $\text{Ti}^{4+}$  and  $\text{Nb}^{5+}$  are known as  $d^0$  ions because they have an empty d-shell electron bands - such species exhibit high polarizabilities [27]. Variations on this family were investigated and bandwidths about 5 times that of fused silica were obtained.

Also described in Chapter 4 are Raman gain experiments on chalcogenides. It proved very difficult to get reliable values for such glasses due to light induced damage. Nevertheless, the largest Raman gain found in this work was measured to be 70 times that of fused silica for the glass  $18\text{Ge} - 5\text{Ga} - 7\text{Sb} - 70\text{S}$ . For the other chalcogenide glasses that were investigated, only the peak values of the Raman gain coefficient were able to be measured.

There are good indicators in the theoretical work of Lines as to which glasses are good candidates for superior Raman gain [3-6]. For example, tellurites fall into this category and the investigation of their Raman gain is discussed in Chapter 5. In addition,

there are indications from studies of the third order nonlinear susceptibilities, most specifically measurements of the nonlinear refractive index coefficient  $n_2$  as to which glasses may also exhibit large Raman gain coefficients [28-30]. The rationale is that both processes involve changes in the molecular polarizability. Modern glass science now recognizes that certain additives can enhance a nonlinear response by enhancing the polarizability, both linear and nonlinear. For example, the addition of Lewis  $ns^2$  lone pair electron species such as  $Tl^+$ ,  $Pb^{2+}$ , or  $Bi^{3+}$  and/or  $d^0$  ions such as  $Ti^{4+}$ ,  $Nb^{5+}$ , and  $W^{6+}$  are known to enhance the third order nonlinearity in tellurite glasses [30]. In fact, peak Raman gains up to 50 times that of fused silica were discovered in this thesis in augmented tellurites, the largest found to date and reported in the literature in oxide glasses [18].

Measurements described in Chapter 5 on tellurites and published in Optics Letters created a controversy in the literature [15,22]. Raman scattering measurements with visible lasers on tellurite glasses similar to those evaluated by direct Raman gain reported here at 1064 nm were found in three international laboratories to have Raman gain coefficients approximately twice larger than those reported using the technique described in Chapter 3 [16,20,21]. Many speculations were offered, focused primarily on our technique, despite the fact that we also reported that our measurements on fused silica agreed with the accepted values. This controversy was resolved by showing that the Raman susceptibility is enhanced with visible lasers due to the close proximity of the electronic absorption band edge, also discussed in Chapter 5 [22].

The experimental work in this thesis was done with the close collaboration of Dr. Clara Rivero who fabricated many of the glasses investigated here and also performed the spontaneous Raman scattering measurements quoted frequently in this thesis.

The Raman gain data for a specific tellurite glass was used in Chapter 6 to do numerical simulations of amplification in a tellurite fiber. Included in the computer modeling were linear loss; Raman gain with multiple pumps and signals; forward and/or backward propagating pump beams; forward, backward and double Rayleigh scattering; noise properties of amplifiers; excess noise, etc. This led to a comparison of the optical signal-to-noise ratio for different Raman gains in a tellurite and silica fiber.

The work described in this thesis is summarized in Chapter 7 along with recommendations for further experiments.

## **CHAPTER TWO: THEORETICAL CONSIDERATIONS OF RAMAN GAIN AND RAMAN SCATTERING**

The Raman gain process has been well-known and understood from the early days of nonlinear optics [31]. The Raman gain spectrum is intimately connected to the spontaneous Raman spectrum obtained by scattering from thermally excited optical phonons (vibrational modes) of a material. However, there are fundamental differences between the physics of the Raman gain and the spontaneous Raman scattering processes. In Raman gain, the optical phonons are coherently driven by the mixing of optical fields where-as in spontaneous Raman scattering the phonons arise from noise and hence are uncorrelated [32,33]. These differences primarily impact the case of overlapping vibrational lines frequently encountered in the complex glasses reported recently in the literature. The principle difference occurs near the pump wavelength for the Raman gain where the Raman gain coefficient falls to zero right at the pump frequency. This results in a small difference between the line shapes of the two processes in this vicinity.

To date, the theory of these Raman processes has been focused on single component materials which have a single dominant vibrational mode which couples strongly to light fields. This is the case of fused silica. Furthermore, based on the success found in interpreting the link between the spontaneous Raman process and the Raman gain, very little attention has been paid to the impact on the shape of the Raman spectrum in multi-component glasses when measured near their electronic absorption band edges.

As it is shown in this and Dr. Clara Rivero's thesis, this has led to misinterpretations of how spontaneous Raman spectra must be interpreted under these conditions [34].

In this chapter the theory of spontaneous Raman scattering will be developed in parallel with Raman gain spectroscopy in order to highlight the similarities and differences. With the exception of the inclusion of the Bose-Einstein factor which comes into the spontaneous Raman scattering formulation to take into account the population of the phonon states, the approach used here is completely classical. It will be based on simple harmonic oscillator models for the molecular vibrations. The propagation of light will be treated via the usual solutions to the wave equation. Finally, the coupling of the optical fields to the vibrations will utilize classical mechanics via interaction potentials and forces on normal modes followed by the standard slowly varying phase and amplitude approximations. This approach allows the basic physics to be highlighted and will facilitate the extension of the theory in a simple way to include multi-component media such as the glasses investigated here experimentally using nonlinear optical techniques.

## ***2.1 Theory of Raman Gain and Spontaneous Raman Scattering: Single Raman Active Species***

The two processes by which light interacts with vibrational modes of molecules are shown schematically in Figure 2.1. In the stimulated Raman scattering process which is the origin of Raman gain, two light fields are considered to mix and produce a nonlinear driving force on the normal vibrational modes of the medium. Thus the frequency difference between the optical waves must match those of the vibrational

modes. In the spontaneous Raman scattering case, the phonon modes are generated by “white noise”, random fluctuations in the normal modes of the material and light scatters from these thermally generated vibrations.

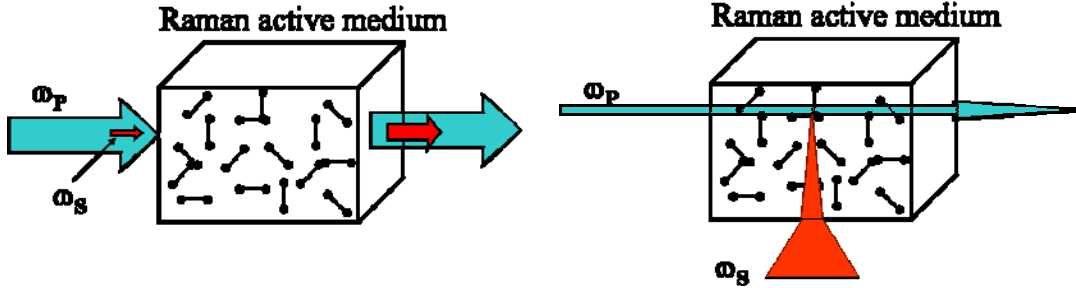


**Figure 2.1.** Schematic representation of the stimulated Raman (gain) process (left) and 90°-geometry spontaneous Raman scattering process (right)

Although in a real experiment all of the beams that interact in the material have finite cross-sections, for simplicity it is assumed in this chapter that the fields are plane waves and are continuous wave in the time domain. In order to get absolute values for the material Raman gain coefficients it is necessary to include the details of the interacting beams and the specific geometry used in both the Raman gain and spontaneous Raman scattering cases. Since the sample sizes in the Raman gain process are only a few millimeters in length, pulsed lasers are needed to achieve the irradiances that are required and for that case the details of the temporal pulses also enter into the problem of obtaining absolute values for the Raman gain coefficient. The inclusion of finite beams and temporal pulses for the Raman gain process will be discussed in Chapter 3.

For the interaction geometry shown in Figure 2.1, the incident (pump) field of frequency  $\omega_p$  and wavevector  $k_p$  is written as

$$E_{pi} = \frac{1}{2} E_{pi} \exp(i\omega_p t - k_p z) + c.c. \quad (2.1)$$

Similarly the Raman signal (or spontaneously scattered) field takes the form

$$E_{si} = \frac{1}{2} E_{si} \exp(i\omega_s t - \vec{k}_s \cdot \vec{r}) + c.c. \quad (2.2)$$

where in this case  $\omega_s$  is the signal (scattered) frequency,  $k_s$  is the signal (scattered) wavevector which lies along the z-axis for Raman gain and, for example, in Figure 2.1 shown for  $90^\circ$  scattering lies along the x-axis. (In actual fact, the spontaneous Raman scattering experiments used in conjunction with the Raman gain measurements were performed in a back scattering geometry.) In the Raman gain case, the gain occurs in the overlap region between two forward traveling, co-propagating beams where-as in the Raman scattering case light is scattered into all directions due to the noise nature of the phonon modes and the scattering volume is defined by the light gathering optics.

Here only the key concepts are discussed and the details of the calculation can be found in textbooks and journal articles [32,33,35,36]. Classically, one can discuss these processes in terms of the effective susceptibilities  $\chi^{(n)}$  used in the usual nonlinear expansions used for describing the nonlinear polarization induced by the light-vibration coupling. In this case this is a third order process, i.e.  $n = 3$ . The alternative is to consider the interaction in terms of a mechanistic model for the light-vibration interaction in single molecules and then extend the result to many molecules. The second option is chosen here because it highlights the fundamental physics that underlies the Raman processes.

Consider first a single Raman-active optical phonon mode with displacement given by

$$q_\beta = \frac{1}{2} Q_\beta \exp[i\Omega_\beta t - \Gamma_\beta t] + c.c. \quad (2.3)$$

where  $\Omega_\beta$  and  $\Gamma_\beta$  are the phonon frequency and the inverse decay constant of the  $\beta$ 'th mode. An excited vibrational mode induces a change in the molecular polarizability  $\alpha$  of the molecule as it modulates the molecular electron “cloud”. This can be written as:

$$\delta\alpha_{ij}^\beta = \frac{\partial\alpha_{ij}^\beta}{\partial q_\beta} \Big|_{q_\beta=0} Q_\beta \quad (2.4)$$

where  $\frac{\partial\alpha_{ij}^\beta}{\partial q_\beta} \Big|_{q_\beta=0}$  is the Raman susceptibility tensor, i.e. it describes the strength of the phonon-light coupling. Note that not all vibrational modes in an isolated molecule modulate the polarizability and for those that do not the Raman susceptibility will be zero. However in disordered media such as glasses, the symmetry relations that govern whether a mode is Raman or infrared active are partially broken so in practice all of the vibrational modes modulate the polarizability to some degree. Usually this coupling due to broken symmetries is quite weak and can be ignored in practice so that only the isolated molecules giving rise to Raman active modes need to be considered.

### 2.1.1 Raman Gain

For Raman gain, the phonon amplitude is given by the mixing of the pump and signal fields, i.e.  $q_\beta \propto E_{pi}E_{si}$  with  $Q_\beta \propto E_{pi}E_{si}^*$ . As a result the phonons are driven at the frequency  $\omega_p - \omega_s = \Omega \cong \Omega_\beta$ .

The starting point of the derivation is the polarization induced in a molecule by a Raman active vibration of amplitude  $q$  and an incident optical field  $E_j$

$$p_i = \left[ \alpha_{ij} + q_\beta \frac{\partial\alpha_{ij}^\beta}{\partial q_\beta} \right] E_j$$



(2.5)

where  $\alpha_{ij}$  is the average polarizability of the molecule in the co-ordinate system defined by the incident light field. Since the media under discussion are disordered media, in this case these polarizabilities, both linear and nonlinear, represent averages over all of the orientations of the molecules. It is of course possible to include the orientation of the individual molecules at the beginning of the formulation and then average over all possible orientations. However, there is nothing to be gained in understanding the processes involved in this case, although it would be rigorously more correct. The nonlinear polarization induced per unit volume with a species density of  $N$  molecules per unit volume is simply written as

$$P_i^{NL} = Nq \frac{\partial \alpha_{ij}^\beta}{\partial q} \Big|_{q=0} E_j. \quad (2.6)$$

From electromagnetic theory and classical mechanics, the interaction potential between the induced polarization and the incident field is given simply by

$$V_{\text{int}} = - \int_0^{E_i} P_i^{NL} dE_i = - \frac{1}{2} q \frac{\partial \alpha_{ij}^\beta}{\partial q} \Big|_{q=0} E_j E_i. \quad (2.7)$$

From classical mechanics, the force driving the normal mode is given by  $F_q = -\partial V_{\text{int}} / \partial q$  so that

$$F_q = \frac{1}{2} \frac{\partial \alpha_{ij}^\beta}{\partial q} \Big|_{q=0} E_j E_i. \quad (2.8)$$

This force excites the vibration via the driven simple harmonic equation

$$\ddot{q}_\beta + \Gamma_\beta \dot{q}_\beta + \Omega_\beta^2 q_\beta = \frac{1}{2m_\beta} \frac{\partial \alpha_{ij}^\beta}{\partial q} \Big|_{q=0} E_j E_i. \quad (2.9)$$

Inserting Equation 2.3 into 2.9 and solving for  $Q_\beta$  yields for the case  $\omega_p - \omega_s = \Omega \cong \Omega_\beta$

$$Q_\beta = \frac{1}{4m_\beta D(\Omega_\beta)} \left. \frac{\partial \alpha_{ij}^\beta}{\partial q} \right|_{q=0} E_j E_i. \quad (2.10)$$

where the resonant denominator is  $D_\beta(\omega_p - \omega_s) = [-(\omega_p - \omega_s)^2 + i\Gamma_\beta(\omega_p - \omega_s) + \Omega_\beta^2]$ .

This last equation means that the vibration is optimally excited when the difference frequency between the two optical fields matches that of the vibrational mode. Substituting for the total field  $E_i = E_{pi} + E_{si}$  into Equation 2.10, then substituting the resulting  $Q_\beta$  into Equation 2.6 and separating the nonlinear polarization terms that oscillate at  $\omega_p$  and  $\omega_s$ ,

$$P^{NL}(\omega_s) = \frac{1}{2} \frac{N_\beta}{8m_\beta D^*(\omega_p - \omega_s)} \left| \left. \frac{\partial \alpha_{ii}^\beta}{\partial q} \right|_{q=0} \right|^2 |E(\omega_p)|^2 E(\omega_s) \exp[i(\omega_s i - k_s z)] + c.c. \quad (2.11)$$

$$P^{NL}(\omega_p) = \frac{1}{2} \frac{N_\beta}{8m_\beta D(\omega_p - \omega_s)} \left| \left. \frac{\partial \alpha_{ii}^\beta}{\partial q} \right|_{q=0} \right|^2 |E(\omega_s)|^2 E(\omega_p) \exp[i(\omega_p i - k_p z)] + c.c. \quad (2.12)$$

for co-polarized pump and signal waves. Here the subscript “ $ii$ ” refers to a single polarization,  $x$  or  $y$ , and a summation over “ $i$ ” is not implied in this case. This is the key result for the nonlinear polarizations. For the case of orthogonally polarized pump and signal waves, the parameter  $\alpha_{ii}^\beta$  is simply replaced by  $\alpha_{ij}^\beta$  where the “ $ij$ ” refer to the orthogonal polarizations. In most glasses this depolarized component is much smaller although it must be corrected for in our experimental geometry to get accurate values for the Raman gain coefficients.

The usual slowly varying phase and amplitude approximation is now applied. For the signal beam this takes the form

$$\frac{d}{dz}E_{\beta}(\omega_s) = i \frac{N_{\beta}\omega_s}{8m_{\beta}n_s n_p c^2 \epsilon_0^2} \left| \frac{\partial \alpha_{ii}^{\beta}}{\partial q_{\beta}} \right|_{q_{\beta}=0}^2 \frac{\Omega_{\beta}^2 - \Omega^2 - i\Omega\Gamma_{\beta}}{(\Omega_{\beta}^2 - \Omega^2)^2 + \Omega^2\Gamma_{\beta}^2} I(\omega_p)E_{\beta}(\omega_s) \quad (2.13a)$$

for the growth of the signal field along the z-axis where  $n_s$  and  $n_p$  are the refractive indices at the frequencies  $\omega_s$  and  $\omega_p$ ,  $\Omega = \omega_p - \omega_s$  and  $E_{\beta}(\omega_s)$  is the field due to the  $\beta$ 'th mode respectively. In a similar fashion, the pump field “growth” (actually depletion) is given by

$$\frac{d}{dz}E_{\beta}(\omega_p) = i \frac{N_{\beta}\omega_p}{8m_{\beta}n_s n_p c^2 \epsilon_0^2} \left| \frac{\partial \alpha_{ii}^{\beta}}{\partial q_{\beta}} \right|_{q_{\beta}=0}^2 \frac{\Omega_{\beta}^2 - \Omega^2 + i\Omega\Gamma_{\beta}}{(\Omega_{\beta}^2 - \Omega^2)^2 + \Omega^2\Gamma_{\beta}^2} I(\omega_s)E_{\beta}(\omega_p) \quad (2.13b)$$

The imaginary part of this equation gives the Raman gain, and the real part the accompanying change in the refractive index. Solving for the imaginary part gives for a propagation distance  $z$

$$E_{\beta}(\omega_s, z) = E(\omega_s, 0) \exp\left[\frac{g_{RG\beta}(\Omega)}{2} I(\omega_p)z\right] \quad (2.14)$$

so that the Raman gain coefficient (defined by  $I_{\beta}(\omega_s, z) = I(\omega_s, 0) \exp[g_{RG\beta} I(\omega_p)z]$ ) has the form

$$g_{RG\beta}(\Omega) = \frac{N_{\beta}\omega_s\pi}{2m_{\beta}n_s n_p c^2 \epsilon_0^2} \left| \frac{\partial \alpha_{ii}^{\beta}}{\partial q_{\beta}} \right|_{q_{\beta}=0}^2 \frac{\Omega\Gamma_{\beta} / 2\pi}{(\Omega_{\beta}^2 - \Omega^2)^2 + \Omega^2\Gamma_{\beta}^2} \quad (2.15)$$

The salient characteristics of Raman gain are now quite clear, i.e.  $g_{RG\beta}(\Omega) > 0$  for  $\Omega > 0$  and  $g_{RG\beta}(\Omega) < 0$  for  $\Omega < 0$ . Therefore amplification only occurs for longer wavelengths than the pump beam. The detailed dependence on  $\Omega$  is shown in Figure 2.2 in the limit  $\Gamma_{\beta} \cong \Omega_{\beta}$  in which the zero in the Raman gain coefficient at  $\Omega = 0$  is obvious.

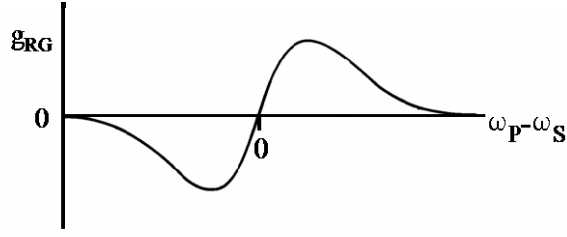


**Figure 2.2.** The Raman gain response versus the frequency shift from the pump wave

In this plane wave analysis the signal beam grows exponentially with distance and the growth rate depends on the *irradiance* of the pump beam, i.e. the phase of the pump beam is not important. Note that absorption of the signal beam occurs for  $\Omega < 0$ . Typically for a single molecule  $\Omega_\beta \gg \Gamma_\beta$  so that the resonant denominator can be written as

$$(\Omega_\beta^2 - \Omega^2)^2 + \Omega^2 \Gamma_\beta^2 \cong (\Omega_\beta + \Omega)^2 (\Omega_\beta - \Omega)^2 + \Omega^2 \Gamma_\beta^2 \cong 4\Omega_\beta^2 [(\Omega_\beta - \Omega)^2 + (\frac{\Gamma_\beta}{2})^2]. \quad (2.16)$$

This now gives for the Raman gain coefficient for  $|\Omega_\beta - \Omega|$  less than a few times  $\Gamma_\beta/2$

$$g_{RG\beta}(\Omega) = \frac{N_\beta \omega_s \pi}{8m_\beta n_s n_p c^2 \epsilon_0^2 \Omega_\beta} \left| \frac{\partial \alpha_\beta}{\partial q_\beta} \right|_{q_\beta=0}^2 \frac{\Gamma_\beta / 2\pi}{(\Omega_\beta - \Omega)^2 + (\Gamma_\beta / 2)^2}. \quad (2.17)$$

Most molecules will have multiple normal modes  $\beta$  which are Raman active. Since the signal field is proportional to the phonon amplitude, and the phonon amplitudes are driven coherently by the mixing of optical fields, the total signal field growth is given by

$$E(\omega_s) = \sum_\beta E_\beta(\omega_s), \quad (2.18)$$

i.e. the fields are added, not like the spontaneous Raman scattering case where the intensities scattered from each normal mode are summed. If the signal is measured in

situations for which the net gain is small over a sample of length  $L$  and the depletion of the pump can be neglected, it is useful to expand the signal generated at a distance  $z$  into the sample as

$$E_{\beta}(\omega_s, z) \cong E(\omega_s, 0) \left[ 1 + \frac{g_{RG\beta}(\Omega)}{2} I(\omega_p) z \right] \quad (2.19)$$

where  $E_{\beta}$  is the total signal at the distance  $z$  into the sample. Thus

$$\frac{I(\omega_s, z) - I(\omega_s, 0)}{I(\omega_s, 0)} = \sum_{\beta} g_{RG\beta}(\Omega) I(\omega_p) z. \quad (2.20)$$

This formula describes the Raman gain from a single molecular species.

### 2.1.2 Spontaneous Raman Scattering

In spontaneous Raman scattering the phonon modes are excited by thermal noise so that there is no correlation between vibrations of the same frequency by different molecules and between different frequencies by the same molecule. This is a dilute gas, isolated molecule approximation which is quite valid in a disordered and dense medium as well. As a result the fields scattered are uncorrelated from molecule to molecule and between different vibrational modes in the same molecule. (There is of course weak coupling between vibrational modes, especially in a disordered medium, but there is no evidence that this significantly affects the Raman spectrum.) In this case, due to the statistical nature of the mode excitation, the energy for each vibration at temperatures for which in the high temperature limit defined by  $\hbar\omega \ll KT$  is  $KT$  where  $K$  is Boltzmann's constant. For the more general case, the average energy of the equivalent harmonic

oscillator (vibration) which includes both the potential and kinetic energy of the vibration, is given by

$$m_{\beta}\Omega_{\beta} \langle Q_{\beta}Q_{\beta}^{*} \rangle = \frac{\hbar}{1 - \exp\left[-\frac{\hbar\Omega_{\beta}}{KT}\right]} \quad (2.21)$$

for the case in which a phonon is created (Stokes scattering),  $\omega_p - \omega_s = \Omega \cong \Omega_{\beta}$  and

$$m_{\beta}\Omega_{\beta} \langle Q_{\beta}Q_{\beta}^{*} \rangle = \hbar \frac{\exp\left[-\frac{\hbar\Omega_{\beta}}{KT}\right]}{1 - \exp\left[-\frac{\hbar\Omega_{\beta}}{KT}\right]} \quad (2.22)$$

for the anti-Stokes case in which a phonon is annihilated and the frequency is shifted  $\omega_p - \omega_s = -\Omega \cong -\Omega_{\beta}$ . Here  $m_{\beta}$  is the effective mass for the vibration and the expressions contain the usual Boltzmann factor. When  $\hbar\omega \ll KT$ , both formulae reduce to

$$\langle Q_{\beta}Q_{\beta}^{*} \rangle = \frac{KT}{m_{\beta}\Omega_{\beta}^2}. \quad (2.23)$$

as required in the high temperature limit.

From this point on the derivations follow the classical routes described in Reference [33]. For Raman scattering from a single molecule, the frequency spectrum is given by

$$\frac{I_{\beta}(\omega_s)}{\Delta\Omega I(\omega_p)} = \frac{\omega_s^4}{8c^4(4\pi)^2\varepsilon_0^2} \sin^2\frac{\phi}{2} \left| \frac{\partial\alpha_{\beta}}{\partial q_{\beta}} \Big|_{q_{\beta}=0} \right|^2 \frac{\hbar}{m_{\beta}\Omega_{\beta}} [1 - \exp(-\frac{\hbar\Omega_{\beta}}{kT})]^{-1} \quad (2.24)$$

$$X \left\{ \frac{\Gamma_{\beta}/2\pi}{(\omega_p - \omega_s + \Omega_{\beta})^2 + (\Gamma_{\beta}/2)^2} + \exp(-\frac{\hbar\Omega_{\beta}}{kT}) \frac{\Gamma_{\beta}/2\pi}{(\omega_p - \omega_s - \Omega_{\beta})^2 + (\Gamma_{\beta}/2)^2} \right\}$$

Here  $\Delta\Omega$  is the solid angle subtended at the detector and  $\phi$  is the scattering angle. If there are multiple different Raman-active vibrations which contribute to the scattered light, and the number density of the different species is  $N_\beta$

$$I(\omega_s) = \sum_{\beta} N_{\beta} I_{\beta}(\omega_s) \quad (2.25)$$

then the intensity spectra due to scattering from different modes are simply added together.

### 2.1.3 Inhomogeneously Broadened Line Shapes

A complete description of Raman processes requires that the inhomogeneous broadening due to the disordered nature of glasses needs to be included. This means that each molecule, depending on its local environment, may have a different vibrational frequency  $\Omega_\beta$ . Consider a disordered medium which gives rise to a volume distribution of the species which in turn gives rise to a distribution of the vibrational frequencies  $\Omega_\beta$  of the form  $f(\Omega_\beta - \Omega_{\beta 0})$  in which the distribution peaks at  $\Omega_{\beta 0}$  with a total species number density  $N_{\beta 0}$ . The number density of molecules with vibrational frequencies  $\Omega_\beta$  in a frequency interval  $d\Omega_\beta$  is given by

$$N_{\beta 0} f(\Omega_\beta - \Omega_{\beta 0}) d\Omega_\beta \quad (2.26)$$

with

$$\int_0^{\infty} f(\Omega_\beta - \Omega_{\beta 0}) d\Omega_\beta = 1 \quad (2.27)$$

The spontaneous Raman spectrum is now given by

$$I(\omega_s) = \sum_{\beta} N_{\beta 0} \int_0^{\infty} f(\Omega_{\beta} - \Omega_{\beta 0}) I_{\beta}(\omega_s) d\Omega_{\beta}. \quad (2.28)$$

Furthermore the Raman gain spectrum is given by

$$g_{RG}(\Omega) = \sum_{\beta} N_{\beta 0} \int_0^{\infty} \frac{\omega_s}{4m_{\beta 0}n_s n_p c^2 \varepsilon_0^2} \left| \frac{\partial \alpha_{ii}^{\beta 0}}{\partial q_{\beta 0}} \right|_{q_{\beta 0}=0}^2 f(\Omega_{\beta} - \Omega_{\beta 0}) \frac{\Omega \Gamma_{\beta}}{(\Omega_{\beta}^2 - \Omega^2)^2 + \Omega^2 \Gamma_{\beta}^2} d\Omega_{\beta}. \quad (2.29)$$

It is generally believed that the breadth  $\Delta\Omega_{\beta}$  of  $f(\Omega_{\beta}-\Omega_{\beta 0})$  is governed by the distribution of the vibrational frequencies  $\Omega_{\beta}$  due to disorder in glasses. When spontaneous Raman spectra in crystals are compared to their counterparts in the glassy version of medium, it is generally found that the crystal lines are much narrower than those in the glasses. In the usually accepted limit that  $\Delta\Omega_{\beta} \gg \Gamma_{\beta}$ , the expressions for both Raman processes can be simplified by noting that

$$\frac{\Gamma_{\beta} / 2\pi}{(\omega_p - \omega_s + \Omega_{\beta})^2 + \Gamma_{\beta}^2} \cong \delta(\Omega - \Omega_{\beta}). \quad (2.30)$$

Then the integral in Equation 2.28 gives for  $\omega_p - \omega_s = \Omega$

$$\frac{I(\omega_s)}{\Delta\Omega I(\omega_p)} = \sum_{\beta} N_{\beta 0} \frac{\omega_s^4}{8c^4 (4\pi)^2 \varepsilon_0^2} \sin^2(\phi/2) \left| \frac{\partial \alpha_{ii}^{\beta 0}}{\partial q_{\beta 0}} \right|_{q_{\beta 0}=0}^2 \frac{\hbar}{m_{\beta 0} \Omega} X[1 - \exp(-\frac{\hbar\Omega\beta 0}{kT})]^{-1} f(\Omega - \Omega_{\beta 0}) \quad (2.31)$$

for the Raman spectrum. Conversely, if  $\Delta\Omega_{\beta} \ll \Gamma_{\beta}$ , Equation 2.24 is recovered. Furthermore, if neither of these limits is valid the spectrum can be complicated, with the largest deviation from the two limits occurring when  $\Delta\Omega_{\beta} \approx \Gamma_{\beta}$ . In that case, Equation 2.28 must be evaluated numerically.



The situation is somewhat more complex in the case of the Raman gain unless the approximations in Equation 2.16 are applied. In that limit the integral in Equation 2.29 can be performed which gives

$$g_{RG}(\Omega) = \sum_{\beta} \frac{N_{\beta 0} \omega_s \pi}{2m_{\beta 0} n_s n_p c^2 \epsilon_0^2} \left| \frac{\partial \alpha_{ii}^{\beta 0}}{\partial q_{\beta 0}} \right|_{q_{\beta 0}=0}^2 \frac{1}{2\Omega} f(\Omega - \Omega_{\beta 0}) \quad (2.32)$$

Conversely, if  $\Delta\Omega_{\beta} \ll \Gamma_{\beta}$ , Equations 2.15 in the general case and 2.17 if the natural line width is much smaller than the frequency shift  $\Omega_b$  are recovered. Furthermore, if neither of these limits is valid the spectrum can be complicated, with the largest deviation from the two limits occurring when  $\Delta\Omega_{\beta} \approx \Gamma_{\beta}$ . In that case, Equation 2.29 must be evaluated numerically.

Frequently the inhomogeneously broadened distribution  $f(\Omega_{\beta} - \Omega_{\beta 0})$  has been assumed to take a gaussian-like shape of the form

$$f(\Omega_{\beta} - \Omega_{\beta 0}) = A \exp \left[ \frac{-(\Omega_{\beta} - \Omega_{\beta 0})^2}{\Delta\Omega_{\beta}^2} \right]. \quad (2.33)$$

This is a reasonable approximation to a Voigt distribution that might be a more appropriate inhomogeneous lineshape function when deconvolving the actual spectra of amorphous materials. The gaussian distribution, however, is more easily used in numerical calculations.

#### 2.1.4 Summary: Single Raman Active Species

It is clear that the wavelength (or frequency,  $\Omega$ ) dependence of the two response functions is essentially identical except in the tails of the spectrum. At  $\Omega = 0$  the Raman gain coefficient is zero where-as the Raman spectrum does not necessarily go to zero

there. This implies that a spontaneous Raman scattering experiment will yield the Raman gain spectral distribution if the same pump frequency is used. Note that obtaining an absolute value of the Raman gain coefficient via spontaneous Raman scattering requires exact knowledge of the scattering geometry, the scattering optics, the detector sensitivity etc.

Another fundamental difference between the two processes, which becomes important when corrections from measurement wavelengths to operating gain wavelengths are needed, is the wavelength dispersion dependences of the two Raman

interactions. Both processes are proportional to  $\left| \frac{\partial \alpha_{ii}^{\beta}}{\partial q_{\beta}} \right|_{q_{\beta} = 0}^2$ , which to first order

approximation contains the dispersion associated with  $(n^2 - 1)^2$ . Hence, the dispersion dependence of the spontaneous Raman scattering process is equivalent to  $(n^2 - 1)^2$ , and

for Raman gain it is  $\frac{(n^2 - 1)^2}{n^2}$ . These corrections become particularly important when

measurements are made close to the absorption band edge of the material under examination, which is usually the case for spontaneous Raman measurements that are conducted in the visible range on glasses with heavy species such as  $\text{TeO}_2$ ,  $\text{PbO}$ ,  $\text{TlO}_{0.5}$ ,  $\text{Nb}_2\text{O}_5$ , etc.

For the classic Raman gain material, fused silica, the Raman gain spectrum is well-known from very careful spontaneous Raman scattering experiments [23,37]. Hence silica is used as a reference material in obtaining the absolute Raman gain spectrum of new materials by taking the two spectra, silica and the glass of interest, under exactly the same conditions. Silica has a very strong vibrational peak at  $440 \text{ cm}^{-1}$  (13.2 THz) and

much smaller peaks at 800 (24), 1065 (32) and 1200  $\text{cm}^{-1}$  (36 THz), corresponding to the Si-O-Si bond rocking and bending, asymmetric stretching, and the TO and LO splitting pairs respectively. The two other sharp bands characteristic of the Raman spectrum of vitreous  $\text{SiO}_2$ , occurring at 495 (15) and 606  $\text{cm}^{-1}$  (18 THz), are identified as defects found in the silica structure, known as the  $D_1$  and  $D_2$  peaks respectively. Because there is effectively one dominant peak, the spontaneous Raman and gain spectra are essentially identical near their maximum value, and in fact Stolen and Ippen found excellent agreement between a carefully measured Raman spectrum of bulk fused silica and a calibration point from a direct Raman gain measurement for a frequency shift of 330  $\text{cm}^{-1}$  (9.9 THz) in a fused silica fiber [23].

## ***2.2 Raman Physics in Multi-component Glasses***

Many of the modern glasses currently under consideration as new Raman gain materials contain two or more species which are incorporated into the glass matrix. This case requires special attention because such glasses became the focus of a controversy in the literature about differences between Raman gain coefficients measured by direct nonlinear optics techniques and spontaneous Raman scattering.

Consider a multi-component glass with each component when analyzed separately has its own distinct vibrational modes and electronic states (labeled by “ $r$ ”). An example of a two component glass would be  $\text{TeO}_2\text{--WO}_3$ . The two oxide constituents - tellurium oxide and tungsten oxide - each have well-defined vibrational modes and electronic transitions. In the glassy state the two components to a first approximation retain the same vibrational frequencies and peak wavelengths for their absorption lines.

The polarizability of species “ $k$ ” in its own frame of reference, when modulated by its  $\beta$ 'th Raman active phonon of amplitude  $Q_\beta^k$  can be written as

$$\alpha_{ij}^k = \sum_r \alpha_{ij}^{k,r}(\omega_1 - \omega_{k,r}) + \sum_r \sum_\beta \left\{ \frac{\partial \alpha_{ij}^{k,r}(\omega_1 - \omega_{k,r})}{\partial Q_\beta^k} \Big|_{Q_\beta^k=0} \right\} Q_\beta^k \quad (2.34)$$

where  $\partial \alpha_{ij}^{k,r}(\omega_1 - \omega_{k,r}) / \partial Q_\beta^k$  is the Raman molecular susceptibility. To facilitate comparison of Raman interactions at different pump laser frequencies, the notation has been changed for the pump laser frequency to  $\omega_1, \omega_2, \dots$  etc. Note that each contribution to the linear polarizability (first summation in Equation 2.34), and to the Raman susceptibility (second summation) is associated with a specific electronic transition in the species centered at the frequency  $\omega_{k,r}$  with some complex spectral distribution and transition matrix element. The transition frequencies coincide with peaks in the absorption spectrum. Thus the Raman susceptibilities undergo dispersion with frequency and how strong the dispersion is depends on the frequency shift between the transition frequency and pump laser frequency. For example, from Equation 2.34, the refractive index of the material is given by

$$n^2 = 1 + \frac{1}{\epsilon_0} \sum_k N_k \text{Real} \left\{ \sum_r \alpha_{ij}^{k,r}(\omega_1 - \omega_{k,r}) \right\}, \quad (2.35)$$

where  $N_k$  is the number density of species  $k$  in the glass. (The absorption spectrum is given by the imaginary component). Hence the frequency (wavelength) dispersion in the refractive index is a summation of the dispersion due to all of the electronic transitions in all the component species.

Since the discrepancies discussed above had their origin in the spontaneous Raman scattering experiments, it is useful to obtain detailed expressions for this process

including all of the factors involved. The scattering occurs inside the material but the laser source and the detection system are in air. Thus it is necessary to take into account at the air-glass boundary the Fresnel transmission coefficient and the effect of refraction on the solid angle subtended at the detector for a typical Raman scattering experiment [19,21]. The peak intensity of a Raman scattered line  $I_{\beta}^{k,r}(\omega_1 - \Omega_{\beta}^k)$  in air (at the detector) due to the  $\beta$ 'th normal mode of the  $k$ 'th species to the incident intensity  $I_{inc}(\omega_l)$  in air, at frequency  $\omega_l$  is given by

$$\frac{I_{\beta}^{k,r}(\omega_1 - \Omega_{\beta}^k)}{I_{inc}(\omega_1)\Delta\Omega} = K_{SR}^{k,r}(\omega_1 - \Omega_{\beta}^k)^4 \frac{[1 - R(\omega_1)][1 - R(\omega_1 - \Omega_{\beta}^k)]}{[n(\omega_1 - \Omega_{\beta}^k)]^2} \left| \frac{\partial \alpha_{ij}^{k,r}(\omega_1 - \omega_{k,r})}{\partial Q_{\beta}^k} \right|^2 \quad (2.36)$$

where  $\Delta\Omega$  is the solid angle at the detector,  $\Omega_{\beta}^k$  is the frequency shift of the Raman peak from the laser frequency  $\omega_1$ ,  $R$  is the reflectance coefficient  $\left( R(\omega) = \frac{[n(\omega) - 1]^2}{[n(\omega) + 1]^2} \right)$  at normal incidence, and the  $[n(\omega_1 - \Omega_{\beta}^k)]^2$  in the denominator is a consequence of the solid angle correction. All of the explicit dependence on frequency has been shown in Equation 2.36 and all of the phonon and electromagnetic parameters, including the Bose-Einstein thermal population factor, are contained in the constant  $K_{SR}^{k,r}$ . Similarly, the dependence of the Raman gain coefficient (defined for the pump irradiance) on frequency is given by

$$g_{RG_{\beta}}^{k,r}(\omega_1 - \Omega_{\beta}^k) = K_{RG}^{k,r} \frac{(\omega_1 - \Omega_{\beta}^r)}{n(\omega_1 - \Omega_{\beta}^r)n(\omega_1)} \left| \frac{\partial \alpha_{ij}^{k,r}(\omega_1 - \omega_{k,r})}{\partial Q_{\beta}^k} \right|^2, \quad (2.37)$$

where  $K_{RG}^{k,r}$  is a constant that contains all the phonon and electromagnetic constant parameters and is *different* from  $K_{SR}^{k,r}$  [22]. When all of the experimental details are taken into account, it is therefore possible to evaluate the Raman gain coefficient in multi-component glasses from the spontaneous Raman spectrum, at the *same excitation frequency*. The detailed relationship is

$$g_{RG\beta}^{k,r}(\omega_1 - \Omega_\beta^r) = \frac{K_{RG}^{k,r}}{K_{SR}^{k,r}} \frac{n(\omega_1 - \Omega_\beta^r)}{(\omega_1 - \Omega_\beta^r)^3 n(\omega_1) [1 - R(\omega_1)] [1 - R(\omega_1 - \Omega_\beta^r)]} \frac{I_\beta^{k,r}(\omega_1 - \Omega_\beta^r)}{I_{inc}(\omega_1) \Delta\Omega}. \quad (2.38)$$

However, clearly the frequency dispersion in the refractive index and Raman susceptibility needs to be corrected for when comparing Raman scattering spectra at one frequency with Raman gain measurements at a different frequency.

Frequency dispersion in nonlinear optical coefficients, including the Raman susceptibility, is well-known in nonlinear optics [38-40]. Although the Raman susceptibility must also exhibit dispersion with frequency, it is not *á priori* the same as the refractive index dispersion because not all of the vibrational modes couple (modulate) equally to the molecular polarizability. Therefore the dispersion in refractive index cannot in principle be used to evaluate the dispersion in the Raman susceptibility. However, in the special cases when there is one dominant peak in the Raman spectrum due to coupling to a dominant electronic transition that is also primarily responsible for the dispersion in the refractive index in the wavelength range of interest, then the wavelength dispersion of the Raman susceptibility can be obtained from the index dispersion [9]. Thus the resonant enhancement in the susceptibility

$\partial\alpha_{ij}^{k,r}(\omega_1 - \omega_{k,r}) / \partial Q_{\beta}^k$  for frequencies below the electronic absorption band edge may be linearly proportional to the resonant enhancement in  $\alpha_{ij}^{k,r}(\omega_1 - \omega_{k,r})$ . This enhancement is approximated by  $(n^2(\omega_1) - 1)$ .

This correction has been proven to work in the case of fused silica. In fact, in many materials only a limited number of electronic transitions are important, as is well-known from typical absorption spectra. In general, the closer the laser excitation frequency is to  $\omega_{k,r}$ , the larger the resonant enhancement in the Raman susceptibility and the more intense the particular Raman peaks will be. Furthermore, in such conditions if two different vibrations couple to susceptibilities whose associated absorption maxima have different resonance frequencies ( $\omega_{k,r}$ ), as shown in Figure 2.3, then their relative contributions to a Raman spectrum will change with frequency  $\omega_l$ . These are the two features which will be examined experimentally later in order to test the importance of frequency dispersion of the Raman cross-section on measurements of Raman spectra at different frequencies  $\omega_l$ . A misunderstanding of these issues has led to criticism of the work described in this thesis and the resolution of the discrepancies claimed will be discussed in Chapter 5.

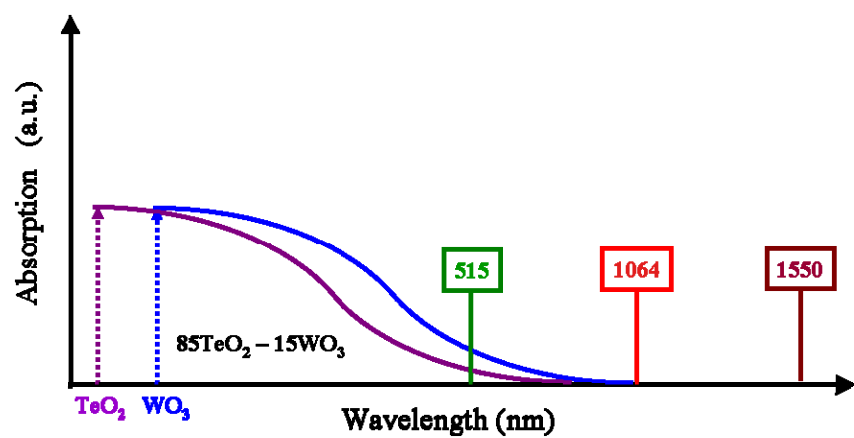


**Figure 2.3.** Example of the absorption spectrum of the compound  $85\text{TeO}_2 - 15\text{WO}_3$  which shows the tails of the absorption edge due to different component species extending different distances into the visible part of the spectrum. The locations of three important pump wavelengths are also indicated



## CHAPTER THREE: EXPERIMENTAL APPARATUS, MEASUREMENT TECHNIQUES AND DATA ANALYSIS

### ***3.1 Raman Gain: Finite Cross-section Beams and Pulsed Fields***

In Chapter 2 the usual theoretical analysis of the Raman gain process was presented in the plane wave limit, the slowly varying phase and amplitude approximation, and negligible loss and pump depletion limit. The growth of the Raman signal was given by the equation

$$\frac{d}{dz} E_R(z) = \frac{g_{RG}}{2} E_S(z) I_P(z) \quad (3.1)$$

where  $E_S(z)$  is the injected signal field,  $E_R(z)$  is the generated Raman signal field,  $g_{RG}$  is the material Raman gain coefficient (for the Raman irradiance) at a specific frequency shift from the pump, and  $I_P(z)$  is the pump beam irradiance. In practice, however, the beams used experimentally are obtained from pulsed lasers and therefore have finite transverse dimensions and finite temporal envelopes. Hence in order to obtain absolute Raman gain coefficients experimentally, it is necessary to modify the theory to include these additional factors.

The goal is to facilitate rapid characterization of test quantities of bulk samples. Test quantities of optically homogeneous samples of complex glasses useful for rapid characterization can be routinely fabricated in thicknesses of a few millimeters. Furthermore, when one substitutes the Raman gain for fused silica, the standard against which all other materials are compared, it becomes clear that focused pulsed laser beams

are needed in order to provide enough electric field strength to induce the nonlinear process under investigation in such small samples.

Consider beams which are finite in space and time, *viz.* focused beams out of a pulsed laser. Assuming negligible pump and injected signal field depletion,

$$\begin{aligned} E_R(x, y, z, t) &= E_R^p(z) f_R(x, y, t) \\ E_S(x, y, 0, t) &= E_S^p(z) f_S(x, y, t) \\ E_P(x, y, z, t) &= E_P^p(z) f_P(x, y, t) \end{aligned} \quad (3.2)$$

where the  $f_i(x, y, t)$  are the space-time profiles of the  $i=R, S, P$  fields normalized so that  $f_i(0, 0, 0)=1$  with  $E_R^p(z), E_S^p(z), E_P^p(z)$  as the peak fields. Assuming Gaussian shaped fields (verified experimentally in this case),

$$\begin{aligned} f_S(x, y, t) &= \exp\left[-\frac{(x^2 + y^2)}{\omega_S^2} - \frac{t^2}{\tau_S^2}\right] \\ f_P(x, y, t) &= \exp\left[-\frac{(x^2 + y^2)}{\omega_P^2} - \frac{t^2}{\tau_P^2}\right], \end{aligned} \quad (3.3)$$

so that

$$f_R(x, y, t) = f_S(x, y, t) f_P^2(x, y, t). \quad (3.4)$$

Here  $\omega_p$  ( $\omega_s$ ) and  $\tau_p$  ( $\tau_s$ ) are the pump (signal) beam waists and pulse widths at the 1/e value of the normalized electric field. Note that although both the Raman and signal fields propagate together at the same frequency, the Raman field has a different spatial distribution than the input signal field. Integrating Equation 3.1 over a sample length  $L$  with the zero depletion assumption for both the pump and incident signal fields, Equation 3.1 gives

$$E_R^p(L) = \frac{1}{2} g_{RG} L E_S^p(0) I_P^p(0) . \quad (3.5)$$

Thus total output field at the Raman (and signal) frequency is

$$E_T(x, y, L) = E_S^p(0)f_S(x, y, t) + \frac{1}{2}g_{RG}LE_S^p(0)I_P^p(0)f_S(x, y, t)f_P^2(x, y, t). \quad (3.6)$$

Writing  $I_T(x, y, L, t) = 0.5c\epsilon_0n_s^2E_T^2(x, y, t)$ ,

$$I_T(x, y, L, t) = I_S^p(0)f_S^2(x, y, t)\left[1 + \frac{1}{2}g_{RG}LI_P^p(0)f_P^2(x, y, t)\right]^2. \quad (3.7)$$

Again making the assumption of small Raman signal the bracket  $[1+A]^2$  can be expanded for small  $A$  and truncated at the leading term to give  $I + 2A$  so that

$$I_T(x, y, L, t) = I_S^p(0)f_S^2(x, y, t)\left[1 + g_{RG}LI_P^p(0)f_P^2(x, y, t)\right]. \quad (3.8)$$

In the actual experiment it is the pulse energy  $\Delta E_i$  which is measured. It is obtained from Equation 3.8 by integrating the fluence over  $x$ ,  $y$  and  $t$  which gives

$$\Delta E_T(L) = \Delta E_S(0) \left[ 1 + \frac{\sqrt{8}}{\pi^{3/2}} \frac{1}{(\omega_s^2 + \omega_p^2)\sqrt{\tau_s^2 + \tau_p^2}} g_{RG}L\Delta E_P(0) \right]. \quad (3.9)$$

for the total output pulse energy (input signal + Raman) at the signal frequency. The Raman gain coefficient  $g_{RG}$  was evaluated from the data based on the equation,

$$g_{RG}L = \frac{\Delta E_T(L) - \Delta E_S(0)}{\Delta E_S(0)\Delta E_P(0)} (w_p^2 + w_s^2) \sqrt{(\tau_s^2 + \tau_p^2)} \left(\frac{\pi}{2}\right)^{\frac{3}{2}}. \quad (3.10)$$

Fused silica gain coefficients peak at  $\sim 10^{-13}$  m/W near 1  $\mu$ m pumping and one expects values on the order of  $10^{-12}$  m/W for highly nonlinear glasses [5,6]. A simple calculation shows that pump irradiances of 1-10 GW/cm<sup>2</sup> are required in order to detect approximately 10% gain which sets the peak irradiance needed from the laser used. It was verified, with the exception of some chalcogenide glasses, that such irradiances are below the damage threshold of the glasses studied to date.

The vibrational Raman response has been confirmed to be on the order of hundreds of femtoseconds [41]. For the slowly varying envelope approximation to remain valid, the experimental apparatus should have time domain pulse widths in the picosecond regime. This will require precision delay lines so that the signal and pump beams are optimally overlapped in time.

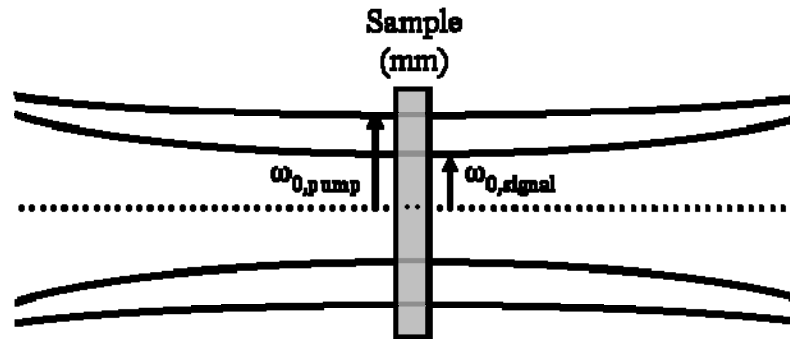


**Figure 3.1.** Pump and probe beam interactions in Raman gain measurements. The Rayleigh range of the probe beam is 1.4 cm at the longest wavelengths tested, which enables a plane wave approximation in millimeter thick bulk samples

Figure 3.1 shows the actual beam interaction geometry for measuring the Raman gain in a bulk sample. In order to approximately optimize the amplification of the output beam due to Raman gain, the spatial beam overlap, in addition to the temporal overlap needed to be optimized. Given the previous constraint on sample thickness, simulations were performed in order to determine what pump and input signal beam sizes were required within the glass sample to meet beam overlap requirements to ensure maximum Raman gain. Given the maximum energy per pulse available (400  $\mu\text{J}$ ), beam waists of around 100  $\mu\text{m}$  were required for the pump wavelength. In order to ensure spatial overlap of the pump and signal inside the sample, the input signal beam waist was chosen to be roughly half that of the pump beam waist. This was based on the Rayleigh range of the input signal beam. The sample was positioned so that the beam foci of the pump and

signal were both in the middle of the sample. As will be discussed below, operating in the linear (versus exponential) growth regime allows simple corrections to be made for the finite beam sizes and pulsed nature of the experiment.

### 3.2 Description of the Experimental Apparatus

Figure 3.2 depicts the experimental apparatus used for making Raman gain measurements in millimeter thick bulk glass samples.

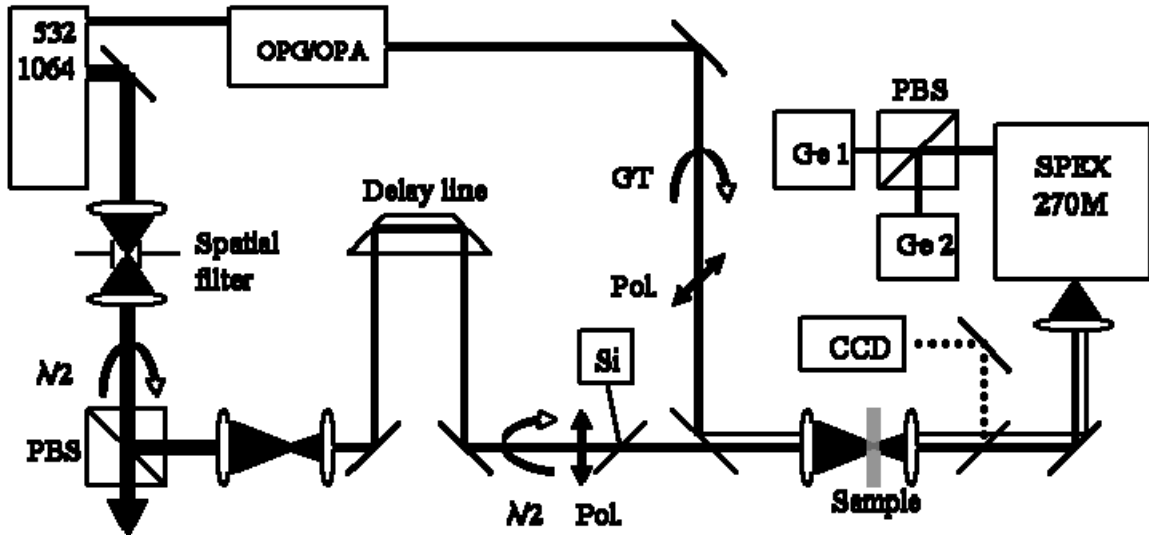
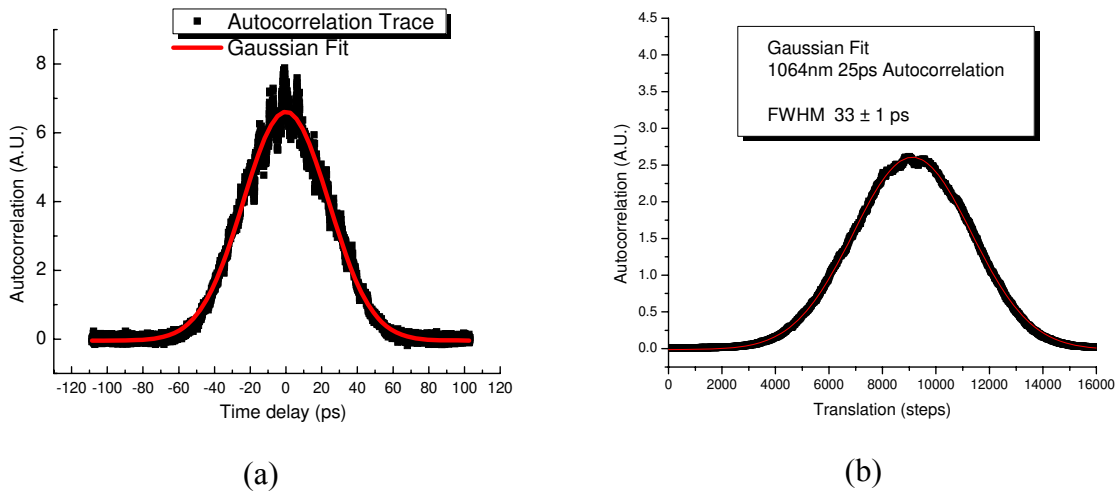


Figure 3.2. Major equipment used in experimental apparatus for Raman gain measurements. A detailed explanation is given in the text

Given the points of consideration mentioned above, a Q-switched, mode-locked Nd:YAG laser with pulse widths of approximately  $(33 \pm 2)$  ps ( $1/e$  of electric field) is chosen [42]. Pulse widths are verified by autocorrelation measurements using a 0.5 mm thick c-cut LiNbO<sub>3</sub> crystal and a 2 mm thick KTP crystal at separate times. Typical results for autocorrelations using the LiNbO<sub>3</sub> crystal are shown in Figure 3.3 (a), and

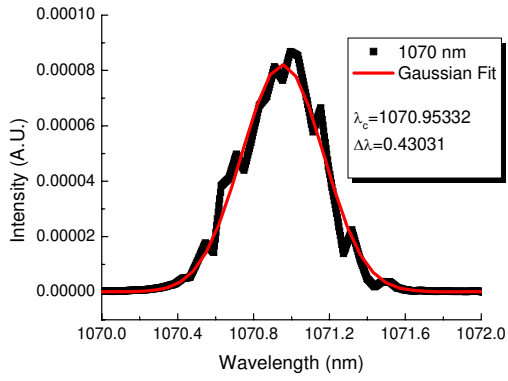
typical results for autocorrelations using the KTP crystal are shown in Figure 3.3 (b). The LiNbO<sub>3</sub> crystal uses Type I phase-matching so that the autocorrelation sits on a background pedestal and shows fringes. The KTP crystal uses Type II phase-matching so the autocorrelation is free of background noise and does not suffer from fringe effects.



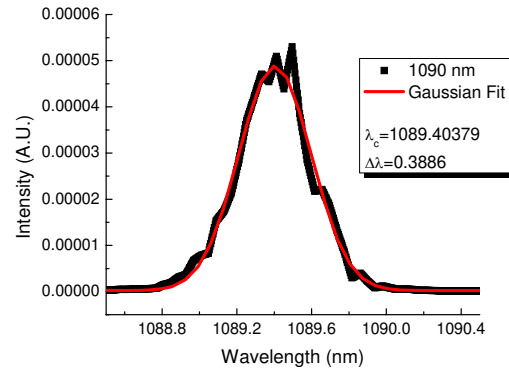
**Figures 3.3 (a) & (b).** Autocorrelation traces of the 1064 nm pump beam with (a) LiNbO<sub>3</sub> crystal and (b) KTP crystal

The laser source is an EKSPLA 2143A whose 1064 nm emission line was used as the Raman gain ( $\Delta E_p$ ) pump source. The repetition rate of 10 Hz is advantageous for allowing thermal effects to dissipate between measurements. The laser operates using two laser crystal rods operating in an oscillator and amplifier arrangement. In the oscillator branch, a single flash lamp is fired and free running pulses are mode-locked using a passive organic dye suspended in an ethyl alcohol solution. After several passes in the oscillator cavity to deplete most of the energy in the laser crystal, a Q-switch dumps the appropriate pulse (selected by the user) into the amplifier cavity. The

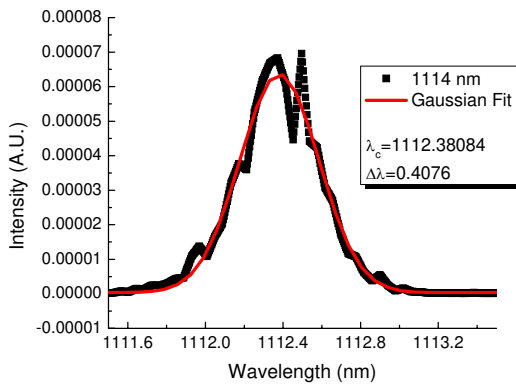
amplifier laser crystal is larger in diameter and longer in length than the oscillator laser crystal rod in order to preserve optimum spatial quality and a high energy per pulse. The amplifier laser rod is placed in a dual flash lamp chamber and the amount of amplification (selected by the user) is changed by altering the timing of the firing of the flash lamps with respect to the Q-switch. The amplifier branch uses a dual-pass configuration. A  $\lambda/4$  plate and polarizing beam splitter is used to dump the laser pulse out of the amplifier cavity after propagating through the laser crystal. A K\*DP second harmonic generation (SHG) crystal converts 35% of the 1064 nm emission into 532 nm. Up to 8 mJ at 532 nm is used to pump an optical parametric generator and amplifier (OPG/OPA), an EKSPLA PG501VIR tunable from 680 – 2300 nm [43]. It utilizes a motorized grating and two BBO crystals which are kept at a steady temperature via heaters. The BBO crystals and grating are angle tuned in order to provide the proper wavelength at the output. Output pulse energies of hundreds of microjoules have an energy stability of  $\pm 10\%$  (300 laser shot RMS deviation). Figures 3.4 (a) – (h) are the spectra obtained from the OPG/OPA using an ANDO AQ-6915E optical spectrum analyzer over a typical wavelength range used in the Raman gain measurements. The spectral measurements were made using a resolution of 0.05 nm and averaging of 10 laser shots per resolution point in order to remove the shot-to-shot noise of the OPG/OPA. The spectral bandwidth never exceeds 0.5 nm, which is equivalent to a bandwidth of  $4 \text{ cm}^{-1}$ .



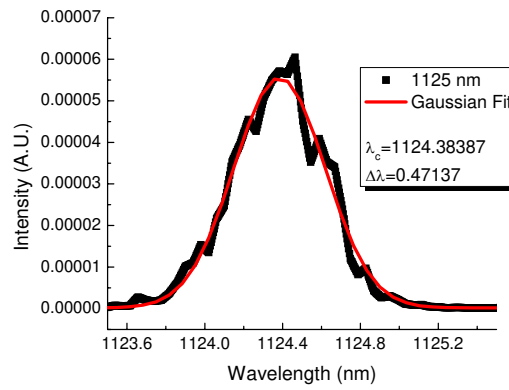
(a)



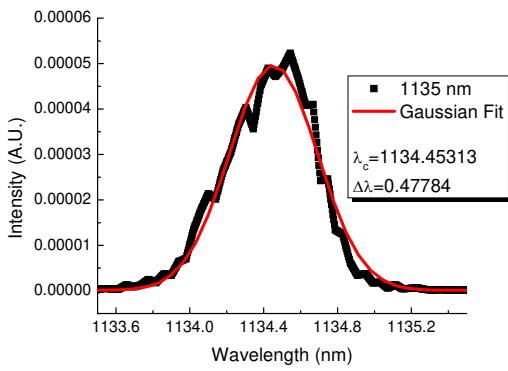
(b)



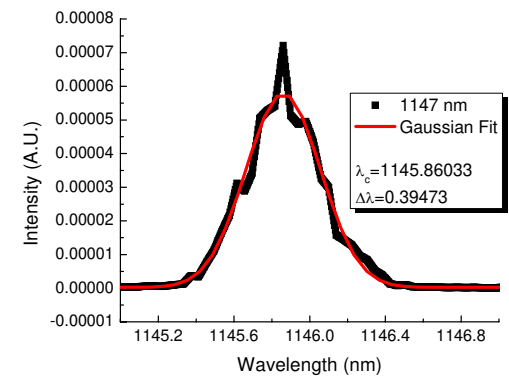
(c)



(d)

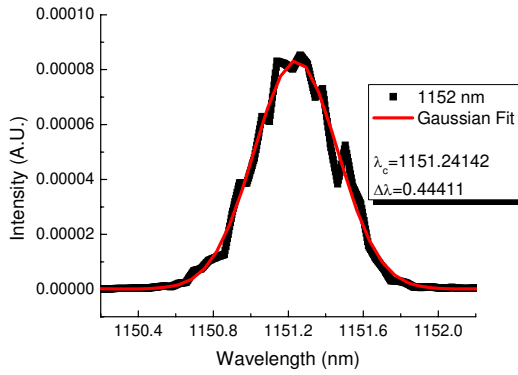


(e)

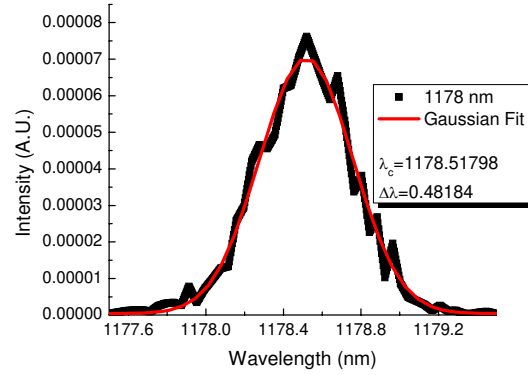


(f)





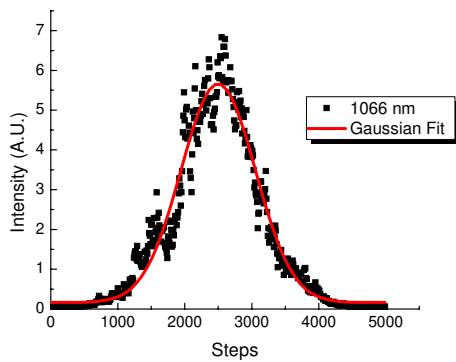
(g)



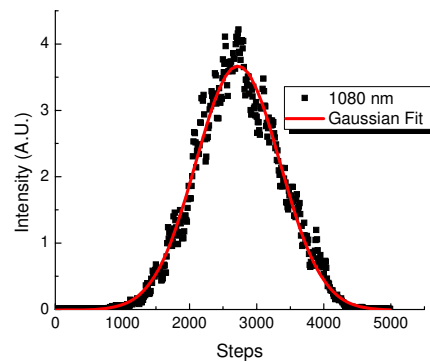
(h)

**Figures 3.4 (a) – (h).** Spectra obtained from the OPG/OPA

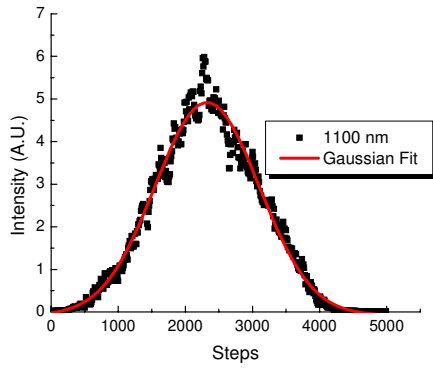
Autocorrelation measurements were made and OPG/OPA pulse widths varied between 7 – 10 ps ( $1/e$  of electric field) in the wavelength range used (1070 – 1250 nm) and are depicted in Figures 3.5 (a) – (f). The autocorrelation pulse width variation with wavelength is shown in Figure 3.6. At each discrete wavelength tested, the pulse width stability was  $\pm 1$  ps over the duration of the autocorrelation measurements when fitting the data to a Gaussian shape. The triangular shape of the autocorrelation signal signifies that a slight chirp exists across the pulses from the OPG/OPA.



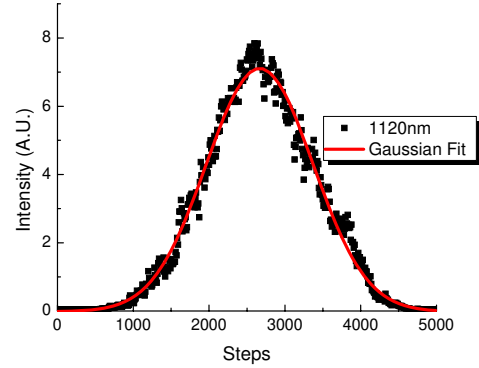
(a)



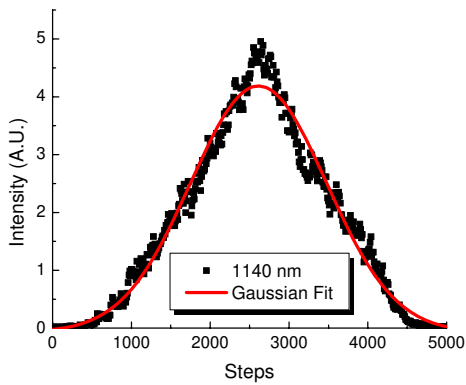
(b)



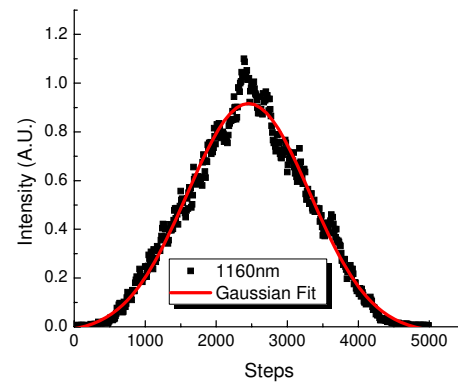
(c)



(d)



(e)



(f)

Figures 3.5 (a) – (f). Autocorrelations of OPG/OPA pulses with a slight frequency chirp

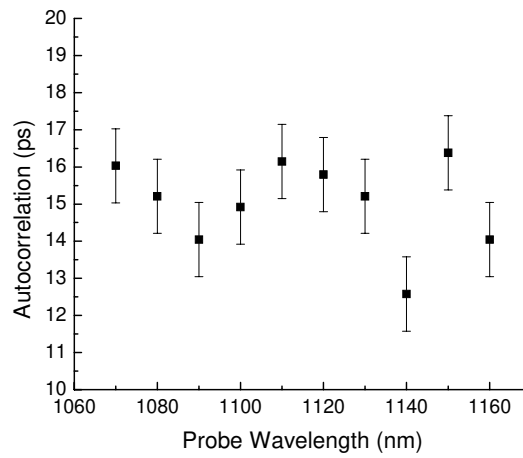


Figure 3.6. Pulse width variation as a function of wavelength from OPG/OPA

The 1064 nm beam remaining after the K\*DP doubling crystal was spatially filtered using a telescope and a pinhole at the focus. Spatial filtering is required since the SHG process to create 532 nm for pumping the OPG/OPA leaves the 1064 nm beam severely non-Gaussian in the spatial profile. The beam is then re-collimated after the pinhole and reduced in diameter by a factor of two by a telescope. A delay line is employed in order to optimize temporal overlap with the input signal beam from the OPG/OPA. A half-wave plate and polarizer (Pol.) is used to control the intensity and set the linear polarization at the sample. An optical beam sampler from Newport is used to redirect less than 5% of the pump beam energy towards a reversed biased silicon detector (Si) which is calibrated against a precision pyrometer where the sample is located. The role of this detector is to measure the pump energy into the sample on a single shot basis.

The input signal beam from the OPG/OPA is propagated through a Glan-Thompson broadband polarization rotator (GT) and polarizer in order to control the input signal intensity and set the polarization. The polarization of the input signal beam is set such that it is linearly polarized at  $45^\circ$  with respect to the pump beam. In the Raman gain measurements, the output beam which is polarized parallel to the pump was the  $\Delta E_T(L)$  in Equations 3.9 and 3.10, where-as the orthogonal polarization is used to establish approximately the  $\Delta E_S(0)$ , based on the fact that the amplification of the orthogonal polarization (to the pump) is given approximately by the spontaneous Raman depolarization ratio as a function of wavelength. The pump and signal beams are then combined at another optical beam sampler which is oriented in order to allow maximum transmission of the pump beam. The optical beam sampler is anti-reflection coated for 1064 nm and is also slightly wedged in order to avoid ghosting of the signal beam at the

sample since the input signal beam is redirected based on Fresnel reflection [44]. A lens with a focal length of 28 cm is chosen in order to provide the necessary input signal beam size. Extensive knife-edge measurements are made in order to characterize the dispersion of the beam waist size and focus location of the input signal beam when its wavelength is varied. Since the input signal beam is larger at the focusing lens than the pump beam, the signal beam gets focused to a smaller beam waist inside the sample. The beam waist sizes inside the sample are approximately 125 microns for the pump beam and 75 microns for the input signal beam. The Rayleigh ranges are 1.65 cm for the input signal beam at 1070 nm and 1.4 cm at 1250 nm, and the pump beam has a Rayleigh range of 4.6 cm at 1064 nm. These large Rayleigh ranges as compared to the sample length allows the beams inside the sample to be approximated as a plane wave during propagation.

The energy at the sample can be as high as 400  $\mu\text{J}$  in the pump beam, where-as the input signal beam contains only a few  $\mu\text{J}$  of energy (enough for accurate detection). Temporal overlap of the two beams is accomplished by tuning the OPG/OPA to 1066 nm and using a collinear cross-correlation technique with the c-cut  $\text{LiNbO}_3$  crystal in a Type I phase-matching arrangement and detecting the new frequency that is generated. This can be done either with an optical spectrum analyzer or by using an aperture in front of the detector to spatially filter the 1064 nm and 1066 nm beams.

After the beams propagated and exchanged energy through the Raman gain process, they are collected with an imaging lens with a focal length of 7 cm. Neutral density filters are used to reduce the pulse energies to avoid burning the broadband metallic coated optics and grating inside of the monochromator. A metallic mirror on a

flip-mount, located after neutral density filters, is periodically used to redirect the beams to a CCD camera prior to the monochromator.

This camera serves two purposes. First, it is used as a double check that the beams are optimally spatially overlapped at each signal wavelength tested. Second, by laterally moving the sample, the input pump and signal beams are verified to produce minimum scattering from either surface imperfections or inhomogeneities inside the sample. The sample sits on two additional translation stages in order to provide precise control of the location of beam propagation through the sample. Once this is ensured, the beams are allowed to bypass the flip-mount mirror and are then directed towards the monochromator entrance slit. A cylindrical focusing lens with a focal length of 8 cm is used to direct the beams into a SPEX 270M monochromator which utilizes a 600 lines/mm single pass grating [45]. This lens reduces the fluence on the grating due to the strong pump beam, and additionally provides increased spectral resolution at the output slit of the monochromator. The monochromator slits are set at a 1 mm entrance width and 200 micron output width.

The experimental data is gathered as follows. A polarizing beam splitter and two germanium detectors (Ge 1 and Ge 2) are located at the output slit of the monochromator. The detectors are reverse biased germanium diodes from Judson Technologies with identical low pass filters built from common electrical components (approximately 10% tolerances) [46]. On a shot-to-shot basis, the voltages from the pump detector and germanium detectors are fed into a Stanford Research Systems boxcar data acquisition unit which is connected to a PC and controlled by LabView software. The delay and gate

width of the boxcar electronics are adjusted in order to provide the smallest possible error bars in the measurements.

Note that by taking the intensity (energy) ratios indicated in Equation 3.10 on a shot-by-shot basis, fluctuations in the OPG/OPA output pulse energy are removed to first order.

### ***3.3 Raman Gain Measurements and Data Analysis***

Multiple data sets consisting of 500 laser shots, one set for each discrete signal wavelength probed, are recorded on the computer. The pump beam irradiance can be varied for each grouping of 500 shots to check for linearity in the Raman gain with pump irradiance by adjusting the second half-wave plate in the pump branch. After this process is completed for a discrete wavelength, the pump beam is blocked from the sample surface and a 500 shot calibration of the signal is performed by rotating the Glan-Thompson broadband polarization rotator through the maximum and minimum transmission points. By obtaining a linear relationship of one signal detector  $\Delta E_T(L)$  to the other signal detector  $\Delta E_S(0)$ , the wavelength dependence of the apparatus is calculated out as well as any bias from the boxcar electronics. This is a critical step which must be performed for each amplified signal probe wavelength since the equipment after the sample – especially the monochromator grating and the germanium diodes - may not have the same response function for both polarizations. For probe wavelengths (1066 - 1080 nm) close to the pump wavelength, an additional calibration is performed by blocking the input signal at the sample surface and obtaining 500 laser shots by varying the pump energy at the sample via the second half wave plate. Another

linear relationship was found by obtaining the slope of the  $\Delta E_T(L)$  vs.  $\Delta E_P(0)$  curve to account for pump leakage through the output slit onto the germanium detector whose signal polarization was parallel to the pump beam polarization. The slope of this curve is used as an additional correction factor. A calibration for  $\Delta E_S(0)$  vs.  $\Delta E_P(0)$  is unnecessary because the polarizing beam splitter used at the output of the monochromator has an extinction ratio approaching 1000:1. In order to ensure the measurements are repeatable, the sample is moved on translation stages – orthogonal to the beam propagation direction – to verify the homogeneous nature of the glass where the measurements are made.

The data is then analyzed in order to calculate a Raman gain coefficient for each laser shot using conventional spreadsheet programs. Calculation of the Raman gain coefficient entails measuring the length of the sample with a precision micrometer. Signal averaging is performed over 500 shots in order to converge to a mean value and RMS deviation which represents the absolute Raman gain coefficient and error bars reported in the literature. Final corrections are made to the data based on the index of refraction values (to account for surface reflection losses) and the depolarization ratio obtained from the spontaneous Raman scattering experiments performed on the same glasses. The experimental Raman gain seen in the orthogonally polarized probe beam is frequently smaller than the error bars of the measurements. Since this is an experiment based on Raman gain of well-defined beams, there was no need to account for all of the index of refraction corrections needed in scattering measurements, for example to correct for solid angles subtended by the detector in Raman scattering and techniques utilizing the cross-section method.

### ***3.4 Application to Fused Silica and Multi-component Glasses***

The experimental apparatus needs to be checked for accuracy as well as precision. A 3.18 mm thick fused silica sample obtained from ESCO is used as a reference standard. The glass material is Corning 7980-2F. Due to the low Raman gain coefficient in pure fused silica, attempts to measure the entire Raman gain spectrum in the fused silica sample results in the appropriate shape of the Raman gain spectrum but larger error bars are obtained away from the peak where the Raman gain falls below the value  $0.5 \times 10^{-13}$  m/W. Figure 3.7 displays the Raman gain curve of our fused silica sample. The peak value of the Raman gain coefficient is checked for each set of data taken and, after correction for the depolarization ratio, the apparatus consistently returned a Raman gain coefficient of  $(0.9 \pm 0.2) \times 10^{-13}$  m/W at the peak, which is in good agreement with the two most commonly cited values near 1  $\mu$ m pump wavelength [23,37]. This is the first reported direct Raman gain measurement of any silicate material in the bulk form – every other measurement made has been done on fibers or using spontaneous Raman scattering to obtain a material Raman gain coefficient.

For each set of Raman gain data obtained for the test glasses, only the peak of the Raman gain spectrum at  $\Delta\nu = 13.2$  THz was checked for accuracy of the apparatus. The Raman gain coefficient for the peak of the fused silica sample consistently remained within the  $(0.9 \pm 0.2) \times 10^{-13}$  m/W value.



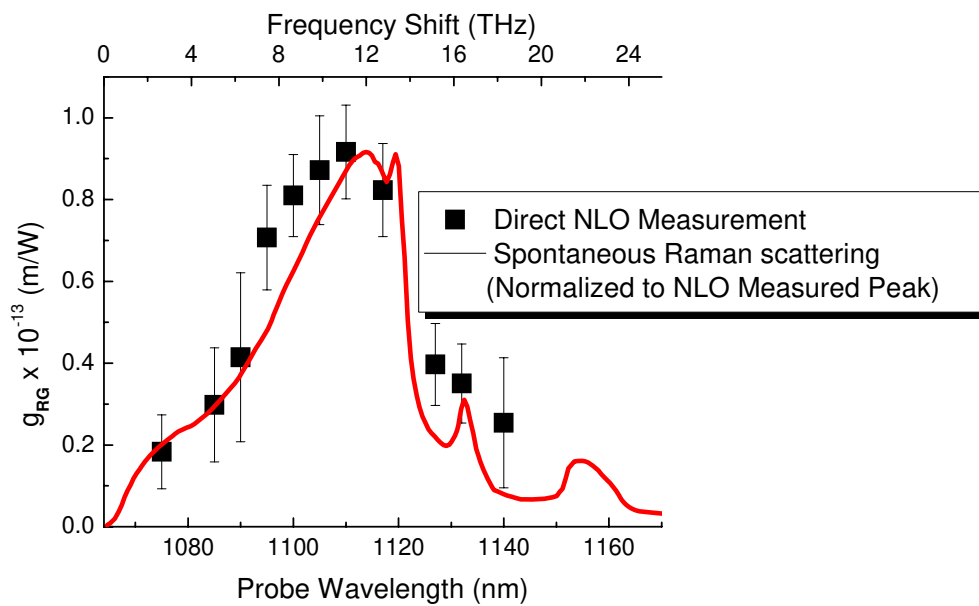


**Figure 3.7.** Raman gain spectrum of 3.18 mm thick pure fused silica sample

## CHAPTER FOUR: RAMAN GAIN MEASUREMENT OF PHOSPHATE AND CHALGONIDE GLASSES

In order to satisfy the stated goals of finding both broad bandwidth and high peak Raman gain coefficients, two different classes of glassy materials were investigated for their Raman gain performance. The first to be discussed will be phosphates. They were investigated due to their broadband response which can extend beyond  $\Delta\nu = 30$  THz ( $1000\text{ cm}^{-1}$ ). A systematic study was performed on four different phosphate glass families to determine what the spectral shape and the magnitude of the peak Raman gain can be obtained within these glasses. The phosphate study also included attempts to add other constituents in the glass matrix in order to try and provide the widest, flattest Raman gain profile possible within the same basic glass forming matrix.

The investigation of chalcogenide glasses was made in order to verify if the values reported in the literature of the ultra-fast irradiance-dependent nonlinear refractive index  $n_2$  approaching 1000 times higher than fused silica translates into similarly enormous values for material Raman gain coefficients [17]. The optical band gaps of chalcogenides begin in the visible part of the spectrum and extend into the near infrared as the composition is varied by including heavier constituents. This shifting of the band gap closer to the strong pump excitation at 1064 nm deteriorated the capability to make reliable Raman gain measurements with the apparatus described in Chapter 3 which uses a 1064 nm pump wavelength.

## 4.1 Borophosphate Raman Gain Data

The first attempt to explore the phosphate family was the investigation of the glass family with a composition given by  $[(100-x)\text{NaPO}_3-x\text{Na}_2\text{B}_4\text{O}_7]:\text{TiO}_2/\text{Nb}_2\text{O}_5=1$  in which the ratio of the phosphate ( $\text{PO}_3$ ) to the borate ( $\text{B}_4\text{O}_7$ ) concentration is varied [19]. Glasses in the system  $[(100-x)\text{NaPO}_3-x\text{Na}_2\text{B}_4\text{O}_7]:\text{TiO}_2/\text{Nb}_2\text{O}_5=1$ , where  $x = 5\%$ ,  $10\%$ , and  $13\%$  mole, were prepared from high purity raw materials:  $\text{NaPO}_3$  (99.99% Aldrich),  $\text{Na}_2\text{B}_4\text{O}_7$  (99.99% Aldrich),  $\text{TiO}_2$  (99.995% Alfa Aesar), and  $\text{Nb}_2\text{O}_5$  (99.998% Cerac). The glasses were melted under an oxygen atmosphere, in platinum crucibles at a temperature of  $1150^\circ\text{C}$ , for 5 minutes. After the melt, the glasses were quenched onto a pre-heated carbon plate, and annealed at a temperature  $40^\circ\text{C}$  below their glass transition temperature ( $T_g$ ). Finally, the glasses were cut and optically polished. This family of borophosphates has the molar concentration of  $\text{TiO}_2$  and  $\text{Nb}_2\text{O}_5$  set to 5% mole for each species. With a high amount of phosphate and relatively low amounts of  $d^0$  species ( $\text{TiO}_2$  and  $\text{Nb}_2\text{O}_5$ ) and boron content, one would expect the Raman gain curve of these glasses to be relatively broad and have a low Raman gain coefficient (although still larger than fused silica).  $\text{Ti}^{4+}$  and  $\text{Nb}^{5+}$  are known as  $d^0$  ions because they have an empty d-shell - such ions exhibit high polarizabilities. Therefore,  $\text{TiO}_2$  and  $\text{Nb}_2\text{O}_5$  were added into the borophosphate matrix to enhance the overall Raman polarizability of the glass.

Figure 4.1 shows the optical band edge as a function of increased boron content within the glass network. The position of the band edge moves to shorter wavelengths as the borophosphate concentration increases.

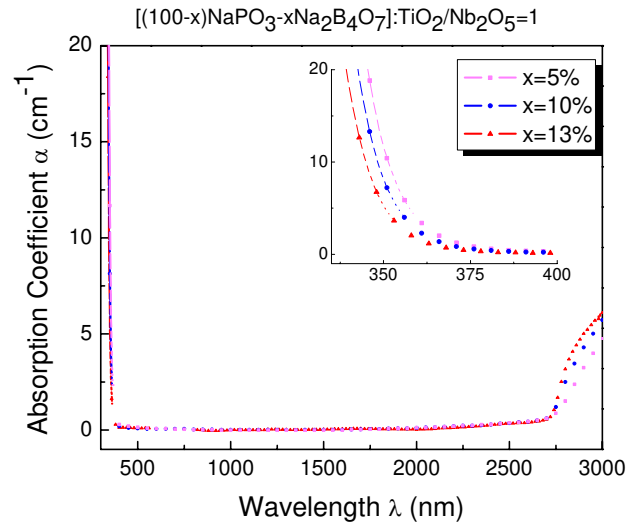


**Figure 4.1.** Optical band edge for the borophosphate family

Reproduced in Figure 4.2 are the Raman gain spectra for this family. Indeed these spectra suggest that relatively low values of the Raman gain coefficient can be obtained over a large bandwidth in a borophosphate versus a silica glass. Here a bandwidth of almost 40 THz was obtained, compared to single digit THz bandwidth in silica glass.

Although the main features in the Raman gain spectrum are reproduced by the spontaneous Raman spectrum, it is clear in these figures that there are some differences between the spontaneous and Raman gain spectra. The part of the discrepancy occurring for data points at low frequency shifts is caused by two factors. As discussed in the theory chapter, one reason is the “boson correction factor” associated with the increase in population of thermally excited phonons at low frequency shifts. As a result the scattered spectrum rises towards low frequency shifts. Another reason is the use of a holographic Rayleigh line rejection filter to eliminate the tail of the excitation line from the spontaneous spectrum at very small frequency shifts. This results in a false peak in the spontaneous Raman spectrum which rises higher than the true Raman gain response and

falls to zero faster at smaller wavelengths. The Raman gain spectrum in any material is expected to go to zero at the pump wavelength, but not as quickly as shown in the spontaneous Raman spectrum.

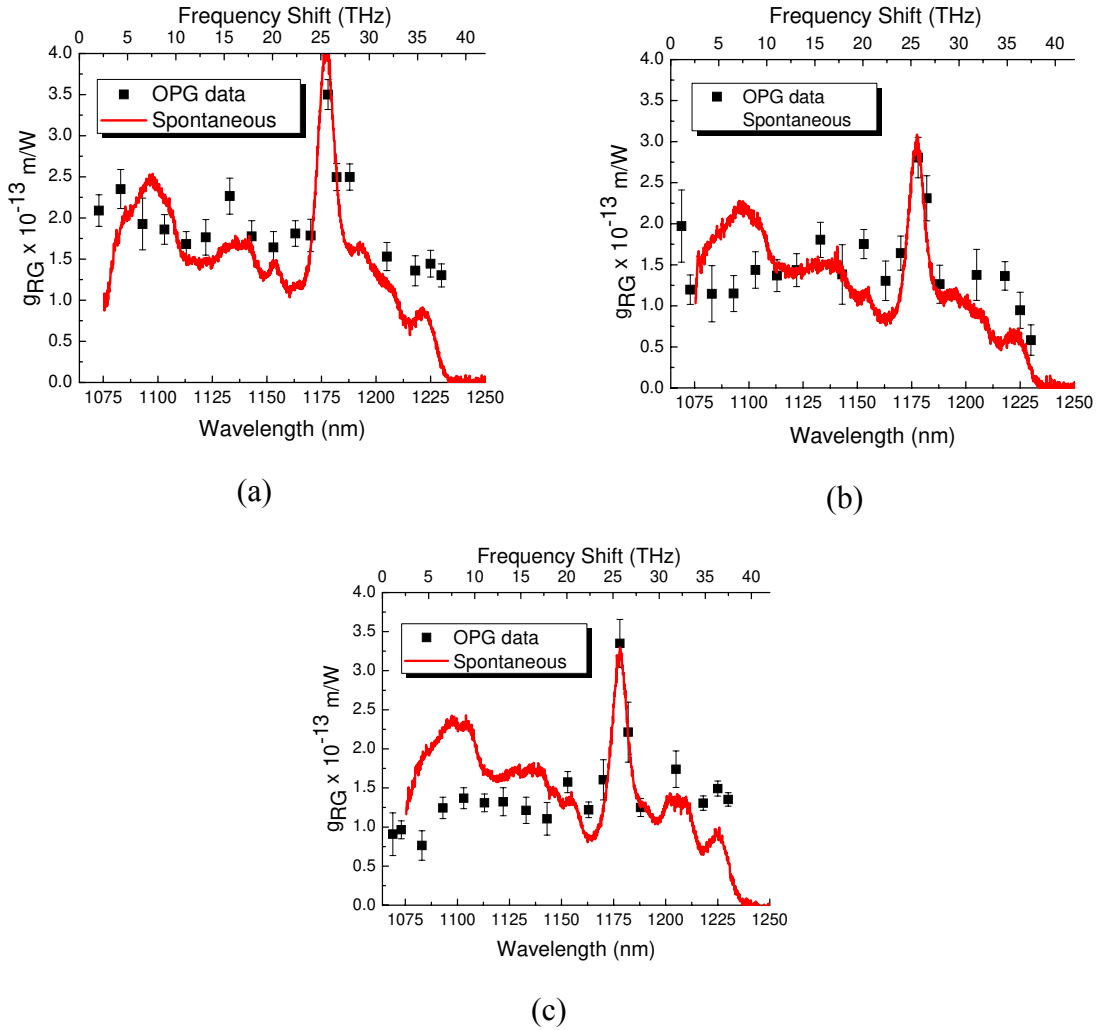


**Figure 4.2 (a) – (c).** Raman gain spectrum of borophosphate compositions of  $[(100 - x)\text{NaPO}_3 - x\text{Na}_2\text{B}_4\text{O}_7]:\text{TiO}_2/\text{Nb}_2\text{O}_5 = 1$  where (a)  $x = 13$ , (b)  $x = 10$ , and (c)  $x = 5\%$ . Overlaid are the spontaneous Raman spectrum taken at 632.8 nm. Values for  $\text{TiO}_2$  and  $\text{Nb}_2\text{O}_5$  are 5% mol for this glass family

The most dominant feature in these Raman gain spectra is the resonance near  $\Delta\nu = 27 \text{ THz}$ , which has been assigned to the Raman activity of isolated  $\text{NbO}_6$  units inside

the glass matrix [47]. Even at 5% mole concentration of  $\text{Nb}_2\text{O}_5$ , the isolated  $\text{NbO}_6$  units have the strongest vibrational contributions to the Raman response of these glasses because of their highly polarizable  $d^0$  ions.

## ***4.2 Binary Phosphate-Niobate Raman Gain Data***

A study was performed on a simple binary phosphate family that contained the composition  $(100-x)\text{NaPO}_3 - x\text{Nb}_2\text{O}_5$  in order to determine what was the maximum amount of Raman gain that could be obtained in a binary phosphate glass family that utilized highly polarizable  $d^0$  ions to increase the Raman activity of the glass. The compositions which were studied contained  $x = 10, 20, 30,$  and  $40\%$  of  $\text{Nb}_2\text{O}_5$ . A binary glass family was chosen to make it simple and reliable to deconvolve the individual Raman vibrational contributions by the phosphate constituents and the niobate constituents. Figure 4.3 displays the absorption data for this phosphate glass family. It is evident that the addition of niobate to the phosphate matrix leads to a progressively larger red shift of the absorption edge towards the visible part of the spectrum. Rivero has shown that this red shift in the absorption edge is also accompanied by an increase in the density, refractive index, and dispersion of this glass.

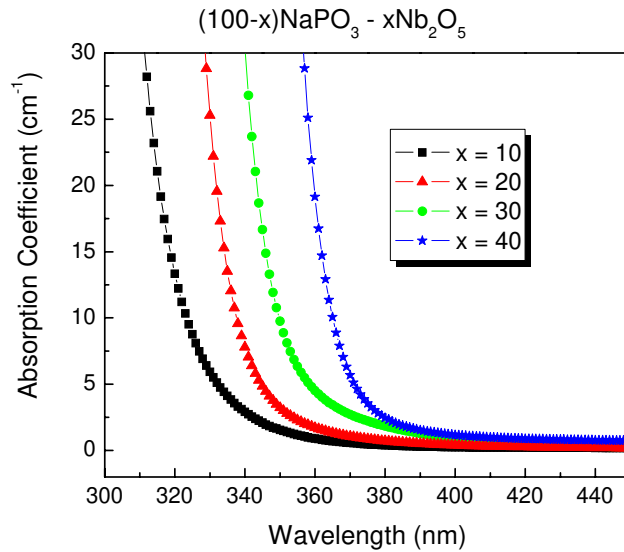
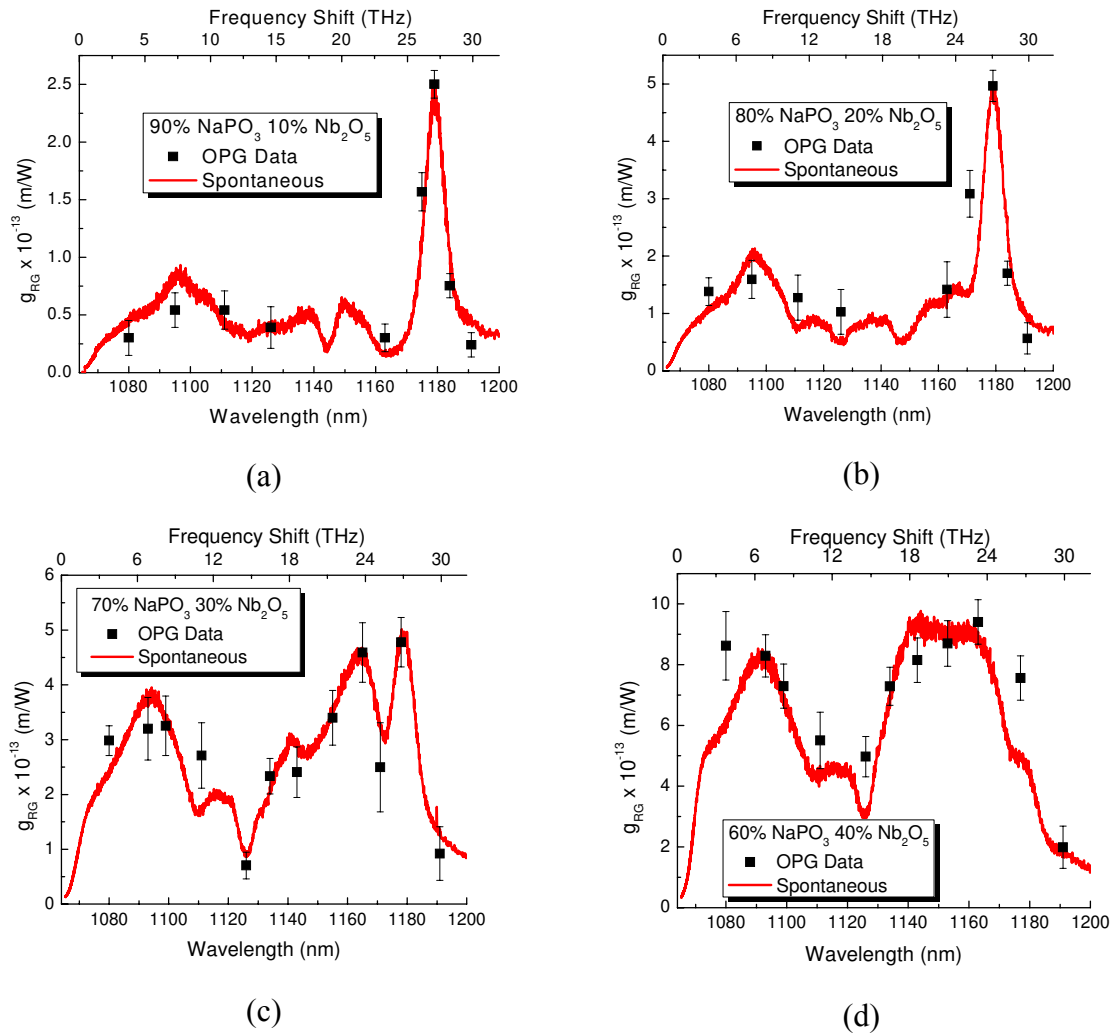


**Figure 4.3.** Wavelength dependence of the absorption coefficient of the binary phosphate-niobate family

The Raman gain curves for this glass family are shown in Figures 4.4 (a) – (d). The Raman vibration near  $\Delta\nu = 27$  THz is caused by isolated NbO<sub>6</sub> units inside the glass matrix as discussed previously [47]. The Raman gain value at this frequency shift first rises as the Nb<sub>2</sub>O<sub>5</sub> concentration is increased but then plateaus because further increases in the concentrations of Nb<sub>2</sub>O<sub>5</sub> in the glass cause Nb-O-Nb chains to preferentially start forming. These clusters remain isolated from the glass network. The Nb-O-Nb chains are responsible for the Raman vibration near  $\Delta\nu = 24$  THz and it is clear that this Raman gain coefficient increases with increasing Nb<sub>2</sub>O<sub>5</sub> in the glass [19,47]. As even more Nb<sub>2</sub>O<sub>5</sub> is introduced into the glass a continuous chain of NbO<sub>6</sub> units is linked together by the Nb-O-Nb bonds and this results in the creation of a Raman vibration near  $\Delta\nu = 19$  THz as seen in 60NaPO<sub>3</sub> - 40Nb<sub>2</sub>O<sub>5</sub> in Figure 4.4 (d) [19,47].



**Figures 4.4 (a) - (d).** Raman gain spectra of the binary phosphate niobate glasses with increasing niobate content. The spontaneous Raman spectra were taken at 514.5 nm and were overlaid over and normalized to the Raman gain data

The broadband Raman gain remains consistently small for small concentrations of Nb<sub>2</sub>O<sub>5</sub> in the glass matrix, but at concentrations above 20% Nb<sub>2</sub>O<sub>5</sub>, the total Raman gain increases quickly. This is consistent with the transition from isolated NbO<sub>6</sub> units for small Nb<sub>2</sub>O<sub>5</sub> concentrations, to the building of Nb-O-Nb bonds with isolated NbO<sub>6</sub> clusters, to a continuous network of NbO<sub>6</sub> units. It should be noted that with increasing amounts of Nb<sub>2</sub>O<sub>5</sub> in the glass, the agreement between the Raman gain data obtained at



1064 nm pumping and the spontaneous Raman scattering data obtained at 514.5 nm show increasing disagreement for the Raman vibration near  $\Delta\nu = 19$  THz. The reason for this discrepancy will be discussed later in Chapter 5. It is caused by the use of different pump wavelengths for the spontaneous versus Raman gain spectra.

Table 4.1 summarizes the Raman gain coefficients for the three niobate vibrations in these glasses. Peak Raman gain coefficients approaching ten times higher than the peak of fused silica are available in this family of glasses. All of the stated values have error bars of 10% or less.

**Table 4.1.** Raman gain coefficients for the three main Raman active vibrations in the  $\text{NaPO}_3 - \text{Nb}_2\text{O}_5$  glass system

	$g_{\text{RG}} \times 10^{-13} \text{ m/W}$ $\Delta\nu = 26 \text{ THz}$	$g_{\text{RG}} \times 10^{-13} \text{ m/W}$ $\Delta\nu = 24 \text{ THz}$	$g_{\text{RG}} \times 10^{-13} \text{ m/W}$ $\Delta\nu = 19 \text{ THz}$
90 $\text{NaPO}_3 - 10\text{Nb}_2\text{O}_5$	2.5	0.3	N/A
80 $\text{NaPO}_3 - 20\text{Nb}_2\text{O}_5$	5	1.1	N/A
70 $\text{NaPO}_3 - 30\text{Nb}_2\text{O}_5$	4.8	4.5	3.5
60 $\text{NaPO}_3 - 30\text{Nb}_2\text{O}_5$	7.6	8.0	9.6

### 4.3 Cation Exchange Phosphate Raman Gain Data

After exploring the Raman gain spectra of binary phosphate-niobate glasses, an effort was made to characterize what effects were introduced by changing the cation in the glass matrix had on the Raman gain strength and spectrum of a similar glass family. Cations such as  $\text{Na}^+$ ,  $\text{K}^+$ ,  $\text{Ca}^{2+}$  and  $\text{Ba}^{2+}$  are modifiers of the glass matrix and hence have a large impact on the vibrational modes. Five samples were prepared and tested. Figure 4.5 shows the absorption spectra and compositions of the cation exchange phosphate glasses. Examining Figure 4.5 it can be noted that cations (both alkali and alkaline earth)

which are atomically lighter cause the band edge to move more into the visible part of the spectrum, as evidenced by the replacement of  $\text{Ca}^{2+}$  with  $\text{Ba}^{2+}$  alkaline earth ions and  $\text{Na}^+$  ions with  $\text{K}^+$  alkali ions. Note, however, that the absorption edges are all quite deep in the UV and deep blue regions of the spectrum and the Raman spectra are not expected to show any significant enhancements for 514.5 nm pump beam excitation.

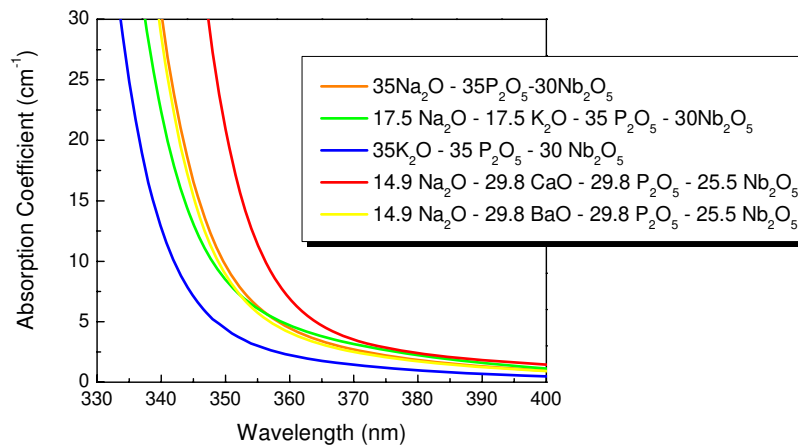
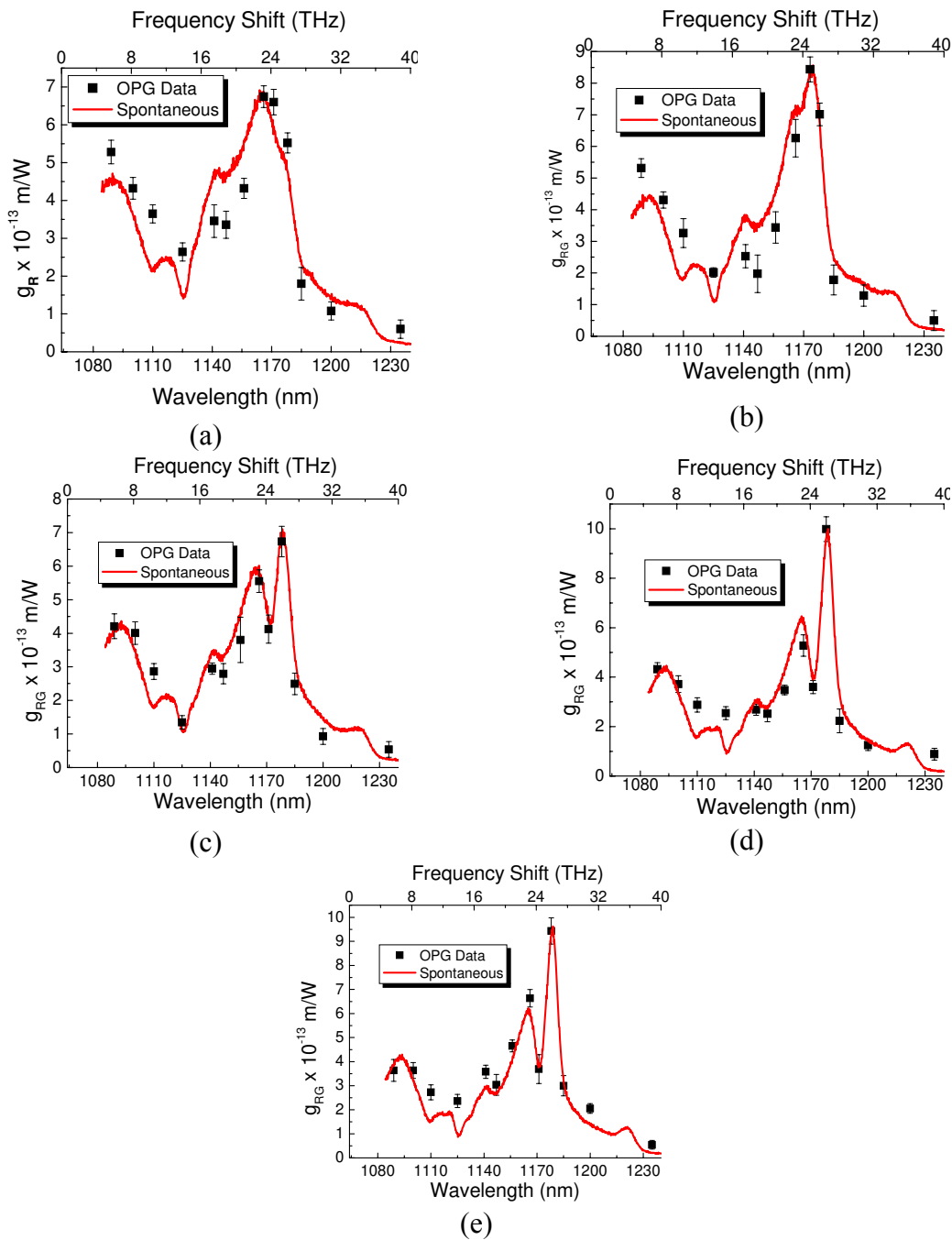


**Figure 4.5.** Absorption band edge of cation exchange glasses with compositions given in the legend of the figure

Figures 4.6 (a) – (e) show the Raman gain spectra of the glasses obtained with 1064 nm pump excitation. The spontaneous Raman data obtained at 514.5 nm is overlaid and normalized to the peak in the Raman gain data.



**Figures 4.6 (a) – (e).** Raman gain of spectra of (a)  $14.9\text{Na}_2\text{O} - 29.8\text{CaO} - 29.8\text{P}_2\text{O}_5 - 25.5\text{Nb}_2\text{O}_5$ , (b)  $14.9\text{Na}_2\text{O} - 29.8\text{BaO} - 29.8\text{P}_2\text{O}_5 - 25.5\text{Nb}_2\text{O}_5$ , (c)  $35\text{Na}_2\text{O} - 35\text{P}_2\text{O}_5 - 30\text{Nb}_2\text{O}_5$ , (d)  $17.5\text{Na}_2\text{O} - 17.5\text{K}_2\text{O} - 30\text{Nb}_2\text{O}_5$ , and (e)  $35\text{K}_2\text{O} - 35\text{P}_2\text{O}_5 - 30\text{Nb}_2\text{O}_5$

The most obvious difference is the change in the overall shape of the Raman gain spectrum when moving from a purely alkali ion ( $\text{Na}^+$  and  $\text{K}^+$ ) to a mix of alkali and alkaline earth ions such as  $\text{Ca}^{2+}$  and  $\text{Ba}^{2+}$ . The Raman gain shape changes from a profile mostly dominated by the  $\text{NbO}_6$  vibrations discussed in the previous section to a modified Raman gain profile. This would suggest that the role of the alkali ions  $\text{Na}^+$  and  $\text{K}^+$  is to interact in very similar ways in the overall glass matrix, while the alkaline earth ions  $\text{Ca}^{2+}$  and  $\text{Ba}^{2+}$  interact differently with the  $\text{NbO}_6$  units in the glass structure.

The increasing peak Raman gain near  $\Delta\nu = 26$  THz of the  $35\text{K}_2\text{O} - 35\text{P}_2\text{O}_5 - 30\text{Nb}_2\text{O}_5$  glass, transitioning to the  $17.5\text{Na}_2\text{O} - 17.5\text{K}_2\text{O} - 30\text{Nb}_2\text{O}_5$  glass, and finally to the  $35\text{Na}_2\text{O} - 35\text{P}_2\text{O}_5 - 30\text{Nb}_2\text{O}_5$  glass can be rationalized by recognizing that potassium is a heavier element than sodium and has more weakly bound electrons available to participate in the interaction with the optical wave. Additionally, an increasing larger discrepancy between the spontaneous Raman and Raman gain spectra appears near the Raman active mode at frequency shifts below the  $\Delta\nu = 19$  THz as the compositions move from purely alkali ions ( $\text{Na}^+$  and  $\text{K}^+$ ) toward heavier alkali and alkaline earth ions ( $\text{Ca}^{2+}$  and  $\text{Ba}^{2+}$ ). This has not been completely interpreted at this time and probably occurs due to a difference in the interaction between alkali ions and alkali earth ions and the glass matrix. The peak Raman gain coefficients available in these glasses are approximately 10 times higher than the peak coefficient of fused silica, but with less spectral flatness than the gain bandwidth offered by the binary phosphate-niobate glasses previously discussed.

#### ***4.4 Raman Gain Data on Broadband Phosphates for Attempts Towards Spectrally Flattened Gain Profiles***

A common characteristic found in each of the Raman gain data in Figures 4.4 and 4.6 is the lack of a significant Raman active mode near  $\Delta\nu = 11 - 15$  THz. Although the main Raman active mode in fused silica lies in this spectral region, the amplitude of this fused silica Raman active mode is roughly equal to the magnitude of the response of the phosphate glasses without the presence of fused silica. The search for a more Raman active material in this spectral region could potentially lead to a more spectrally flat Raman gain curve if a stable glass can be formed with this material. Figure 4.7 depicts spontaneous Raman scattering data obtained by Rivero which shows that a phosphate-antimony glass contains the necessary Raman active vibration near  $\Delta\nu = 11 - 15$  THz. This stimulated an attempt to incorporate  $\text{Sb}_2\text{O}_3$  into a borophosphate glass composition to achieve spectral uniformity in the Raman gain curve.

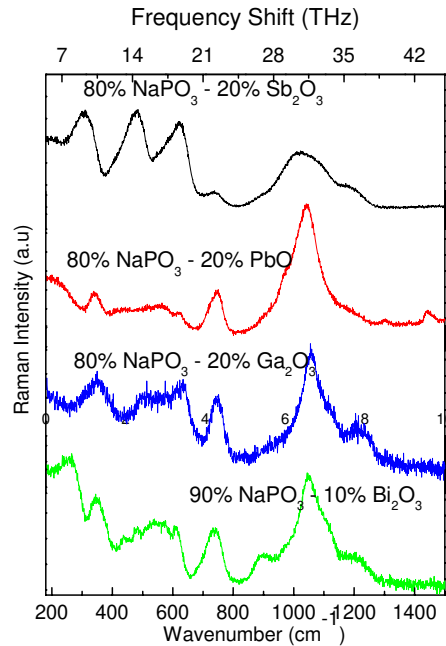


**Figure 4.7.** Raman active modes of various binary phosphate glasses. 80NaPO<sub>3</sub> – 20Sb<sub>2</sub>O<sub>3</sub> (black line) displays the desired Raman active mode near  $\Delta\nu = 13 - 15$  THz. The spontaneous Raman was data taken with a 633 nm pump wavelength

The absorption band edges and the exact compositions for the glasses fabricated and investigated are shown in Figure 4.8. The compositions are essentially borophosphates that include moderate amounts of TiO<sub>2</sub>, Nb<sub>2</sub>O<sub>5</sub>, and Sb<sub>2</sub>O<sub>3</sub> additives. The absorption band edges are no less than 400 nm for these glasses and therefore have a yellowish color. The movement of the absorption band edge further into the visible is attributed to increasingly smaller amounts of borophosphate and increasing amounts of TiO<sub>2</sub> and Nb<sub>2</sub>O<sub>5</sub> while the amount of Sb<sub>2</sub>O<sub>3</sub> is kept constant.

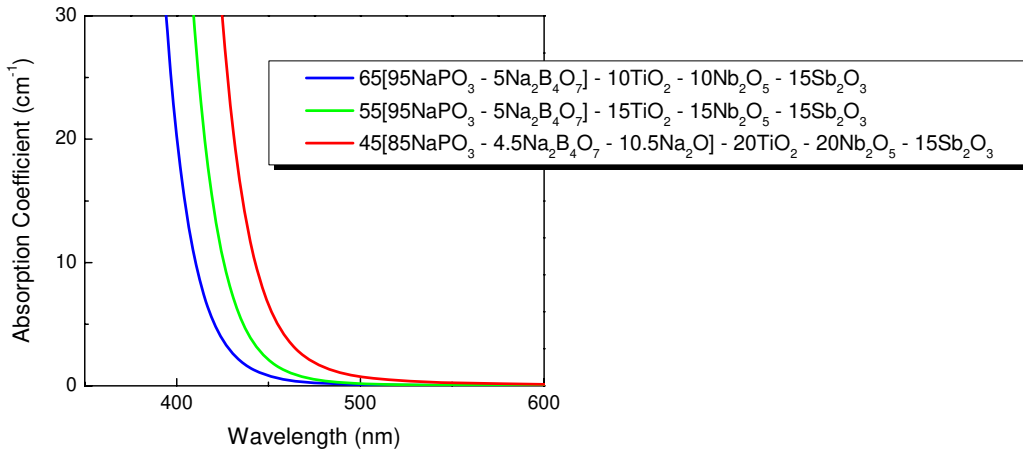
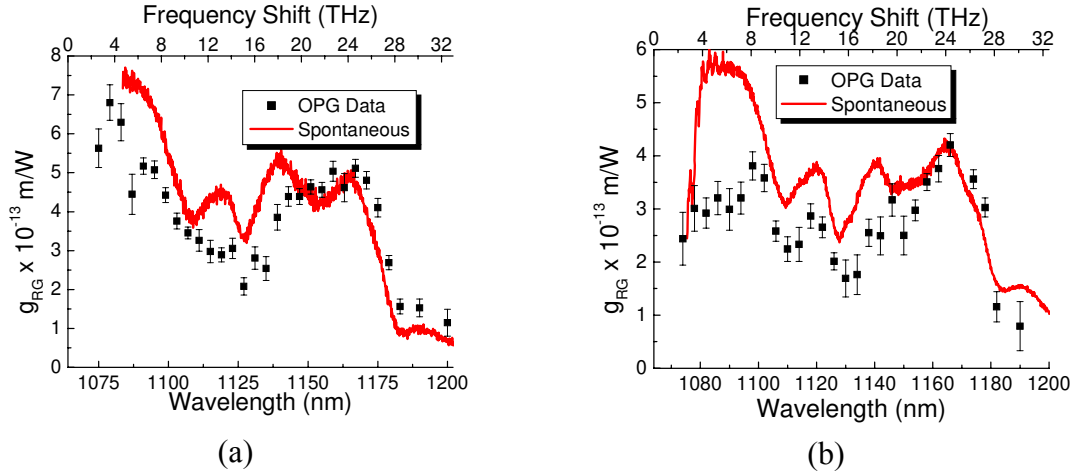


**Figure 4.8.** Absorption band edge of borophosphate glass with constant  $\text{Sb}_2\text{O}_3$  content and increasing  $\text{TiO}_2$  and  $\text{Nb}_2\text{O}_5$  content

The Raman gain data for these compositions is depicted in Figures 4.9 (a) & (b). The spontaneous Raman scattering spectra obtained at 633 nm is overlaid and normalized to the Raman gain data. Reliable Raman gain data was not obtained for the composition  $65[95\text{NaPO}_3 - 5\text{Na}_2\text{B}_4\text{O}_7] - 10\text{TiO}_2 - 10\text{Nb}_2\text{O}_5 - 15\text{Sb}_2\text{O}_3$  because of scattering losses due to poor optical surface quality and/or inhomogeneity of the glass. As the absorption band edge moves further into the visible and closer to the excitation wavelength used in the spontaneous Raman scattering experiment, there appears to be increasing disagreement between the spontaneous Raman and Raman gain data. This is consistent with the results of the binary phosphate-niobate and cation-exchange glasses previously reported. The low frequency shift content of these glasses deserves discussion due to the inability of the spontaneous Raman scattering experiment to capture the details close to the pump wavelength.



**Figures 4.9 (a) & (b).** Raman gain curves of (a)  $45[85\text{NaPO}_3 - 4.5\text{Na}_2\text{B}_4\text{O}_7 - 10.5\text{Na}_2\text{O}] - 20\text{TiO}_2 - 20\text{Nb}_2\text{O}_5 - 15\text{Sb}_2\text{O}_3$  and (b)  $55[95\text{NaPO}_3 - 5\text{Na}_2\text{B}_4\text{O}_7] - 15\text{TiO}_2 - 15\text{Nb}_2\text{O}_5 - 15\text{Sb}_2\text{O}_3$ . The spontaneous Raman spectrum obtained with a pump wavelength of 633 nm is overlaid for comparison

The low frequency Raman scattering spectra ( $\Delta\nu < 8$  THz) of these glasses due to the heavy masses of the  $d^0$  ions  $\text{Ti}^{4+}$  and  $\text{Nb}^{5+}$  is expected to be considerably larger than that for lighter Raman active materials such as  $\text{SiO}_2$ . The increase in low frequency Raman scattering would be expected to increase for increased heavy metal content as depicted in Figures 4.9 (a) & (b). The cause for the additional increase in low frequency Raman gain for the glass in Figure 4.9 (a) with respect to its spontaneous Raman scattering data, as compared to the same case for Figure 4.9 (b), is not known. It can be speculated that the heavier constituents of  $\text{TiO}_2$ ,  $\text{Sb}_2\text{O}_3$ , and  $\text{Nb}_2\text{O}_5$  may have Raman active modes at low frequency shifts which cannot be resolved by spontaneous Raman scattering experiments.



## 4.5 Raman Gain Measurements of Chalcogenide Glasses

Chalcogenide glasses have been shown to have the highest nonlinearities of all glasses reported to date in the literature. Cardinal et al. reported measurements of  $n_2$  using femtosecond pulses and discovered values for  $n_2$  starting around 80 times higher than fused silica for  $\text{As}_2\text{S}_3$  [28]. They speculated that  $n_2$  could approach 400-500 times higher than that of fused silica for  $\text{As}_2\text{Se}_3$ . Harbold et al performed a systematic study on chalcogenide glass in an attempt to optimize the material properties for use in nonlinear switching utilizing a nonlinear phase shift per unit distance defined as

$$\Delta\phi = k_0 n_2 I, \quad (4.1)$$

where  $\Delta\phi$  is the nonlinear phase shift per unit length of propagation,  $k_0$  is the wave vector,  $n_2$  is the nonlinear refractive index, and  $I$  is the irradiance of the optical beam [29]. Slusher et al reported that a maximum FOM can be obtained by finding a material that has an optical band gap that is related to the operating frequency given by  $h\nu = 0.41E_g$  where  $h$  is Planck's constant,  $\nu$  is the optical frequency, and  $E_g$  is the optical band gap of the material. Slusher et al also reported on a small-core nearly stoichiometric  $\text{As}_2\text{Se}_3$  fiber which yielded a value of  $n_2$  930 times higher than that of fused silica at 1.53  $\mu\text{m}$  and a peak Raman gain coefficient approaching 780 times higher than fused silica at a frequency shift near  $\Delta\nu = 7$  THz at 1606 nm [17]. These estimates were larger by about a factor of two than the theoretical predictions performed on the same glass and fiber design. Error bars approaching 30% were stated due to uncertainties in effective areas of the fiber, coupling losses, and the multimode nature of the fiber.

Spurred on by these large reports of nonlinearities in chalcogenide glass, several different families of chalcogenide glass were tested for their Raman gain performance

with pumping at 1064 nm. Modifications to the apparatus described in Chapter 3 were necessary in order to make measurements on chalcogenide glasses. Figure 3.2 is repeated here and relabeled as Figure 4.10 for ease of referring to a diagram when describing the changes made to the apparatus.

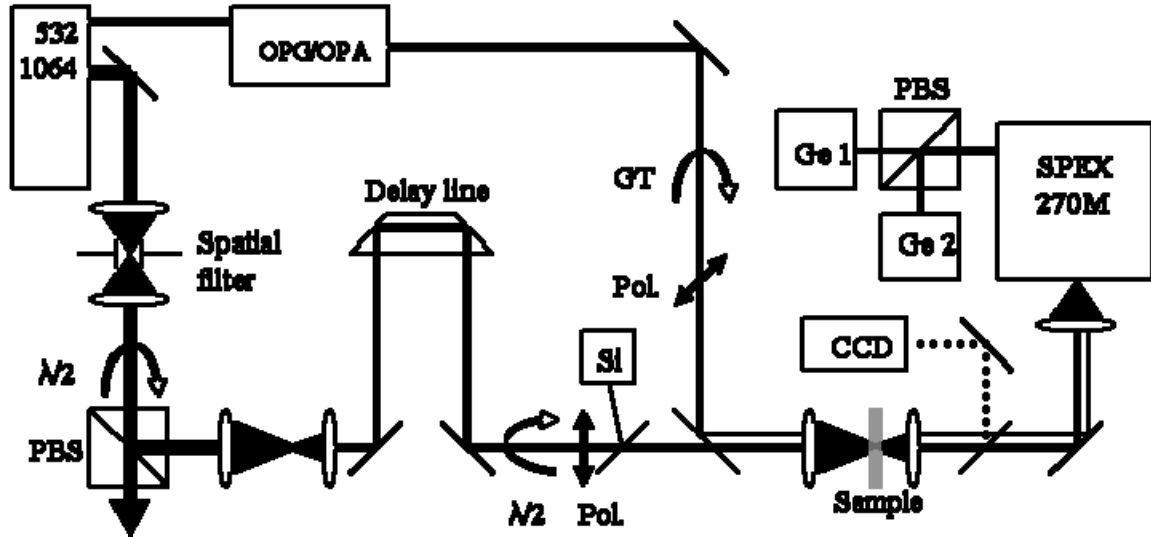


Figure 4.10. Apparatus used for Raman gain measurements on bulk glass samples

A neutral density filter with an absorption coefficient of  $\alpha \approx 10 \text{ cm}^{-1}$  at 1064 nm was inserted before the 28 cm focusing lens located in front of the sample. This filter was necessary in order to reduce the amount of energy in both the signal and pump inside the sample to avoid other linear and nonlinear effects from masking the Raman gain process. In order to maintain accurate detection and good signal-to-noise ratios, the neutral density filters after the sample and before the flip-mount mirror was removed. This enabled the boxcar amplification settings to only be doubled, *viz.* from 20mV/V to 10mV/V of amplification, to maintain accurate detection. A new calibration curve for the

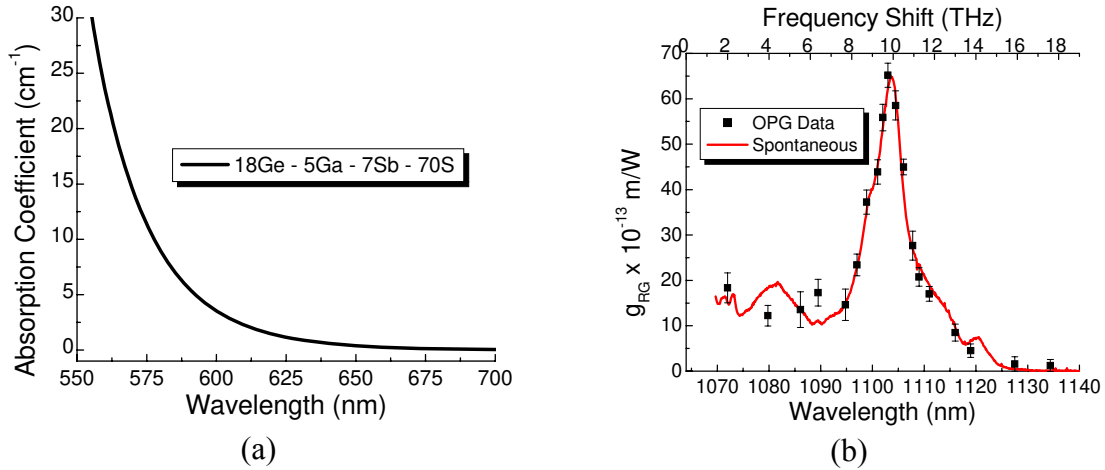
voltage read by the boxcar for the pump detector vs. the energy at the sample was generated and used in the calculations.

The first chalcogenides investigated belonged to the family  $18\text{Ge} - 5\text{Ga} - 7\text{Sb} - (70-x)\text{S} - x\text{Se}$ . Compositions with  $x = 0, 5, 20, 50,$  and  $70$  were investigated. The absorption spectrum for the composition  $18\text{Ge} - 5\text{Ga} - 7\text{Sb} - 70\text{S}$  is displayed in Figure 4.11 (a). Note that the absorption spectrum extends well into the near infrared making useful measurements of the spontaneous Raman spectrum in the visible and ratioing it to the fused silica spectrum not valid for obtaining a non-resonant Raman gain coefficient. Due to these long absorption tails it is probable that the Raman gain at 1064 nm also was somewhat resonantly enhanced.

The Raman data was taken with the modified apparatus using the 1064 nm pump. The spontaneous Raman data obtained at 633 nm is normalized to the peak of the gain data in Figure 4.11 (b). The agreement is reasonable since the Raman spectrum is dominated by a single line (just as in fused silica). The reasons will be discussed later in Chapter 5.

Attempts to measure the Raman gain *spectrum* in the other samples were unsuccessful. Surface scattering made Raman gain measurements on the composition  $18\text{Ge} - 5\text{Ga} - 7\text{Sb} - 65\text{S} - 5\text{Se}$  unreliable. The effects of photodarkening dominated the light-material interaction and did not allow reliable Raman gain spectra on compositions with selenium content higher than  $x = 20$ . These effects are shown in Figures 4.12 (a) – (d). The reduction in the amount of signal measured on transmission through the sample is shown as a function of pump detector voltage (and hence pump energy) in the sample. The effect of replacing sulfur with selenium in chalcogenides has been shown to move

the optical band edge to longer wavelengths. This moves the band edge closer to the pump wavelength of 1064 nm and the effects of two photon absorption can become significant since the band edge of the 18Ge – 5Ga – 7Sb – 70S glass already approaches half of the pump wavelength.

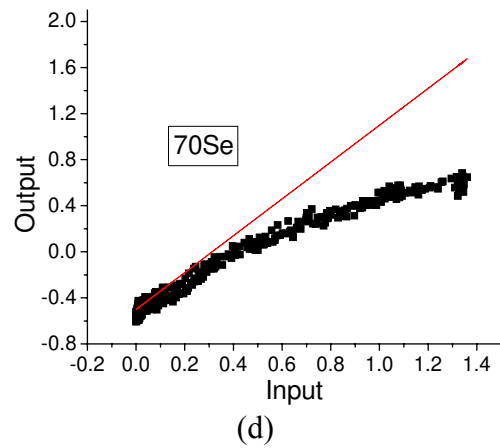
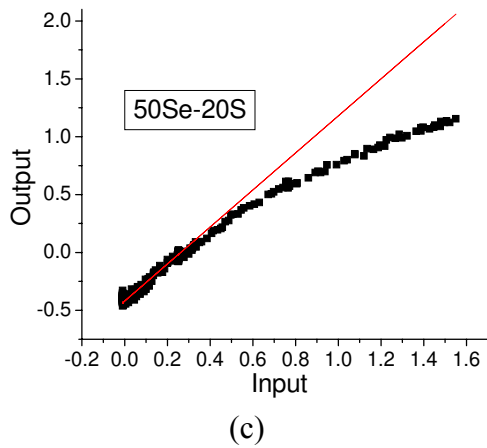
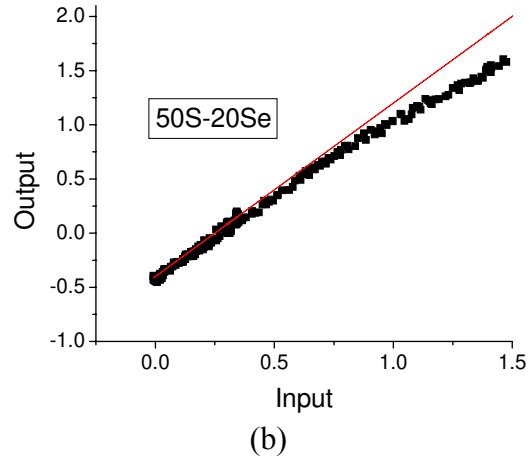
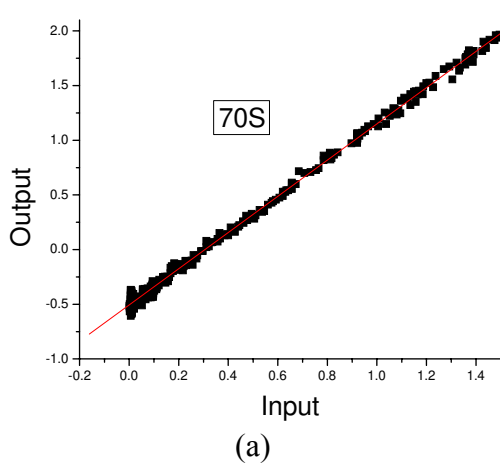


**Figures 4.11 (a) & (b).** (a) Absorption spectrum and (b) the Raman gain curve of 18Ge – 5Ga – 7Sb – 70S. The spontaneous Raman data was obtained at 633 nm and is normalized to the peak of the measured Raman gain spectrum using 1064 nm pumping

An attempt was made to make Raman gain measurements on the family 18Ge – 5Ga – 7Sb – (70-x)S – xSe with  $x = 0, 2,$  and  $5$ . Only the peak of the Raman gain spectrum located near  $\Delta\nu \approx 10$  THz was measured reliably because it required the smallest peak powers which minimized the photodarkening effect. The results for the peak Raman gain coefficient located near  $\Delta\nu \approx 10$  THz are listed in Table 4.2. All of the error bars are  $\pm 15\%$  or less in these measurements.

**Table 4.2.** Peak Raman gain coefficient found in the family 18Ge – 5Ga – 7Sb – (70-x)S – xSe with  $x = 0, 2,$  and  $5\%$

	18 Ge-5Ga-7Sb-70S	18Ge-5Ga-7Sb-68S-2Se	18Ge-5Ga-7Sb-65S-5Se
$g_{RG} \times 10^{-13} \text{ m/W}$ @ $\Delta\nu \approx 10 \text{ THz}$	65	67	72



**Figures 4.12 (a) – (d).** The pulsed 1064 nm incident pump is plotted versus the transmitted signal energy in chalcogenide samples with (a) 70S, (b) 50S – 20Se, (c) 20S – 50Se, and (d) 70Se. The photodarkening effect clearly takes place as the heavier selenium atoms replace the sulfur atoms in the glass network

The peak Raman gain coefficient of  $g_{RG} = (72 \pm 10) \times 10^{-13}$  m/W is the highest measured to date of any of the glasses studied in this project.

## CHAPTER FIVE: RAMAN GAIN MEASUREMENTS IN TELLURITE GLASSES

Tellurite glass holds great promise for high peak Raman gain coefficients if the assumption is made that increased Raman gain coefficients scale roughly with the value of  $n_2$ , the irradiance-dependent refractive index in glasses. Previous work on tellurite glass is based on the systematic studies performed by French researchers on the magnitude of  $n_2$  at 1.5  $\mu\text{m}$  and contributions by the Japanese using spontaneous Raman scattering as an analytical tool to correlate glass structure to certain highly polarizable Raman bands [30,48]. Interestingly enough, the Raman gain measurements utilizing the direct NLO measurement technique at 1064 nm on tellurite glass sparked a controversy within the literature among several different groups investigating the tellurites as prospective materials to be used as a Fiber Raman Amplifiers (FRA) in the optical telecommunications bands. Resolution to the discrepancy between Raman gain data obtained with 1064 nm pumping and the values obtained with lasers in the visible part of the spectrum was reported by Rivero et al and will be discussed in the last section of this chapter [22].

In this work, several different families of tellurite glass were investigated in order to determine the effect of adding a variety of highly polarizable constituents, for example additional  $ns^2$  species such as  $\text{Tl}^+$ ,  $\text{Pb}^{2+}$ , or  $\text{Bi}^{3+}$  and/or  $d^0$  ions such as  $\text{Ti}^{4+}$ ,  $\text{Nb}^{5+}$ , and  $\text{W}^{6+}$  to the tellurite glass. The presence of Lewis  $ns^2$  lone pair electrons in the electronic configuration, such as in the case of Te, Tl, and Pb, can also further enhance the nonlinear response of the material due to the strong coupling of the electric field with

these free pairs of electrons. In this case, one can speculate that the incorporation of such components into the glass can function as intermediate and/or modifier species to the tellurite structural network. Certain compositions provided peak material Raman gain coefficients over 50 times higher than the peak of fused silica, which are the highest non-resonantly enhanced material Raman gain coefficients reported in oxide based glasses in the literature to date.

### ***5.1 Raman Gain Measurements of Binary Tellurium-Thallium Oxide Glass***

Baughner et al showed that thallium oxide ( $\text{TlO}_{0.5}$ ) is a highly polarizable Lewis  $ns^2$  lone pair electron donor due to its partial covalency [49]. In combination with  $\text{TeO}_2$ , a binary glass with  $\text{TlO}_{0.5}$  forms a stable region for  $(100-x)\text{TeO}_2 - x\text{TlO}_{0.5}$  for compositions where  $x$  can range from a few percent all the way past 50%. Since  $\text{TlO}_{0.5}$  is not Raman active above frequency shifts of  $\Delta\nu = 6$  THz, investigating the Raman gain spectra of binary  $\text{TeO}_2 - \text{TlO}_{0.5}$  glass system can provide insight as to the correlation between the absolute intensity of Raman active bands and the structural relationship of  $\text{TeO}_2$  based glass according to the analysis by Sekiya [48]. In the context of this work, a series of five binary glasses with compositions  $(100-x)\text{TeO}_2 - x\text{TlO}_{0.5}$  with  $x = 20, 25, 30, 40,$  and  $50$  were tested for their Raman gain performance and to provide a basic structural analysis ranging from a  $\text{TeO}_2$  rich glass to a relatively weak  $\text{TeO}_2$  network.

Figure 5.1 shows the absorption band edge of the binary  $\text{TeO}_2 - \text{TlO}_{0.5}$  glasses. An interesting phenomenon occurs as the amount of thallium is increased at the expense of the amount of tellurium in the glass. The band edge remains approximately constant

for  $75\text{TeO}_2 - 25\text{TlO}_{0.5}$  and  $70\text{TeO}_2 - 30\text{TlO}_{0.5}$ , then decreases by 25 nm for  $60\text{TeO}_2 - 40\text{TlO}_{0.5}$ , and finally increases 50 nm for the  $50\text{TeO}_2 - 50\text{TlO}_{0.5}$  glass. However, Rivero has shown that the density monotonically increases for increasing thallium content, yet the index of refraction drops by 15% when progressing from  $60\text{TeO}_2 - 40\text{TlO}_{0.5}$  to  $50\text{TeO}_2 - 50\text{TlO}_{0.5}$  [34]. The meaning of this data has yet to be explained by glass scientists.

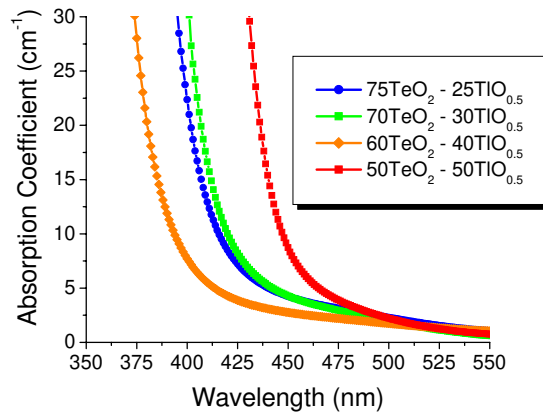


**Figure 5.1.** Absorption spectra of a series of binary  $\text{TeO}_2 - \text{TlO}_{0.5}$  glasses

The damage threshold of the binary  $\text{TeO}_2\text{-TlO}_{0.5}$  glasses was low enough to produce unreliable data away from the main  $\Delta\nu = 20$  THz and  $\Delta\nu = 21.3$  THz peaks in the Raman gain spectrum. Most attempts to measure Raman gain away from these main peaks resulted in surface optical damage after less than five minutes of exposure to the 10 Hz system. Nevertheless, Raman gain measurements were made over the  $\Delta\nu = 20$  THz and  $\Delta\nu = 21.3$  THz bands for all four binary compositions and agree with structural variation analysis of these glasses. Figure 5.2 depicts the spontaneous Raman scattering curve for  $50\text{TeO}_2 - 50\text{TlO}_{0.5}$  and overlaid are the two Raman gain data points. The spontaneous Raman scattering data is *not* normalized to the Raman gain data in this



figure – the absolute Raman scattering cross-section taken at 1064 nm is used for comparison.

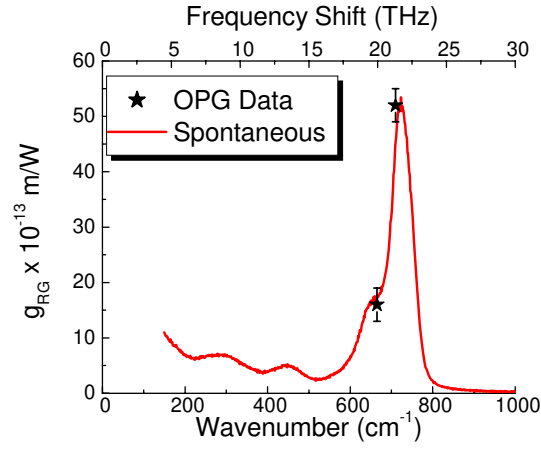


**Figure 5.2.** Raman gain data points for the  $\Delta\nu = 20$  THz and  $\Delta\nu = 21.3$  THz peaks and absolute spontaneous Raman cross-section taken at 1064 nm overlaid for comparison for  $50\text{TeO}_2 - 50\text{TlO}_{0.5}$

In essence, a tellurium rich glass contains many  $\text{TeO}_4$  disphenoids with the lone pair electrons so directed as to constitute the third equatorial corner of a  $\text{TeO}_4\text{E}$  trigonal bi-pyramid; these are the most polarizable entities in the glass network and are responsible for the  $\Delta\nu = 20$  THz vibration as shown by *ab initio* calculations [50]. By combining another structural unit to the glass matrix that also has a Lewis  $ns^2$  lone pair, it can be anticipated that the nonlinearity of the glass can increase due to strengthened stereochemical activity [30]. As the mole % of tellurium decreases, the  $\text{TeO}_4$  units distort to form  $\text{TeO}_{3+1}$  units and then to  $\text{TeO}_3$  units, which have vibrational resonances at a frequency shift near 21.3 THz [48]. This last large resonance, which is stronger than the  $\text{TeO}_4$  vibrational resonance in these glasses, should be related to the presence of thallium ions in the vicinity of the  $\text{TeO}_3$  and  $\text{TeO}_{3+1}$  units. In this frequency range, no Raman band could be related to the presence of thallium oxide groups. NMR investigations are ongoing to evaluate the thallium ion environment in these glasses.

As the ratio of tellurium oxide to thallium oxide is varied, the peak magnitudes of the Raman gain coefficients at the  $\Delta\nu = 20$  THz and  $\Delta\nu = 21.3$  THz bands change. A peak Raman gain coefficient of  $(52 \pm 3)$  times that of the peak Raman gain of the fused silica sample was obtained for the binary sample containing 50% mole of  $\text{TlO}_{0.5}$ . This represents the highest *directly* measured and reported peak Raman gain coefficient to date in oxide glasses known to the author [18]. With the band edges below 500 nm for all of the samples tested, it is reasonable to expect similar performance at the telecommunication wavelengths of 1280-1625 nm because the Raman gain measurements were made with 1064 nm pumping which avoids any resonantly enhanced Raman effects. (Of course, however, the standard wavelength correction by which  $g_{\text{RG}}$  varies inversely with wavelength  $\lambda$  must be applied to obtain  $g_{\text{RG}}$  at communications wavelengths.) Furthermore, the increased peak Raman gain coefficient with increasing thallium oxide content reported here shows a trend of increasing non-resonant nonlinearity with increasing thallium content in the glass matrix. Table 5.1 summarizes the peak Raman gain coefficients and the surface optical damage thresholds for these glasses at the peaks associated with the  $\Delta\nu = 20$  THz and  $\Delta\nu = 21.3$  THz resonances.

**Table 5.1.** Raman gain coefficients for binary  $\text{TeO}_2 - \text{TlO}_{0.5}$  glass system at  $\Delta\nu = 20$  THz and  $\Delta\nu = 21.3$  THz and optical surface damage thresholds at 1064 nm

	$g_{\text{RG}} \times 10^{-13}$ m/W $\Delta\nu = 20$ THz	$g_{\text{RG}} \times 10^{-13}$ m/W $\Delta\nu = 21.3$ THz	Optical surface damage threshold ( $\text{GW}/\text{cm}^2$ )
75 $\text{TeO}_2 - 25\text{TlO}_{0.5}$	25 $\pm$ 4	19 $\pm$ 3	3.6
70 $\text{TeO}_2 - 30\text{TlO}_{0.5}$	21 $\pm$ 4	23 $\pm$ 5	4.4
60 $\text{TeO}_2 - 40\text{TlO}_{0.5}$	21 $\pm$ 5	30 $\pm$ 7	4.0
50 $\text{TeO}_2 - 50\text{TlO}_{0.5}$	16 $\pm$ 3	52 $\pm$ 3	5.1

## 5.2 Raman Gain Measurements of Tellurite Glass with Ternary Lewis $ns^2$ Lone Pair Electrons

Increased Raman gain coefficients in binary  $\text{TeO}_2 - \text{TlO}_{0.5}$  glasses help to confirm the theory that the increased stereochemical activity of Lewis  $ns^2$  lone pair species when in the vicinity of distorted  $\text{TeO}_4$  and  $\text{TeO}_3$  bipyramidal units causes the  $\Delta\nu = 21.3$  THz resonance to be more intense than the  $\Delta\nu = 20$  THz. A picture of the Lewis  $ns^2$  species here is shown below in Figure 5.3.

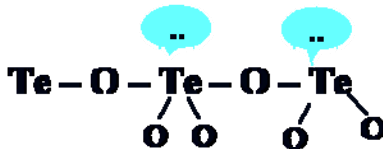


**Figure 5.3.** Schematic of the Lewis  $ns^2$  lone electron pair in  $\text{TeO}_2$  glasses

It can then be speculated that including other Lewis  $ns^2$  lone pair species may further increase the Raman gain near  $\Delta\nu = 21.3$  THz. A series of tellurite glasses with ternary Lewis  $ns^2$  lone pair constituents were fabricated and tested that were of the family  $(100-x-y)\text{TeO}_2 - x\text{TlO}_{0.5} - y\text{PbO}$ . While lead is known to act as a modifier in very small molar quantities, it can serve as an intermediate or partner former in some glass compositions. The addition to the glass in the previous role would allow the average bond strength of the glass to be enhanced, thus “hardening” the material’s laser damage resistance. A systematic study to evaluate this trend in these and other glass systems is necessary to validate these structure-based assumptions.

Nine samples were tested for their Raman gain performance and to verify if an increase in surface optical damage threshold can be measured with varying lead content. In fact, the addition of  $\text{PbO}$  to the glass matrix did increase the damage threshold and

allowed the full Raman gain curve to be obtained for all nine samples tested. Figure 5.4 shows the absorption band edge of the three samples with the least amount of TeO<sub>2</sub> content. Note that the absorption edge now extends into the green end of the spectrum near the 514.5 nm argon ion laser line typically used for spontaneous Raman scattering measurements.

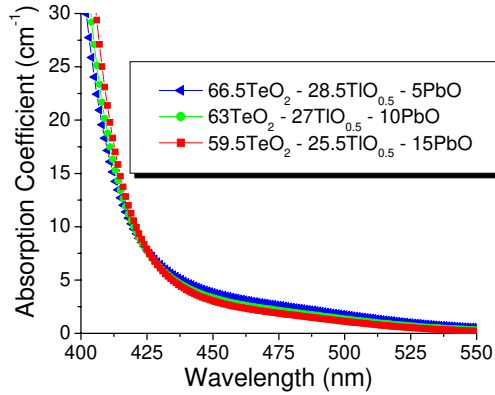
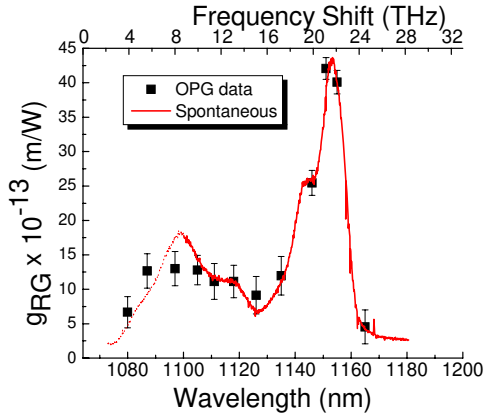


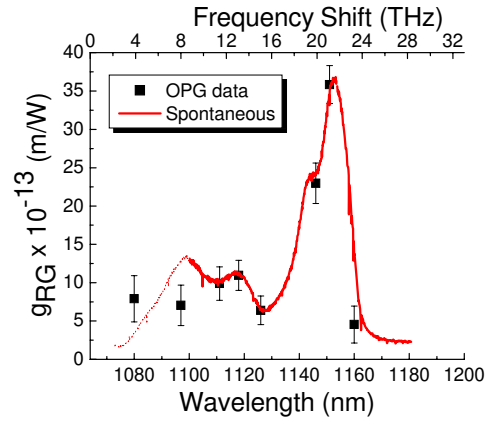
**Figure 5.4.** Absorption coefficient of three ternary tellurite glasses

The absorption band edge moves to longer wavelengths with increased PbO content. At the same time, the residual tail of the absorption curve decreases with increased PbO content in the glass matrix.

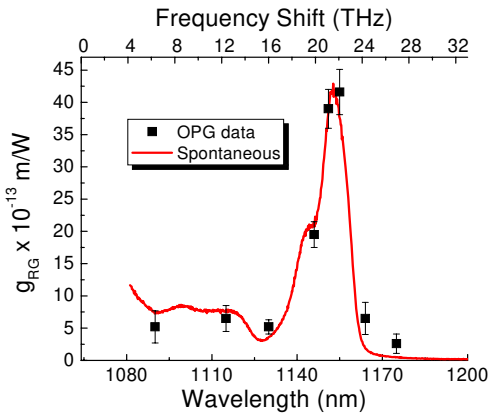
Figures 5.5 (a) – (h) show the Raman gain curves for the ternary tellurite glasses with the spontaneous Raman scattering spectra overlaid for comparison. The spontaneous Raman spectra were obtained at 1064 nm but are *not* the absolute cross-section so they are normalized to the peak in the Raman gain spectra.



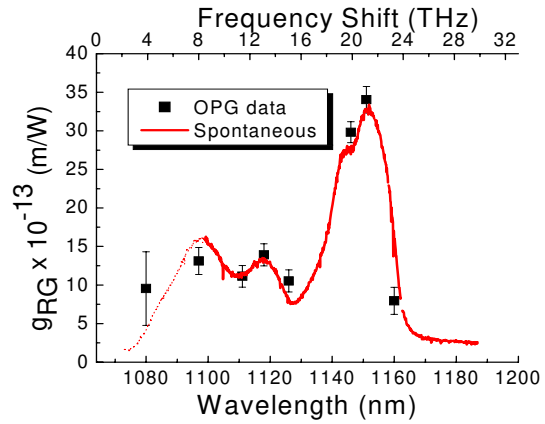
(a)



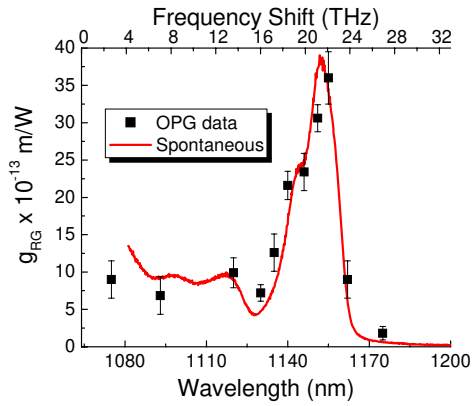
(b)



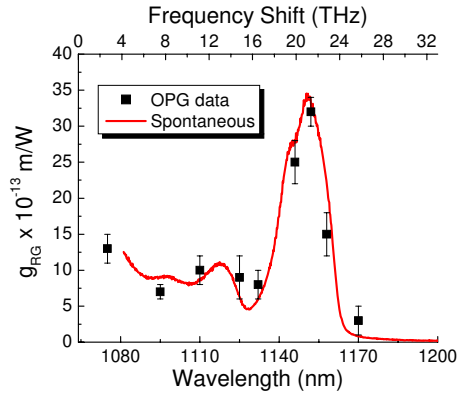
(c)



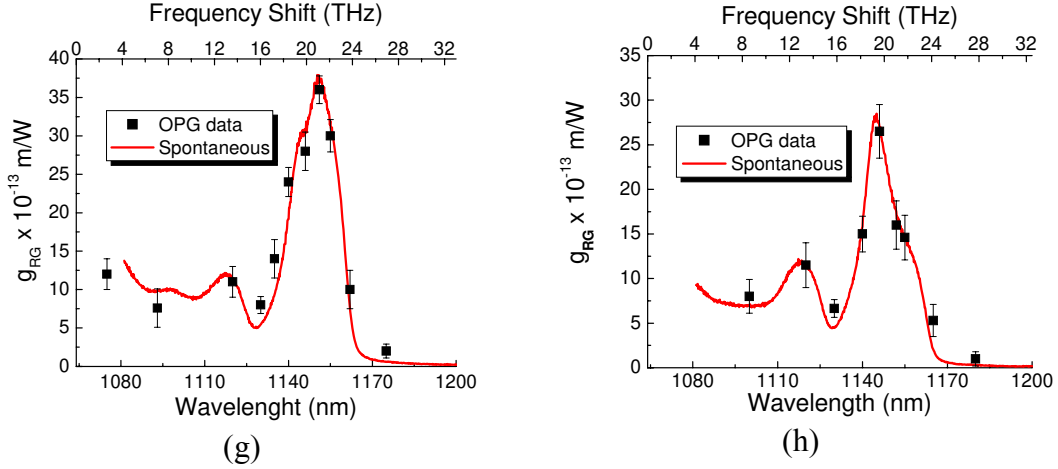
(d)



(e)



(f)



**Figures 5.5 (a) - (h).** Raman gain curves with the spontaneous Raman spectrum overlaid and normalized to the peak of the Raman gain for (a)  $59.5\text{TeO}_2 - 25.5\text{TlO}_{0.5} - 15\text{PbO}$ , (b)  $63\text{TeO}_2 - 27\text{TlO}_{0.5} - 10\text{PbO}$ , (c)  $64\text{TeO}_2 - 16\text{TlO}_{0.5} - 20\text{PbO}$ , (d)  $66.5\text{TeO}_2 - 28.5\text{TlO}_{0.5} - 5\text{PbO}$ , (e)  $68\text{TeO}_2 - 17\text{TlO}_{0.5} - 15\text{PbO}$ , (f)  $70\text{TeO}_2 - 10\text{TlO}_{0.5} - 20\text{PbO}$ , (g)  $72\text{TeO}_2 - 18\text{TlO}_{0.5} - 10\text{PbO}$ , and (h)  $85\text{TeO}_2 - 10\text{TlO}_{0.5} - 5\text{PbO}$

As the amount of  $\text{TeO}_2$  in the glass increases, the peak in the Raman gain spectrum shifts from  $\Delta\nu = 21.3 \text{ THz}$  to  $\Delta\nu = 20 \text{ THz}$ . This is in agreement with the analysis presented in the previous section regarding the evolution of  $\text{TeO}_4$  disphenoids morphing into  $\text{TeO}_{3+1}$  units and further into  $\text{TeO}_3$  units for decreasing amounts of  $\text{TeO}_2$  in tellurite glass. An anomaly in the evolution of this trend occurs for the compositions  $64\text{TeO}_2 - 16\text{TlO}_{0.5} - 20\text{PbO}$ ,  $66.5\text{TeO}_2 - 28.5\text{TlO}_{0.5} - 5\text{PbO}$ ,  $68\text{TeO}_2 - 17\text{TlO}_{0.5} - 15\text{PbO}$ , and  $70\text{TeO}_2 - 10\text{TlO}_{0.5} - 20\text{PbO}$  (Figures 5.5 (c) – (f)). The ratio of the Raman intensities associated with the  $\text{TeO}_4$  units to  $\text{TeO}_{3+1}$  and/or  $\text{TeO}_3$  units decreases for Figure 5.5 (c) ( $64\text{TeO}_2 - 16\text{TlO}_{0.5} - 20\text{PbO}$ ) to Figure 5.5 (d) ( $66.5\text{TeO}_2 - 28.5\text{TlO}_{0.5} - 5\text{PbO}$ ), but it *increases* for Figure 5.5 (d) ( $66.5\text{TeO}_2 - 28.5\text{TlO}_{0.5} - 5\text{PbO}$ ) to Figure 5.5 (e) ( $68\text{TeO}_2 - 17\text{TlO}_{0.5} - 15\text{PbO}$ ) before decreasing again for Figure 5.5 (e) ( $68\text{TeO}_2 - 17\text{TlO}_{0.5} - 15\text{PbO}$ ) to Figure 5.5 (f) ( $70\text{TeO}_2 - 10\text{TlO}_{0.5} - 20\text{PbO}$ ). The transition from Figure 5.5 (g) ( $72\text{TeO}_2 - 18\text{TlO}_{0.5} - 10\text{PbO}$ ) to Figure 5.5 (h) ( $85\text{TeO}_2 - 10\text{TlO}_{0.5} - 5\text{PbO}$ ) clearly shows the transition of the peak in the Raman gain spectrum from the  $\Delta\nu =$

21.3 THz resonance to  $\Delta\nu = 20$  THz resonance. Although the reason for this behavior is unclear at this time, it is clearly rooted in the details of the glass science which need to be addressed by other techniques. Although the  $\text{TeO}_4$  disphenoid has shown to be the most polarizable unit inside of tellurite glass through *ab initio* calculations, the Raman gain curves of glasses in which tellurite is coupled with one or more other Lewis  $ns^2$  lone pair holders demonstrate that the stereochemical coupling between the other Lewis  $ns^2$  lone pair holders and the  $\text{TeO}_{3+1}$  and/or  $\text{TeO}_3$  units provides the peak Raman gain in these glasses [18]. Table 5.2 summarizes the peak Raman gain coefficients near  $\Delta\nu = 21.3$  THz and  $\Delta\nu = 20$  THz found in the ternary Lewis  $ns^2$  lone pair holder tellurite glasses investigated.

**Table 5.2.** Peak Raman gain coefficients near  $\Delta\nu = 21.3$  THz and  $\Delta\nu = 20$  THz and surface optical damage thresholds of ternary tellurite glasses with Lewis  $ns^2$  lone pair holders

	$g_{\text{RG}} \times 10^{-13} \text{ m/W}$ $\Delta\nu = 20 \text{ THz}$	$g_{\text{RG}} \times 10^{-13} \text{ m/W}$ $\Delta\nu = 21.3 \text{ THz}$	Surface optical damage threshold ( $\text{GW/cm}^2$ )
59.5 $\text{TeO}_2$ – 25.5 $\text{TlO}_{0.5}$ – 15 $\text{PbO}$	25±2	42±2	8.3
63 $\text{TeO}_2$ – 27 $\text{TlO}_{0.5}$ – 10 $\text{PbO}$	23±3	38±3	8.5
64 $\text{TeO}_2$ – 16 $\text{TlO}_{0.5}$ – 20 $\text{PbO}$	19±2	43±3	9.2
66.5 $\text{TeO}_2$ – 28.5 $\text{TlO}_{0.5}$ – 5 $\text{PbO}$	30±2	34±2	8.5
68 $\text{TeO}_2$ – 17 $\text{TlO}_{0.5}$ – 15 $\text{PbO}$	23±2	39±4	9.0
70 $\text{TeO}_2$ – 10 $\text{TlO}_{0.5}$ – 20 $\text{PbO}$	25±3	32±2	9.7
72 $\text{TeO}_2$ – 18 $\text{TlO}_{0.5}$ – 10 $\text{PbO}$	28±3	36±2	9.0
76 $\text{TeO}_2$ – 19 $\text{TlO}_{0.5}$ – 5 $\text{PbO}$	25±7	29±6	9.6
85 $\text{TeO}_2$ – 10 $\text{TlO}_{0.5}$ – 5 $\text{PbO}$	28±2	15±2	11.6

The surface optical damage threshold is roughly twice that of the binary tellurium-thallium glasses previously tested. It is not yet known why the addition of  $\text{PbO}$  to the glass matrix increases the surface optical damage threshold over the binary  $\text{TeO}_2$  –  $\text{TlO}_{0.5}$  glasses based on previous analysis of identical compositions. However, it is believed to be related to the role of  $\text{PbO}$  as a network participant in the ternary glasses. While lead is known to act as a modifier in very small molar quantities, it can serve as an

intermediate or partner former in some glass compositions. Its addition to the glass in the previous role would allow the average bond strength of the glass to be enhanced, thus “hardening” the material’s laser damage resistance. A systematic study to evaluate this trend in these and other glass systems is necessary to validate these structure-based assumptions.

### **5.3 Raman Gain Measurements of Tellurite Glasses with Lewis $ns^2$**

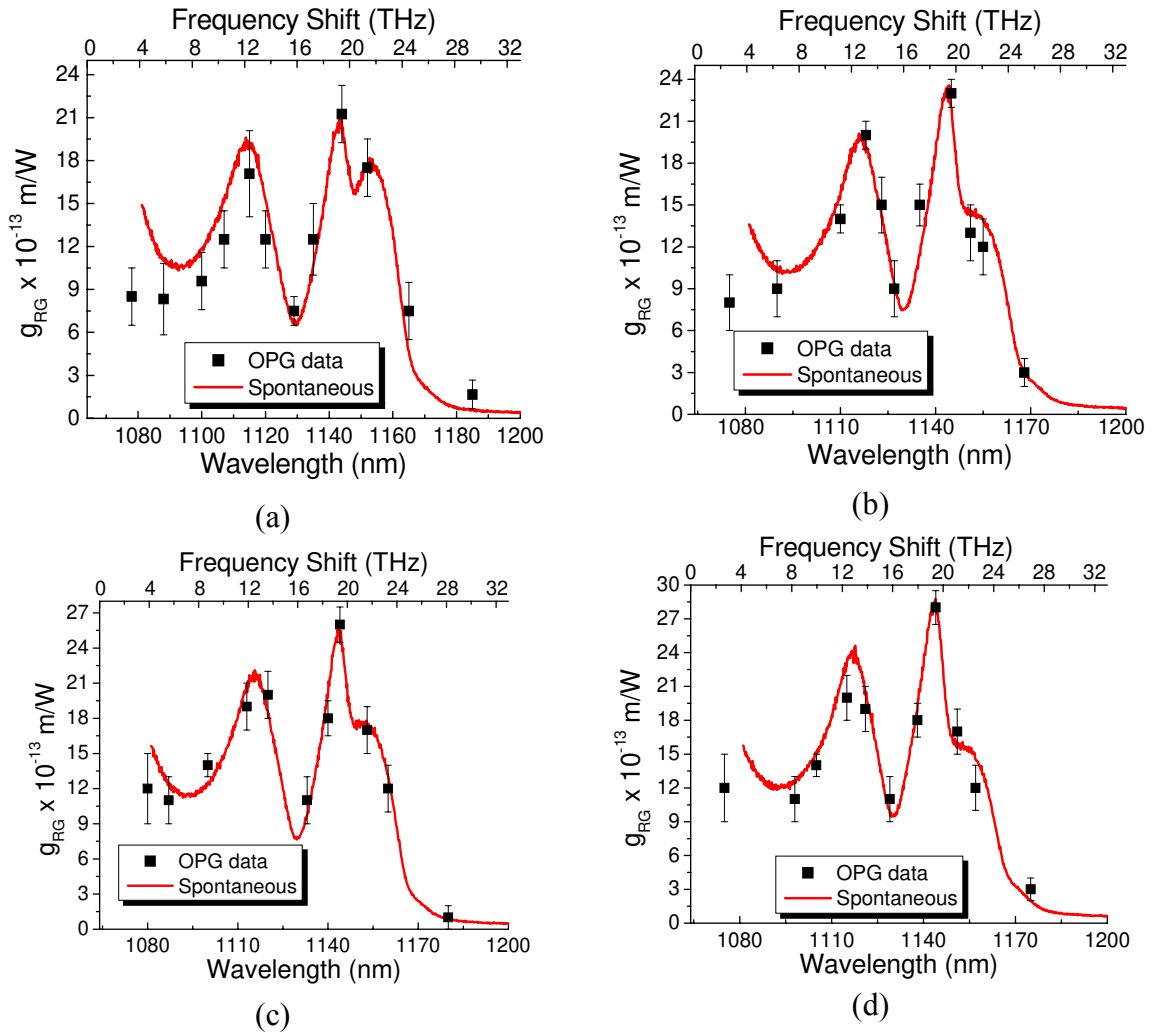
#### ***Lone Pair Electrons and $d^0$ Ions of $Ti^{4+}$ , $Nb^{5+}$ , and $W^{6+}$***

It has been shown in the previous chapter that the addition of  $d^0$  ions such as  $Ti^{4+}$ ,  $Nb^{5+}$ , and  $W^{6+}$  to a glass can significantly enhance the intensity of the Raman gain spectrum due to the high polarizability of the  $d^0$  ions. An investigation into the effect of adding  $d^0$  ions to a tellurite glass with an additional Lewis  $ns^2$  lone pair holder (such as  $Tl^+$ ,  $Pb^{2+}$ , or  $Bi^{3+}$ ) was performed by examining two families of tellurite glass.

The first series of glasses under investigation consisted of the composition  $(100-x-y)TeO_2 - xTiO_2 - yBi_2O_3$ .  $Bi_2O_3$  was added since tellurite glass with  $Bi_2O_3$  has been shown to possess the highest values of  $n_2$  among all tellurite glass [30].  $TiO_2$  was added to the tellurite glass as it is known to help prevent the depolymerization of the  $TeO_4$  units into  $TeO_{3+1}$  and  $TeO_3$  units, *viz.* the  $TeO_4$  disphenoids are joined in the network by  $TiO_4$  units before significant evolution to  $TeO_{3+1}$  and/or  $TeO_3$  units [51]. The resonance at  $\Delta\nu = 13.5$  THz is caused by the *network* of  $TeO_4$  disphenoids [48]. A network of  $T\beta O_4$  units ( $\beta = Te$  or  $Ti$ ) may be expected to enhance the  $\Delta\nu = 20$  THz and  $\Delta\nu = 13.5$  THz resonances for large amounts of  $TeO_2$  and to slow down the reduction in intensity of the  $\Delta\nu = 20$  THz and  $\Delta\nu = 13.5$  THz resonances for decreasing amounts of  $TeO_2$ .



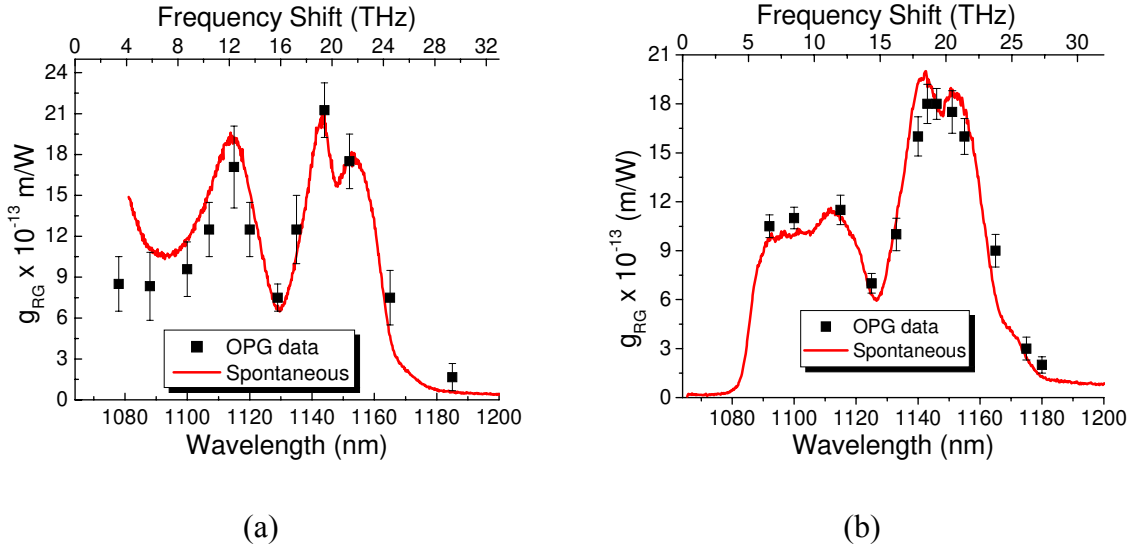
The Raman gain measurements for four of the  $\text{TeO}_2 - \text{TiO}_2 - \text{Bi}_2\text{O}_3$  glasses are shown in Figures 5.6 (a) – (d). They are displayed in the order of increasing  $\text{TeO}_2$  content from Figure 5.6 (a) through Figure 5.6 (d).



**Figures 5.6 (a) - (d).** Raman gain curves and normalized spontaneous Raman spectra for (a)  $75\text{TeO}_2 - 10\text{TiO}_2 - 15\text{Bi}_2\text{O}_3$ , (b)  $80\text{TeO}_2 - 12.5\text{TiO}_2 - 7.5\text{Bi}_2\text{O}_3$ , (c)  $80\text{TeO}_2 - 10\text{TiO}_2 - 10\text{Bi}_2\text{O}_3$  and (d)  $85\text{TeO}_2 - 10\text{TiO}_2 - 5\text{Bi}_2\text{O}_3$

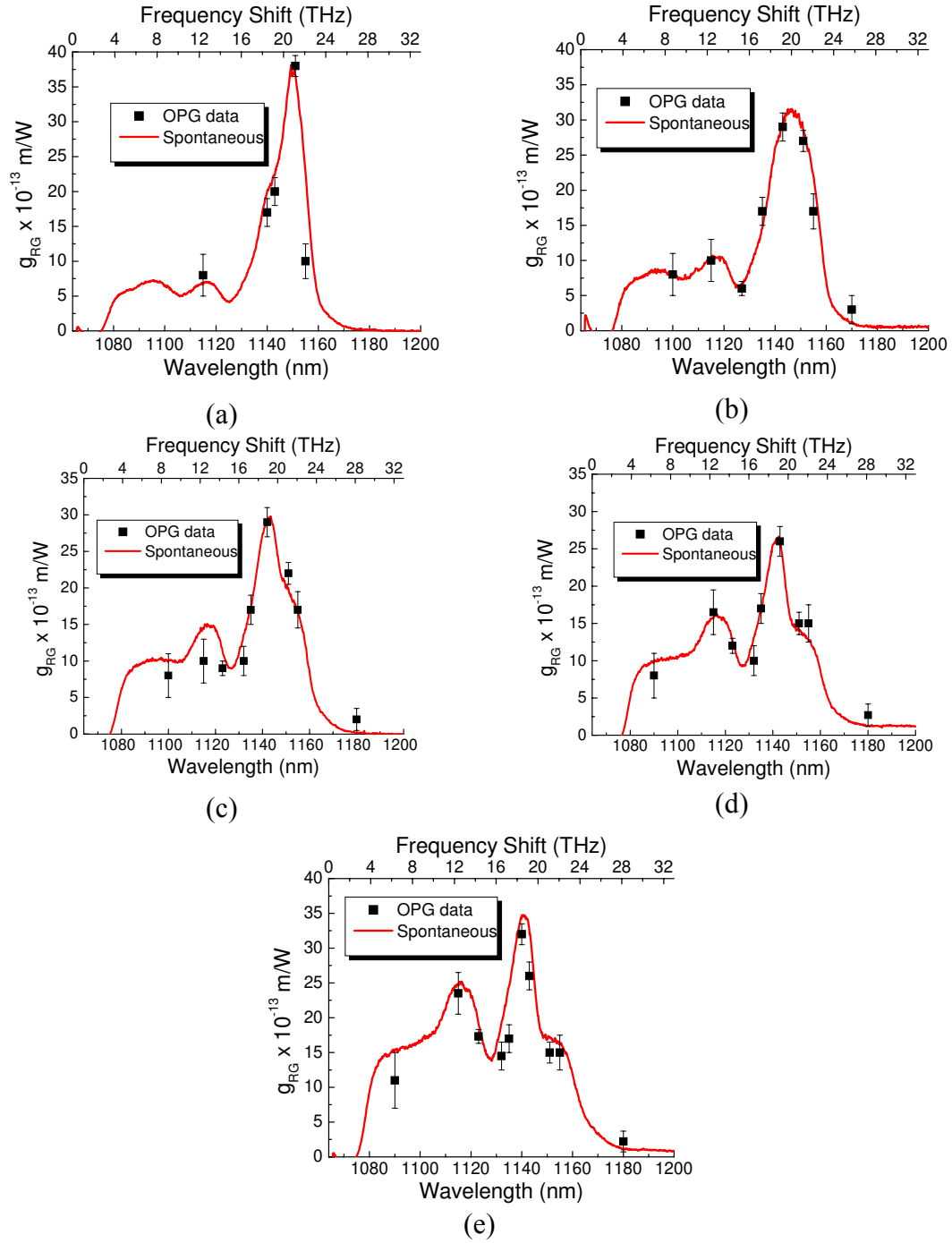
A comparison of the intensities and resonances near  $\Delta\nu = 20 \text{ THz}$  and  $\Delta\nu = 13.5 \text{ THz}$  for the glass in Figure 5.6 (a) to a previously discussed tellurite glass with the

composition  $75\text{TeO}_2 - 12\text{ZnO} - 5\text{PbO} - 3\text{PbF}_2 - 5\text{Nb}_2\text{O}_5$  yields insight into how the *network* of the glass is affected by the compositional differences. This comparison is shown in Figures 5.7 (a) & (b).



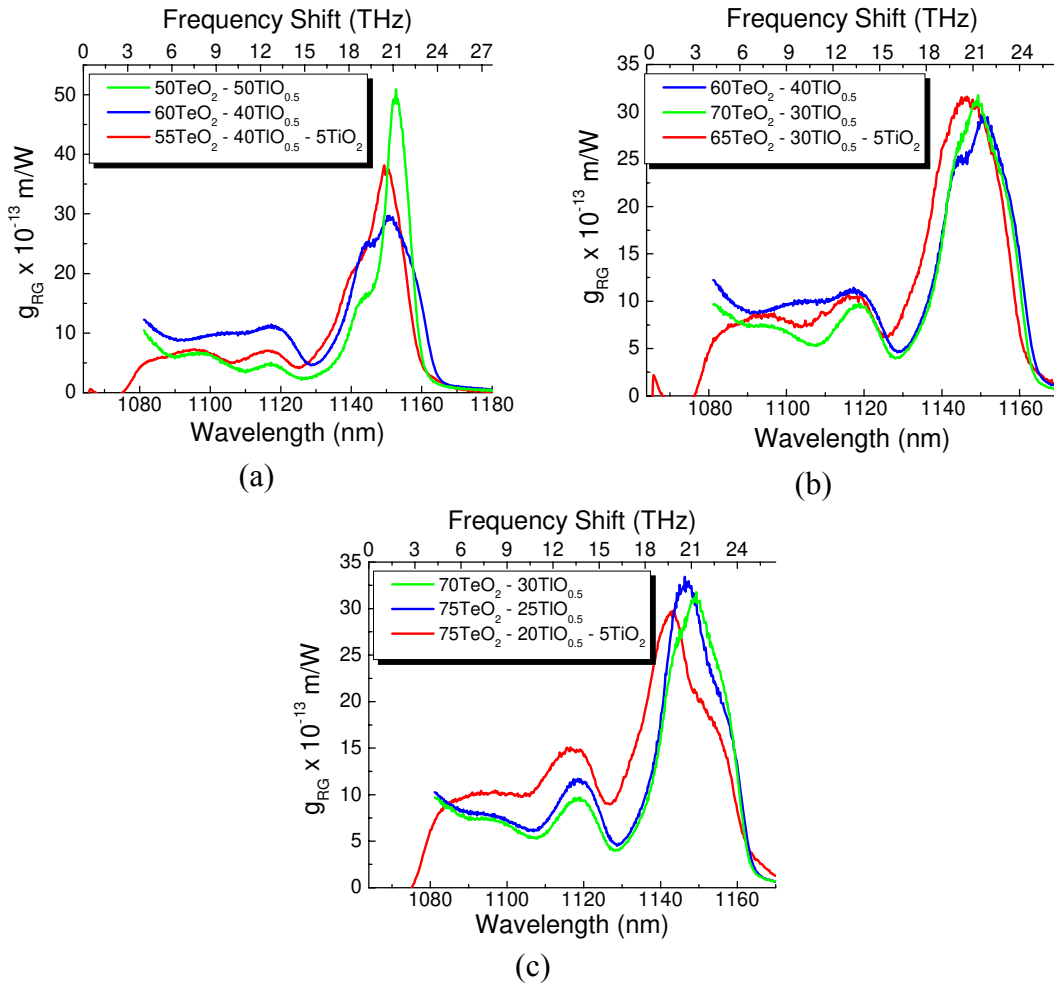
**Figures 5.7 (a) & (b).** Raman gain curves of (a)  $75\text{TeO}_2 - 10\text{TiO}_2 - 15\text{Bi}_2\text{O}_3$  and (b)  $75\text{TeO}_2 - 12\text{ZnO} - 5\text{PbO} - 3\text{PbF}_2 - 5\text{Nb}_2\text{O}_5$ . The network resonance near  $\Delta\nu = 13.5$  THz is enhanced by the presence of  $\text{TiO}_2$  for similar amounts of  $\text{TeO}_2$

The  $(100-x-y)\text{TeO}_2 - x\text{TiO}_2 - y\text{TlO}_{0.5}$  family was also tested. Small amounts of  $\text{TiO}_2$  were added to the  $\text{TeO}_2 - \text{TlO}_{0.5}$  family to investigate how the spectral shape and intensity differed from the binary  $\text{TeO}_2 - \text{TlO}_{0.5}$  oxide glasses. Five glasses were tested for their Raman gain performance and the results are shown in Figures 5.8 (a) – (e).



**Figures 5.8 (a) – (e).** Raman gain curves with the spontaneous Raman spectrum obtained at 633 nm overlaid and normalized to the peak in the Raman gain curve for (a)  $55\text{TeO}_2 - 40\text{TlO}_{0.5} - 5\text{TiO}_2$ , (b)  $65\text{TeO}_2 - 30\text{TlO}_{0.5} - 5\text{TiO}_2$ , (c)  $75\text{TeO}_2 - 20\text{TlO}_{0.5} - 5\text{TiO}_2$ , (d)  $80\text{TeO}_2 - 10\text{TlO}_{0.5} - 10\text{TiO}_2$ , and (e)  $80\text{TeO}_2 - 5\text{TlO}_{0.5} - 15\text{TiO}_2$

A way to verify how the Raman gain spectrum differs from the binary  $\text{TeO}_2 - \text{TlO}_{0.5}$  by including  $\text{TiO}_2$  is to overlay the plots for similar compositions as shown in Figures 5.9 (a) – (c).



**Figures 5.9 (a) – (c).** Spontaneous Raman cross-section of binary glasses obtained at 1064 nm and spontaneous Raman data normalized to the peak in the Raman gain spectrum obtained at 1064 nm using direct NLO measurements

As seen in the previous section, the addition of  $\text{TiO}_2$  to the binary glass results in decreased Raman gain near  $\Delta\nu = 21.3 \text{ THz}$ . This happens because  $\text{TiO}_2$  participates in the glass network and effectively “replaces” the  $\text{TeO}_4$  units with  $\text{TiO}_4$  units.

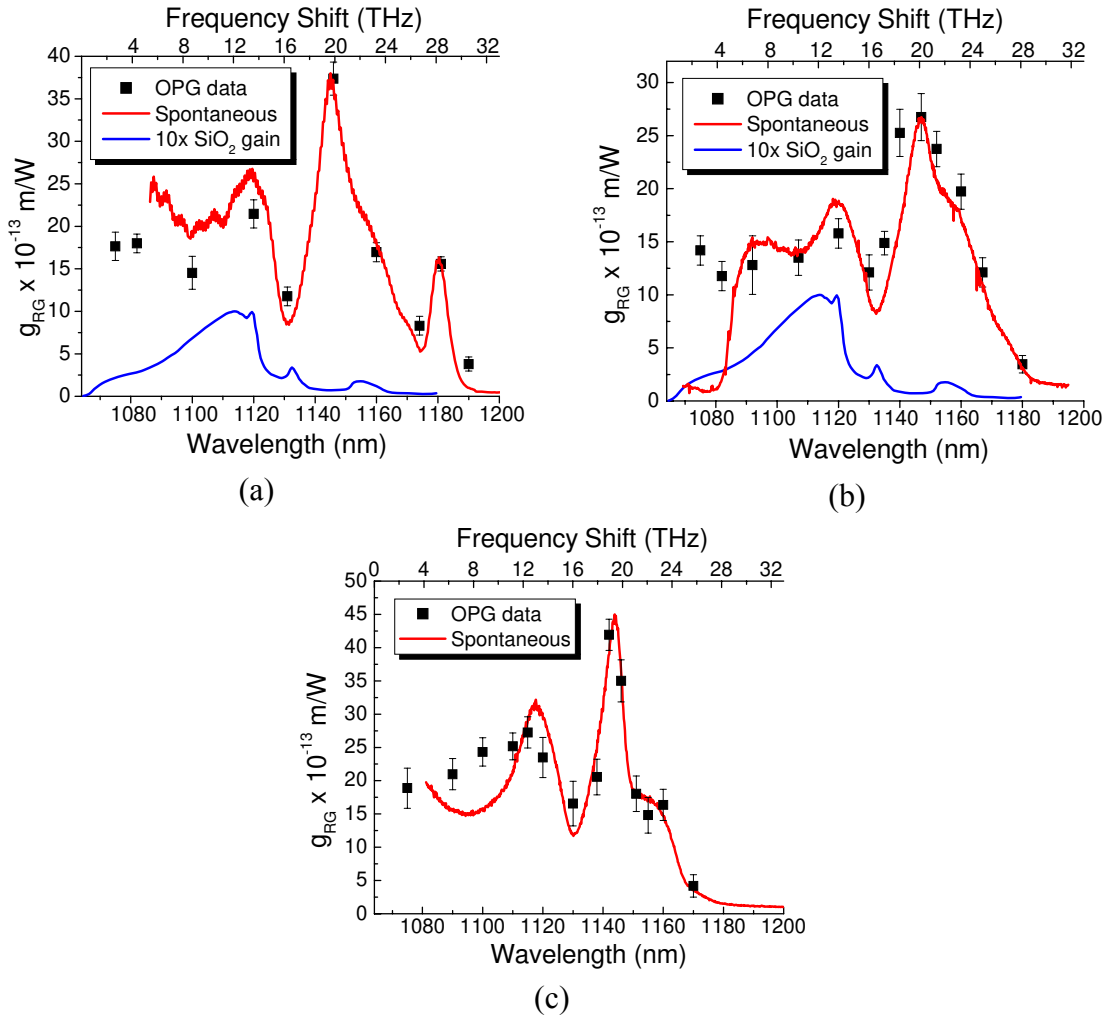
Confirmation of this is found in the increased Raman gain near  $\Delta\nu = 13.5$  THz and  $\Delta\nu = 20$  THz and decreased Raman gain near  $\Delta\nu = 21.3$  THz. Table 5.3 lists the Raman gain values for the two main resonances located near  $\Delta\nu = 20$  THz and  $\Delta\nu = 21.3$  THz along with the surface optical damage threshold for the  $\text{TeO}_2 - \text{TlO}_{0.5} - \text{Bi}_2\text{O}_3$  and  $\text{TeO}_2 - \text{TlO}_{0.5} - \text{TiO}_2$  families.

**Table 5.3.** Main peak Raman gain coefficients and surface optical damage thresholds for ternary Lewis ns<sup>2</sup> and d<sup>0</sup> ion tellurite glasses

	$g_{\text{RG}} \times 10^{-13} \text{ m/W}$ $\Delta\nu = 20 \text{ THz}$	$g_{\text{RG}} \times 10^{-13} \text{ m/W}$ $\Delta\nu = 21.3 \text{ THz}$	Surface optical damage threshold ( $\text{GW/cm}^2$ )
75TeO <sub>2</sub> – 10TiO <sub>2</sub> – 15Bi <sub>2</sub> O <sub>3</sub>	21±2	18±2	4.2
80TeO <sub>2</sub> – 12.5TiO <sub>2</sub> – 7.5Bi <sub>2</sub> O <sub>3</sub>	23±1	13±2	5.6
80TeO <sub>2</sub> – 10TiO <sub>2</sub> – 10Bi <sub>2</sub> O <sub>3</sub>	26±1	17±2	5.1
85TeO <sub>2</sub> – 10TiO <sub>2</sub> – 5Bi <sub>2</sub> O <sub>3</sub>	28±1	15±1.5	6.7
55TeO <sub>2</sub> – 40TlO <sub>0.5</sub> – 5TiO <sub>2</sub>	17±2	38±2	7.4
65TeO <sub>2</sub> – 30TlO <sub>0.5</sub> – 5TiO <sub>2</sub>	29±2	27±2	7.6
75TeO <sub>2</sub> – 20TlO <sub>0.5</sub> – 5TiO <sub>2</sub>	29±2	17±3	8.2
80TeO <sub>2</sub> – 10TlO <sub>0.5</sub> – 10TiO <sub>2</sub>	26±2	14±2	9.7
80TeO <sub>2</sub> – 5TlO <sub>0.5</sub> – 15TiO <sub>2</sub>	33±2	14±2.5	11.3

#### 5.4 Raman Gain Measurements of Tellurite Glass with d<sup>0</sup> Ions

Raman gain measurements were made on three tellurite glasses which incorporated only d<sup>0</sup> ions. The results of these measurements are depicted in Figures 5.9 (a) – (c). Chronologically, Figures 5.9 (a) & (b) were the first reported tellurite Raman gain spectrum in the literature from our group [14].



**Figures 5.10 (a) – (c).** Raman gain spectrum with spontaneous Raman scattering spectrum overlaid and normalized to the peak in the Raman gain spectrum for (a) 85TeO<sub>2</sub> – 15WO<sub>3</sub>, (b) 85TeO<sub>2</sub> – 10Nb<sub>2</sub>O<sub>5</sub> – 5MgO, and (c) 90TeO<sub>2</sub> – 10TiO<sub>2</sub>. Raman gain spectrum of fused silica is also overlaid and multiplied by a factor of 10

Figures 5.10 (a) & (b) were initially reported without accounting for the depolarization ratio which typically increases the measured polarized Raman gain coefficients by 20% - 30% in these high Raman gain glasses [48]. That is, the gain experienced in the “orthogonal polarization” to the pump beam can be significant. Since this signal transmitted through the monochromator and the sample was used to evaluate the incident pump energy on a shot-to-shot basis, the value of the input signal into the sample was overestimated. The ratio of the “orthogonal” to the “parallel” gain was

estimated from the depolarization ratio of the spontaneous Raman scattered signal. This data was corrected for this effect in Figure 5.10.

In Figure 5.10 (a), the additional Raman resonance near  $\Delta\nu = 28$  THz is caused by the presence of  $\text{WO}_3$  in the sample, and the small shoulder near  $\Delta\nu = 24$  THz in Figure 5.10 (b) is caused by the addition of  $\text{Nb}_2\text{O}_5$  in the tellurite glass [14]. The composition in Figure 5.10 (b) contains a small amount of  $\text{MgO}$  in order to stabilize the glass network and results in a lower Raman gain curve than the other two compositions. Figure 5.10 (c) ( $90\text{TeO}_2 - 10\text{TiO}_2$ ) provides the highest peak Raman gain for tellurites with  $d^0$  ions approaching  $(45 \pm 3) \times 10^{-13}$  m/W near the  $\Delta\nu = 20$  THz resonance of the  $\text{TeO}_4$  disphenoids. This peak Raman gain is also the highest Raman gain found for the  $\Delta\nu = 20$  THz resonance.

## 5.5 “The Controversy”

Immediately following the CREOL report in the literature of two of the new tellurite samples just discussed in Section 5.4, namely W ( $85\text{TeO}_2 - 15\text{WO}_3$ ) and Nb ( $85\text{TeO}_2 - 10\text{Nb}_2\text{O}_5 - 5\text{MgO}$ ), and the unique way in which the material Raman gain coefficient was obtained from bulk materials, an Italian group published results on similar tellurite compositions containing  $d^0$  ions and claimed a factor of two higher Raman gain coefficients than those reported by our group [15]. The Italian group performed spontaneous Raman scattering measurements and used 532 nm and 633 nm pump lasers. They reported that they obtained similar Raman scattered intensities from both sources and published their results using the Raman data from the 532 nm pump. The results were normalized to the Raman scattered intensity of fused silica at 532 nm.

The rationale they provided that their data was correct referred the reader to a paper published by a Japanese group at NTT who fabricated a tellurite fiber and claimed a Raman gain coefficient approximately 30 times higher than fused silica using 1400 nm pumping [52]. Although the exact composition of the Japanese fiber was unknown (patented), the Italian group fabricated a glass with a very similar Raman spectrum and obtained a Raman gain coefficient from this material that was 32 times higher than fused silica using 532 nm pumping. (It should be noted that the Japanese group later revised their published Raman gain coefficient as 16 times higher than fused silica [25].) The Italian group claimed the composition  $90\text{TeO}_2 - 10\text{WO}_3$  provided a peak Raman gain coefficient greater than 60 times higher than that of fused silica using 532 nm pumping and compared this to our initial stated claim of 30 times higher than fused silica for  $85\text{TeO}_2 - 15\text{WO}_3$ . Armed with their data, the Italian group called into question the validity of our data due to our experimental technique, i.e. the data was wrong.

Additionally, a Russian group and a Japanese team from Toyota Technical Institute published Raman gain data on tellurite compositions using spontaneous Raman scattering with visible lasers as well [20,21]. The Russians used a 514.5 nm source and reported Raman gain coefficients approaching 100 times greater than fused silica for compositions with heavy amounts of  $\text{d}^0$  ions. The peak in the Raman gain spectrum occurred near the  $\text{WO}_3$  resonance at  $\Delta\nu = 28$  THz augmented by the presence of  $\text{MoO}_3$ . They also remarked that their data differed from our published results by roughly a factor of two. The group from Toyota published data on tellurite compositions using a 488 nm pump source. They fabricated and tested the composition  $85\text{TeO}_2 - 15\text{WO}_3$  and obtained a Raman gain coefficient approximately 75 times higher than fused silica near the  $\Delta\nu =$



20 THz resonance of the TeO<sub>4</sub> disphenoids. The Toyota group also reported their results differed from our results by roughly a factor of two and remarked that the discrepancy could be attributed to different processing techniques, yet still claimed their samples were superior due to the largest reported Raman gains for similar compositions.

This controversy was resolved when spontaneous Raman spectra taken at different pump wavelengths for W and Nb were reported by Rivero et. al [22]. From the discussion in Chapter 2 on frequency dispersion of spontaneous Raman scattering, the ratio of the Raman gain for a glass at two different frequencies  $\omega_1$  and  $\omega_2$ , is given in terms of the Raman scattering intensities by

$$\frac{g_{RG\beta}^{r,k}(\omega_2 - \Omega_{\beta}^r)}{g_{RG\beta}^{r,k}(\omega_1 - \Omega_{\beta}^r)} = \frac{(\omega_1 - \Omega_{\beta}^r)^3}{(\omega_2 - \Omega_{\beta}^r)^3} \frac{n(\omega_2 - \Omega_{\beta}^r)n(\omega_1)}{n(\omega_1 - \Omega_{\beta}^r)n(\omega_2)} \frac{[1 - R(\omega_1 - \Omega_{\beta}^r)][1 - R(\omega_1)]}{[1 - R(\omega_2 - \Omega_{\beta}^r)][1 - R(\omega_2)]} \quad (5.1)$$

$$\times \frac{I_{\beta}^{k,r}(\omega_2 - \Omega_{\beta}^r)}{I_{inc}(\omega_2)} \frac{I_{inc}(\omega_1)}{I_{\beta}^{k,r}(\omega_1 - \Omega_{\beta}^r)}$$

Stolen, in his seminal works on Raman gain deduced from spontaneous Raman scattering, has found that the ratio for the Raman susceptibility for fused silica at different wavelengths is given accurately by Equation 5.1 over the wavelength range 526 – 1064 nm (with a maximum possible frequency dispersion correction of 5% for this wavelength range) [9]. This was expected because the band edge for silica occurs below 200 nm, i.e. at about 165 nm, well-removed from 458 nm (the lowest experimental wavelength used to date in spontaneous Raman scattering). Therefore normalizing the Raman data for the tellurite glasses to that of fused silica reveals the dispersion properties of the Raman susceptibility of the tellurite glasses. Furthermore, by measuring the Raman spectra of a test glass under the same experimental conditions as for fused silica at a laser

wavelength for which the peak Raman gain for fused silica is known, the peak Raman gain of the test glass at that frequency for a Raman active mode can be deduced, i.e.

$$\frac{g_{RG\beta}^{r,k}(\omega_1 - \Omega_{\beta}^r)}{g_{RG\beta'}^{r',k'}(\omega_1 - \Omega_{\beta'}^{r'})} = \tag{5.2}$$

$$\frac{(\omega_1 - \Omega_{\beta'}^{r'})^3 n(\omega_1 - \Omega_{\beta'}^{r'})n'(\omega_1) [1 - R'(\omega_1 - \Omega_{\beta'}^{r'})][1 - R'(\omega_1)] I_{\beta}^{k,r}(\omega_1 - \Omega_{\beta}^r)}{(\omega_1 - \Omega_{\beta}^r)^3 n'(\omega_1 - \Omega_{\beta}^r)n(\omega_1) [1 - R(\omega_1 - \Omega_{\beta}^r)][1 - R(\omega_1)] I_{inc}(\omega_1) I_{\beta'}^{r',k'}(\omega_1 - \Omega_{\beta'}^{r'})}$$

where the prime parameters belong to fused silica. Explicitly,  $\Omega_{\beta'}^{r'}$  at 440  $\text{cm}^{-1}$  ( $\Delta\nu = 13.2$  THz) represents the peak in the Raman frequency shift in fused silica, and  $\Omega_{\beta}^r$  is the Raman active mode of either the 665  $\text{cm}^{-1}$  ( $\Delta\nu = 20$  THz) or 920  $\text{cm}^{-1}$  ( $\Delta\nu = 27.6$  THz) vibration in the tellurite glasses.

Once this value is found for the test glass, the “almost” frequency independence of the fused silica Raman susceptibility allows the frequency dependence of the Raman susceptibility of the test glass to be evaluated by taking the ratio of the test glass Raman intensity spectrum to that of fused silica at the new frequency. By normalizing to fused silica, a frequency-independent Raman susceptibility for the glass with respect to fused silica (for the test glass) would be expected to yield a curve with zero slope when it is plotted as a function of pump wavelength if there is no resonant enhancement in the test glass.

Rivero et. al. found that this was not the case according to Figure 5.11. A large decrease in the relative intensity of the Raman scattered signal with increasing excitation wavelength between 458 and 752 nm is clear when ratioed to fused silica. Note that since all the spectra have been normalized to fused silica, the  $1/\lambda^4$ -wavelength dependence

cancels out. This result clearly illustrates a strong dispersion dependence of the Raman susceptibility tensor.

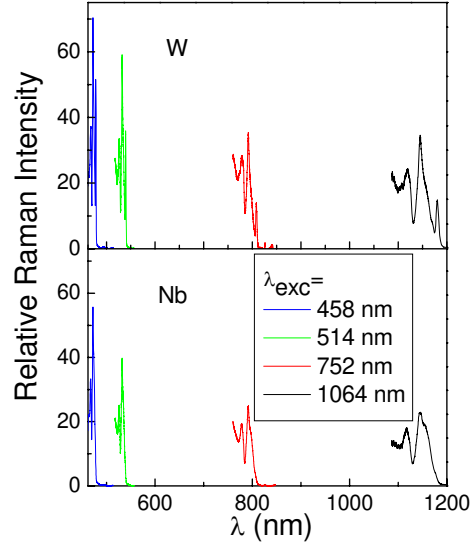


**Figure 5.11.** VV Polarized Experimental Spontaneous Raman Spectrum of samples W ( $85\text{TeO}_2 - 15\text{WO}_3$ ) and Nb ( $85\text{TeO}_2 - 10\text{Nb}_2\text{O}_5 - 5\text{MgO}$ ), normalized to  $\text{SiO}_2$

It is useful to examine the origin of the Raman peaks observed in the two glasses. Figure 5.12 shows the VV polarized spontaneous Raman spectra of the two different glasses at 514 nm. The main peaks, located at around  $450$ ,  $665$ , and  $920\text{ cm}^{-1}$  ( $\Delta\nu = 13.5$  THz, 20 THz, and 27.6 THz), are attributed to the Te-O-Te chain unit symmetric stretching mode, the  $\text{TeO}_4$  bi-pyramidal units, and the isolated W-O short bond vibrations respectively. The shoulders at  $750$  and  $880\text{ cm}^{-1}$  ( $\Delta\nu = 22.5$  THz and 26.4 THz) have been assigned to the  $\text{TeO}_{3+1}$  and/or  $\text{TeO}_3$  trigonal pyramids vibrational units, and the Nb-O vibrations, respectively.

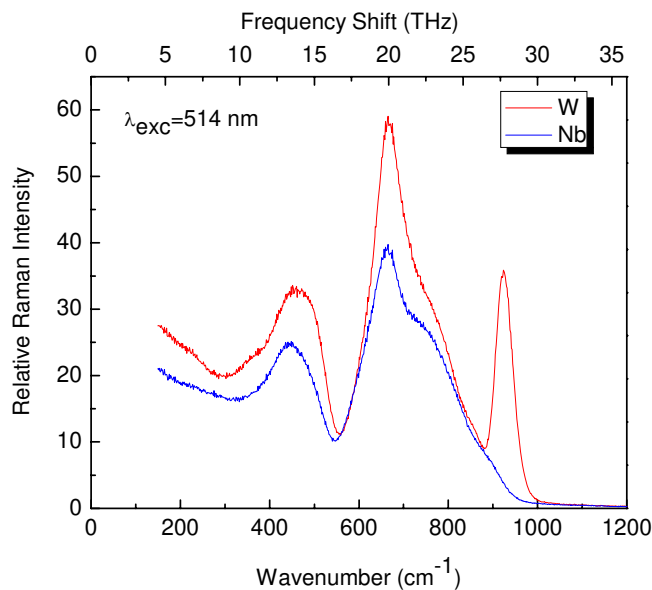


**Figure 5.12.** VV Polarized Spontaneous Raman Spectrum of samples W and Nb, normalized to SiO<sub>2</sub>. Excitation wavelength 514 nm

The Raman gain spectra were obtained from the spontaneous Raman cross-section measurements at different wavelengths. As previously discussed, the Raman gain spectrum parallels the spontaneous Raman cross-section, after correction for the Bose-Einstein correction factor, and the Raman gain coefficient can be obtained using Equation 5.2 once a measured value at a specific wavelength is known. The value of the Raman gain of  $g_{RG} = 1.5 \pm 0.15 \times 10^{-13}$  m/W (for a frequency shift of  $330 \text{ cm}^{-1}$  ( $\Delta\nu = 9.9 \text{ THz}$ )) as measured by Stolen et. al. with 526 nm pumping was used to fix the value of  $g_{RG}$  at 514 nm [23]. Figure 5.12 illustrates the Raman gain coefficient obtained for the strongest Raman resonance in these glasses at  $665 \text{ cm}^{-1}$  ( $\Delta\nu = 20 \text{ THz}$ ), attributed to the TeO<sub>4</sub> bi-pyramidal units, and the  $920 \text{ cm}^{-1}$  vibration attributed to W-O short bond, as discussed above. Also shown in Figure 5.12 is the Raman gain obtained by using a crude

approximation to the wavelength dispersion in the Raman susceptibility

$$\text{as } \left( n^2(\omega_1 - \Omega_{\beta}^r) - 1 \right)^2.$$

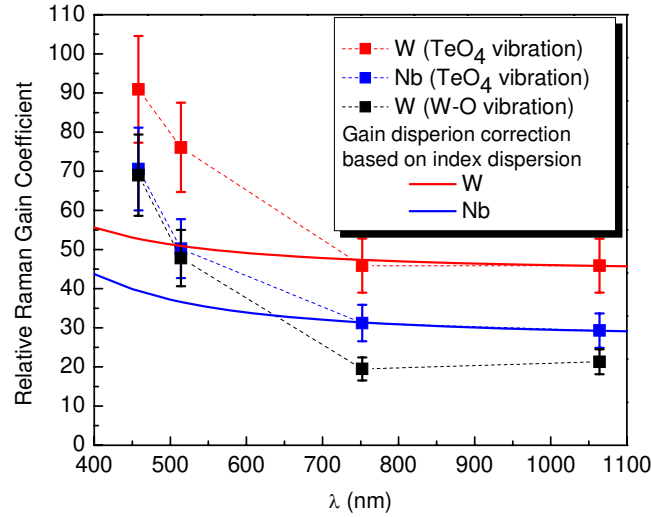


**Figure 5.13.** Estimated multi-wavelength Raman gain coefficient at the peak Raman vibration ( $\text{TeO}_4$  units at  $665 \text{ cm}^{-1}$  ( $\Delta\nu = 20 \text{ THz}$ )), and W-O vibration (at  $920 \text{ cm}^{-1}$  ( $\Delta\nu = 27.6 \text{ THz}$ )) respectively, normalized to  $\text{SiO}_2$ . The dash line is used as a guide to the eye. The solid lines represent the  $(n^2(\lambda) - 1)^2$  approximation to the dispersion which is clearly inadequate when approaching the electronic band edge

It is clear from Figure 5.13 that there is a factor of two discrepancy between the cross-section measurements conducted in the blue-green visible wavelengths, as compared to the cross-section data obtained in the NIR region. There is a resonance enhancement of the Raman susceptibility because the spontaneous, short wavelength Raman measurements were conducted near the absorption edge of the material shown in Figure 5.14. Hence, this result indicates that when the laser wavelength is close to the electronic dipole transition coupled to this particular vibrational mode, resonance enhancement occurs. Furthermore, in these cases, the crude approximation for the wavelength dependence of the Raman susceptibility strongly underestimates the measured wavelength dependence. Note that for wavelengths longer than 752 nm, the

relative gain coefficient is essentially independent of wavelength to within the experimental error.

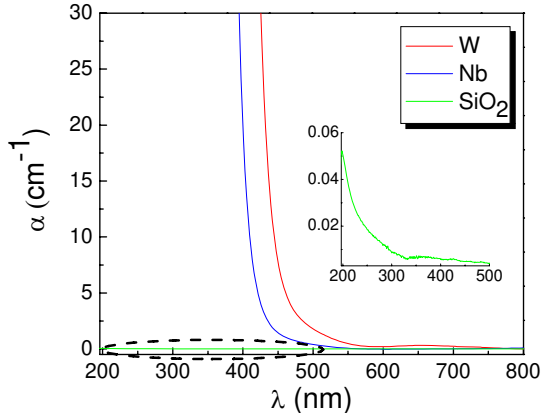


**Figure 5.14.** UV-Vis-NIR absorption spectra of samples W, Nb, and SiO<sub>2</sub>. Notice that 195 nm is the lowest wavelength resolution of the Cary500 Spectrophotometer

The direct Raman gain measurements with 1064 nm pumping on these samples was presented in Section 5.4 in the form of Figures 5.10 (a) & (b). Table 5.4 shows the values of the directly measured Raman gain coefficient of both bulk samples at the 665 cm<sup>-1</sup> ( $\Delta\nu = 20$  THz) Raman resonance, along with the estimated values obtained from the relative cross-section Raman scattering measurements performed with a 1064 nm laser. The agreement is excellent and shows that the controversy is clearly resolved and the direct NLO measurements reported here are vindicated.

**Table 5.4.** Calculated and experimentally measured material Raman gain coefficient with 1064 nm pumping, at the peak Raman resonance at 665 cm<sup>-1</sup> ( $\Delta\nu = 20$  THz)

Sample Code	Calculated Peak Raman Gain Coefficient at 1064 nm (from Spontaneous Raman cross-section)	Peak Raman gain Coefficient at 1064 nm from NLO Experiments
W	$40 \times 10^{-13}$ m/W $\pm$ 15%	$38 \times 10^{-13}$ m/W $\pm$ 10%
Nb	$26 \times 10^{-13}$ m/W $\pm$ 15%	$26 \times 10^{-13}$ m/W $\pm$ 10%

Further evidence for the role played by a close proximity of the Raman scattering excitation laser frequency to the frequency associated with the electronic transitions which couple to the vibrations was obtained by studying the *shape* of the Raman spectrum at *different wavelengths*. This can be demonstrated by identifying Raman peaks for which the Raman-relevant electronic transitions are well-separated in frequency, but still close to the laser frequency. Lines has estimated the effective Sellmeier gap value for single-crystals transition metal (TM) oxides with empty d-bands and TeO<sub>2</sub>, and found that the electronic transitions for the species WO<sub>3</sub>, Nb<sub>2</sub>O<sub>5</sub> and TeO<sub>2</sub> occur at ~ 4.5, 6.8 and 6.3 eV respectively, corresponding to vacuum wavelengths of 276, 183, and 197 nm [27]. While the differences in the local environment between single crystals and a multi-component glass would be expected to affect primarily the shape and spectral width of the electronic transitions, it is reasonable to assume that the actual peak transition wavelengths would only be affected weakly. We use these values for  $\lambda_{k,r}$  of the dominant transitions responsible for the Raman susceptibility. The dominant vibrational Raman peaks associated with these species occur at 920 cm<sup>-1</sup>, 880 cm<sup>-1</sup>, and 665 cm<sup>-1</sup> ( $\Delta\nu = 27.6$  THz, 26.4 THz, and 20 THz) respectively. The Raman peaks at 920 cm<sup>-1</sup> and 665 cm<sup>-1</sup> ( $\Delta\nu = 27.6$  THz and 20 THz) are strong in the 85TeO<sub>2</sub> – 15WO<sub>3</sub> sample and the difference in the wavelengths associated with the electronic transitions is large, 79 nm versus 14 nm for the 85TeO<sub>2</sub> – 10 Nb<sub>2</sub>O<sub>5</sub> – 5MgO sample respectively. Hence the W sample is the best choice for this comparison.

Although both Raman peaks of W are probably resonantly enhanced in the visible, the relative location of the absorption peaks implies that the enhancement should be larger for the 920 cm<sup>-1</sup> ( $\Delta\nu = 27.6$  THz) Raman line, as is also evident from Figure

5.13. In fact, a large resonance enhancement of the  $920\text{ cm}^{-1}$  ( $\Delta\nu = 27.6\text{ THz}$ ) Raman vibration was observed for wavelengths in the visible, after normalizing to the peak Raman gain coefficient at  $665\text{ cm}^{-1}$  ( $\Delta\nu = 20\text{ THz}$ ). This is shown in Figure 5.15, along with the Raman gain spectrum obtained by the direct gain measurement technique with  $1064\text{ nm}$  pumping. This change in the spectrum fully supports the hypothesis that electronic enhancement occurs in these glasses because the Raman spectrum was measured with laser wavelengths near the absorption edge of the glasses. Furthermore, the spectra obtained from the spontaneous Raman and direct measurement experiments with  $1064\text{ nm}$  pumping are in better agreement than the spontaneous Raman spectrum used in the Optics Letter publication since the spontaneous Raman spectrum used in the Optics Letter was obtained at  $514\text{ nm}$  pumping (the green curve in Figure 5.15).

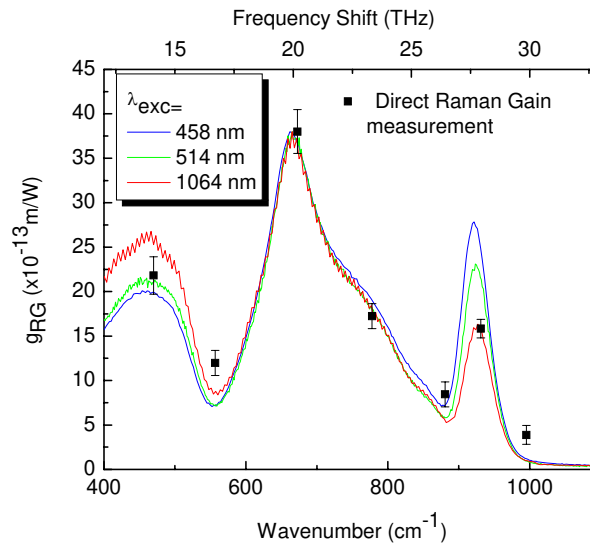


**Figure 5.15.** Spontaneous Raman spectra of  $85\text{TeO}_2 - 15\text{WO}_3$  obtained at different wavelengths, normalized to the peak Raman gain value at  $665\text{ cm}^{-1}$  ( $\Delta\nu = 20\text{ THz}$ ), measured with  $1064\text{ nm}$  pumping

A generous statement of the facts would be to just say, that *all* the reports of the Raman spectra and Raman gain coefficients were correct and the criticism leveled at this



work was incorrect. It was based on a lack of understanding by some glass groups of possible resonant enhancement of nonlinear susceptibilities, including the Raman one.

## CHAPTER SIX: TELLURITE FIBER PERFORMANCE - NUMERICAL ANALYSIS

Although the screening of the new glass samples for the material Raman gain coefficient is a vital part of this research, it only represents one parameter which is necessary in order to make accurate predictions regarding the performance of these new materials as a FRA (Fiber Raman Amplifier). Without obtaining any fiber devices during this program to experimentally characterize other important parameters such as a loss spectrum, dispersion spectrum, or Rayleigh scattering spectrum, it proves a challenge to speculate how well – or poorly – these new materials would compare to currently available FRAs based on silicates. In order to attempt an assessment, theory and literature searches for the important physical parameters have been made and used for a theoretical analysis of noise and performance under different conditions for the high gain tellurite fibers.

### 6.1 Background and Theory

The defining set of equations to analyze the overall Raman gain and OSNR performance for a FRA are listed below in Equation 6.1 [53].

$$\begin{aligned}
 \frac{dP_f(z, \nu)}{dz} &= -\alpha(\nu)P_f(z, \nu) + \gamma(\nu)P_b(z, \nu) \\
 &+ \int_{\zeta > \nu} \left\{ \frac{g_{RG}}{A_{eff}}(\nu - \zeta) [P_f(z, \zeta) + P_b(z, \zeta)] \cdot \left[ P_f(z, \nu) + 2h\nu \cdot \left( 1 + \frac{1}{e^{h(\nu - \zeta)/kT} - 1} \right) \right] \right\} \Delta\nu_B \\
 &- \int_{\zeta < \nu} \left\{ \frac{g_{RG}}{A_{eff}}(\nu - \zeta) [P_f(z, \zeta) + P_b(z, \zeta)] \cdot \left[ P_f(z, \nu) + 2h\nu \cdot \left( 1 + \frac{1}{e^{h(\nu - \zeta)/kT} - 1} \right) \right] \right\} \Delta\nu_B
 \end{aligned} \tag{6.1}$$

In Equation 6.1,  $P_f(z, \nu)$  is the power in the forward propagating wave at position  $z$  and with frequency  $\nu$ ,  $P_b(z, \nu)$  is the power in the backward propagating wave of the same frequency,  $\alpha(\nu)$  is a frequency dependent absorption coefficient,  $\gamma(\nu)$  is a frequency dependent Rayleigh scattering coefficient,  $g_{RG}(\nu - \zeta)$  is the material Raman gain coefficient between frequencies  $\nu$  and  $\zeta$ ,  $A_{eff}$  is the effective area between the optical waves at frequencies  $\nu$  and  $\zeta$ ,  $h$  is Planck's constant, the factor  $\left(1 + \frac{1}{e^{h(\nu-\zeta)/KT} - 1}\right)$  represents the thermal population factor whose presence is caused by a distribution of occupied energy states at temperature  $T$  (in degrees Kelvin) between the two energy states with frequencies  $\nu$  and  $\zeta$ ,  $\Delta\nu$  is the optical bandwidth seen at the detector, and  $K$  is Boltzmann's factor.

Traditionally, the numerical solution to Equation 6.1 has been avoided due to the need for significant computing power to solve the nonlinear coupled differential equations simultaneously. In order to provide quick (and often) accurate analysis, the power in each *signal* is analytically solved using the following equation:

$$P_s(L) = P_s(0) \exp\left(\sum_{pumps} g_{RG} L_{eff} I_{p0} - \alpha_s L\right) \quad (6.2)$$

$$L_{eff} = \frac{1 - \exp(-\alpha_p L)}{\alpha_p}$$

where  $I_{p0}$  is the input pump irradiance and  $L_{eff}$  is the effective interaction length of the pump and signal waves [9]. The art of summing up the pump contributions to the signal power works well for signal powers which remain very weak compared to the pump powers – i.e.  $P_p(z) \gg P_s(z)$ .

Equation 6.2 assumes the undepleted pump approximation, that is  $\alpha_p \gg g_{RG} I_S$ , so that one may only include loss to the strong pump wave as it propagates down the fiber. Taking the case of silica fibers with a typical loss coefficient of 0.2 dB/km, a peak Raman gain coefficient of  $\sim 10^{-13}$  m/W, average signal powers in the FRA of less than 0.1 mW, and effective areas on the order of  $20 \mu\text{m}^2$ , the undepleted pump approximation holds quite well yielding  $0.1 \gg 0.0005$  for  $\alpha_p \gg g_{RG} I_S$  of loss to the pump wave per kilometer of propagation. Once the solutions for signal powers at the output of the FRA have been established, the noise analysis also has some elegant analytical solutions which work well for low to medium gain FRAs and shorter fiber lengths in silica-based materials.

The solution for ASE powers at low to medium Raman gains and short fiber lengths uses the same approach as that used by Smith when deriving maximum power thresholds obtainable from typical Raman and Brillouin gain coefficients and spectra. Within the Smith treatment one can find the 3 dB noise limit of the ideal Raman amplifier, the disappearance of the 3 dB excess noise as the amplifier gain goes to zero, and a noise factor greater than 3 dB at elevated temperatures [54]. The approach used here is borrowed from Stolen [9].

The sum of the amplified signal and noise powers from the FRA are given by:

$$P_S(L) = P_S + P_N = [P_S(0) + P_N(0)] e^{g_{RG} I_{P0} L_{eff} - \alpha_S L} \quad (6.3)$$

where  $P_S$  and  $P_N$  are the signal and noise powers out of the amplifier,  $P_S(0)$  is the signal power into the amplifier,  $P_N(0)$  is the fictitious input noise power into an ideal noise-free amplifier, and  $I_{P0}$  is the pump irradiance into the amplifier.

The 3 dB noise figure of an ideal optical amplifier refers to a decrease by a factor of two in the ratio of electrical signal and noise powers after detection of the amplified optical signal by a noise-free detector. The detected current  $I$  is proportional to the total optical power  $P_S(L)$ ,

$$I = RP_S(L) \propto (E_S + E_N)^2, \quad (6.4)$$

where  $E_S$  and  $E_N$  are the signal and noise electric fields and  $R$  is the responsivity of the detector. The detected current will contain a signal current  $\sim E_S^2$  and two noise terms  $\sim 2E_S E_N$  and  $E_N^2$ . The noise terms are called the signal-spontaneous beat noise and the spontaneous-spontaneous beat noise. Normally the signal power is large enough that the signal-spontaneous beat noise is dominant and spontaneous-spontaneous noise terms are further cut by electrical filters.

The electrical signal power is  $I_S^2 R_L$  into a load resistor  $R_L$ . The noise power is the time averaged product of the total current minus the signal current squared into the load resistor  $R_L$ , or simply  $\langle (I - I_S)^2 \rangle R_L$ . The signal to noise ratio can now be defined as:

$$SNR = \frac{I_S^2}{\langle (I - I_S)^2 \rangle} = \frac{P_S^2}{4P_S P_N}. \quad (6.5)$$

Both the numerator and denominator of Equation 6.5 contain the amplification factor  $\exp(2g_{RG}I_{P0}L_{eff} - \alpha_S L)$ . The expression for the SNR then contains the signal power  $P_S(0)$  input to the amplifier and the effective input noise from Equation 6.3. By defining  $N_S$  as the number of noise photons and setting  $N_S = 1.0$  (the ideal noise input limit) the SNR takes on the form

$$SNR = \frac{P_S(0)}{4P_N} = \frac{P_S(0)}{4h\nu\Delta\nu_B}. \quad (6.6)$$

This SNR is compared to the SNR of an ideal shot noise limited detector,

$$SNR(\text{shot limit}) = \frac{P_S(0)}{2h\nu\Delta\nu_B}. \quad (6.7)$$

The factor of two difference between Equations 6.6 and 6.7 is the 3 dB excess noise of the ideal discrete Raman amplifier. The 3 dB excess noise disappears when the amplifier gain goes to zero as would happen when the pump is turned off. This can be seen from the term in the brackets in Equation 6.8,

$$N_S(L) = [1 - e^{-g_{RG}I_0L}] e^{g_{RG}I_0L} \quad (6.8)$$

where the fictitious noise input goes to zero and hence the output noise of the discrete FRA is in agreement with that of an ideal shot noise limited detector.

Raman amplifiers are often said to have a negative noise figure. This can happen because of the way the noise figure is defined when the transmission fiber is used as the Raman amplifier – a discrete Raman amplifier will have a positive noise figure which is greater than 3 dB.

The noise figure in dB can be defined as minus the log of the ratio of the SNR after the amplifier to the SNR that would be obtained using a fictitious ideal shot noise limited detector,

$$NF = -10 \log_{10} \frac{SNR(\text{amp})}{SNR(\text{shot limit})}. \quad (6.9)$$

Using Equations 6.6 and 6.7 the noise figure is  $10\log(2)$  or 3 dB. The excess noise of the discrete Raman amplifier will actually be greater than 3 dB because of the thermal excitation of the vibrational modes. This is given by the factor  $\left(1 + \frac{1}{e^{h(\nu-\zeta)/KT} - 1}\right)$ .

Inclusion of the thermal population factor modifies the noise figure (NF),

$$NF = 10 \log_{10} \left[ 2 \left( 1 + \frac{1}{e^{h(\nu-\zeta)/KT} - 1} \right) \right]. \quad (6.10)$$

For fused silica, the Raman gain peak is located near a frequency shift of 13.2 THz. Here the thermal population factor is 0.138 and the excess noise figure is approximately 3.6 dB. It should be noted that this simple treatment of the noise figure does not account for additional noise effects which are caused by Rayleigh scattering to be discussed later in this chapter.

The case is different when the transmission fiber is used as a backwards-pumped Raman amplifier (the usual case in practice). In this configuration, the signal will reach a minimum and then rise again because of the amplification which occurs mostly at the output end of the FRA. We define the signal minimum as the point in the FRA where the signal is weakest instead of at the input end,

$$SNR = \frac{P_S(L - L_{MIN})}{4h\nu\Delta\nu}, \quad (6.11)$$

where  $L_{MIN}$  is defined as the point in the fiber where the signal has minimum power. The noise figure for this configuration is obtained from the ratio of Equation 6.11 to the SNR of the detected output signal without amplification using an ideal shot noise limited detector,

$$NF = 10 \log_{10} \left( \frac{2P_S(L)}{P_S(L - L_{MIN})} \right) = 10 \log_{10} (2e^{-\alpha_S(L - L_{MIN})}), \quad (6.12)$$

where  $P_S(L)$  is the signal output power without any Raman amplification.  $P_S(L)$  and  $P_S(L - L_{MIN})$  are related through the loss in the fiber at the signal wavelength  $\alpha_S$ . In order to find the distance  $(L - L_{MIN})$ , one considers finding the point in the transmission fiber where the gain from Raman amplification equals the fiber loss at the signal wavelength

$$\alpha_S = g_{RG} I_{P0} e^{-\alpha_S (L - L_{MIN})} . \quad (6.13)$$

Here  $I_{P0}$  is the pump irradiance launched into the output end of the fiber (backward propagating with respect to the signal). For completeness, the losses at the pump and signal wavelengths are included along with the thermal occupation factor. After minor algebraic substitutions, the noise figure becomes

$$NF = 10 \log_{10} \left( \frac{2\alpha_S}{g_R I_{P0}} \right) = 10 \log_{10} \left[ 2 \left( 1 + \frac{1}{e^{h(\nu - \zeta)/kT} - 1} \right) \right] - \frac{\alpha_S}{\alpha_P} 10 \log_{10} \left( \frac{g_{RG} I_{P0}}{\alpha_S} \right). \quad (6.14)$$

As stated above, this noise figure does not account for additional noise effects which are caused by Rayleigh scattering which can be significant in distributed Raman amplifiers due to the long fiber lengths.

Rayleigh scattering occurs when an optical wave interacts with a particle that has a radial dimension which is much less than the wavelength of light. Depicted in Figure 6.1 is an example of an optical wave interacting with a random imperfection on the core/cladding interface of a waveguide. A similar argument for loss can be made for the interaction of the optical wave with a molecule which is part of the chemical composition of the waveguide.

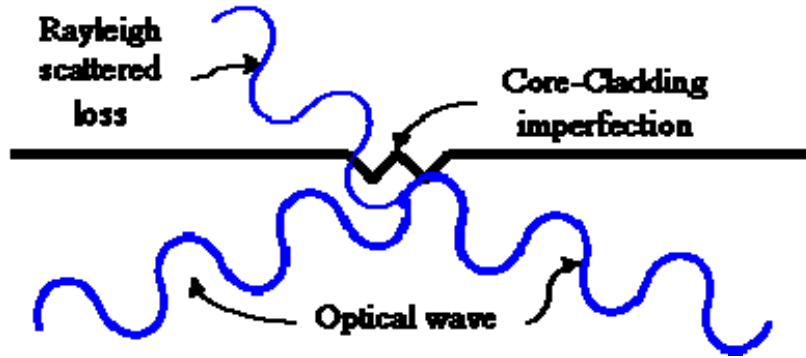


**Figure 6.1.** Rayleigh scattering of an optical wave due to an imperfection in a waveguide



This loss is not coupled back into a guided mode of the waveguide. Although power from the optical wave gets scattered in all directions, only the power that gets captured by a propagation mode supported by the optical fiber is of concern for the noise analysis of a FRA – the rest of the power that does not get coupled into a supported fiber mode exists in the guiding geometry as a leaky, non-guided mode and is treated as pure loss of signal power from the optical wave. Rayleigh scattering coefficients have been experimentally measured and reported for several different types of silica-based transmission fibers, with and without germanium doping and different effective areas, and typically they range from  $\gamma_R \sim 10^{-6} - 10^{-7} \text{ m}^{-1}$  in the S, C, and L-bands, as shown in Figure 6.2 [1].

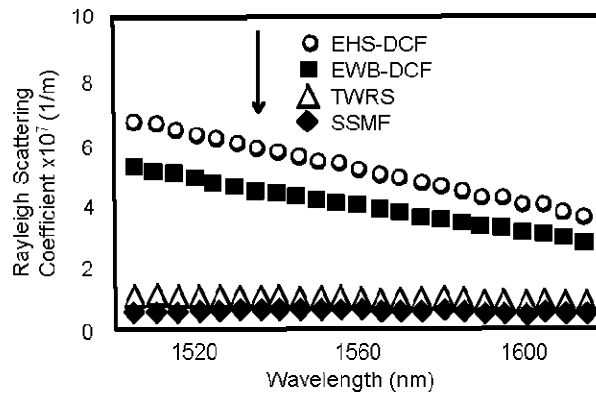


**Figure 6.2.** Rayleigh scattering coefficients for various silica-based FRAs [1]

There are two sources of noise which arise from Rayleigh scattering inside the FRA. The first source of noise is the double Rayleigh backscattering (DRS) of the signal itself, which leads to the phenomenon known as Rayleigh crosstalk [55,56]. The second source of noise – the one of primary concern in the performance evaluation of the FRA – is Rayleigh scattering of the ASE noise inside the FRA [57].

The effect of double Rayleigh scatter interference of the signal itself – known as Rayleigh crosstalk - on the performance of optical networks causes intensity noise on the signal after detection and that this causes a reduction in the receiver sensitivity. A bit-error rate floor is established because the DRS noise power in a FRA increases in proportion to the signal power. Using the approximation of constant gain per unit length in the gain fiber the OSNR due to DRS of the signal (in dB) at the output of an amplifying fiber is given in Equation 6.15 as

$$OSNR_{DRS} = -10 \log \left( \frac{k^2 L^2}{4(\ln G)^2} (G^2 - 2 \ln G - 1) \right), \quad (6.15)$$

where  $G$  is the *net* gain of the amplifying fiber,  $k$  is the Rayleigh backscatter per unit length, and  $L$  is the length of the gain fiber. Lewis et al. experimentally showed that Equation 6.15 holds well for reasonable net Raman gains in 9 km and 15 km silica-based fibers in the C-band [55]. They also demonstrated how employing a dual stage amplifier can greatly reduce the Rayleigh crosstalk penalty due to shorter fiber spans and less net Raman gain per fiber span [55]. The results in Figure 6.3 show minimum OSNR due to DRS of the signal of approximately 20 dB at relatively high net Raman gains approaching 30 dB for single stage amplifiers.

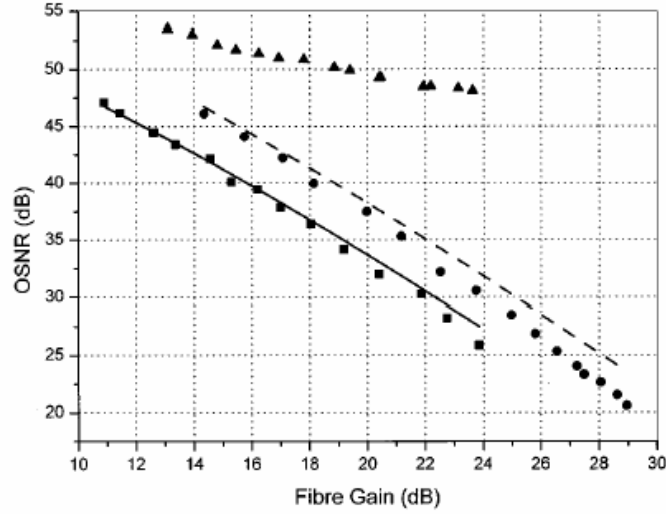


**Figure 6.3.** OSNR due to DRS of the signal at 1550 nm in a silica-based FRA. Circles + dotted line is a 9 km span, Squares + solid line is a 15 km span, triangles denote dual stage span with 9 km in each stage [55]

It should be noted that the value of Rayleigh crosstalk is simply the inverse of the OSNR due to DRS of the signal as stated in Equation 6.16

$$OSNR_{DRS} = 10 \log \left( \frac{P_{signal}}{P_{DRS}} \right) \tag{6.16}$$

$$\text{Rayleigh crosstalk} = 10 \log \left( \frac{P_{DRS}}{P_{signal}} \right)$$

It will be shown later in this chapter that Rayleigh crosstalk is not the limiting factor in terms of overall SNR of the FRA unless very long fiber spans are used or very high net Raman gains are desired.

Rayleigh scattering of the ASE poses the most severe threat to the OSNR in silica-based FRAs. For high net Raman gains, the ASE power inside the amplifier can become large enough through Raman amplification that Rayleigh scattering can start to couple the forward and backward traveling ASE waves. A theoretical plot of OSNR vs.

pump power inside silica-based FRAs, with and without Rayleigh scattering of the ASE, is depicted in Figure 6.4 [57].

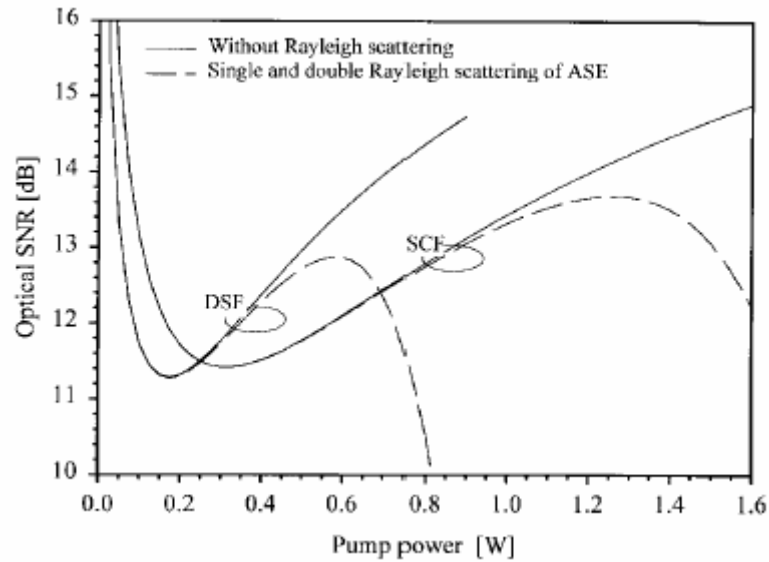


**Figure 6.4.** Theoretical predictions of OSNR in silica core fiber (SCF) and dispersion shifted fiber (DSF) when operated as a FRA [57]

For a given amount of net Raman gain inside the FRA, the ASE undergoes the same amount of Raman gain as the signal. Due to Rayleigh backscattering, part of the ASE power gets coupled into the backward propagating mode inside the fiber and experiences Raman gain in the reverse direction. As the net Raman gain of the signal increases, the single and double Rayleigh scattered ASE captured into propagating fiber modes experiences Raman gain along with the inherent forward propagating ASE. This increased total ASE noise power inside the fiber leads to a decreased OSNR as experimentally confirmed in both pure silica core transmission fiber (SCF) and germanium doped dispersion shifted fiber (DSF) in Figure 6.5 [57].

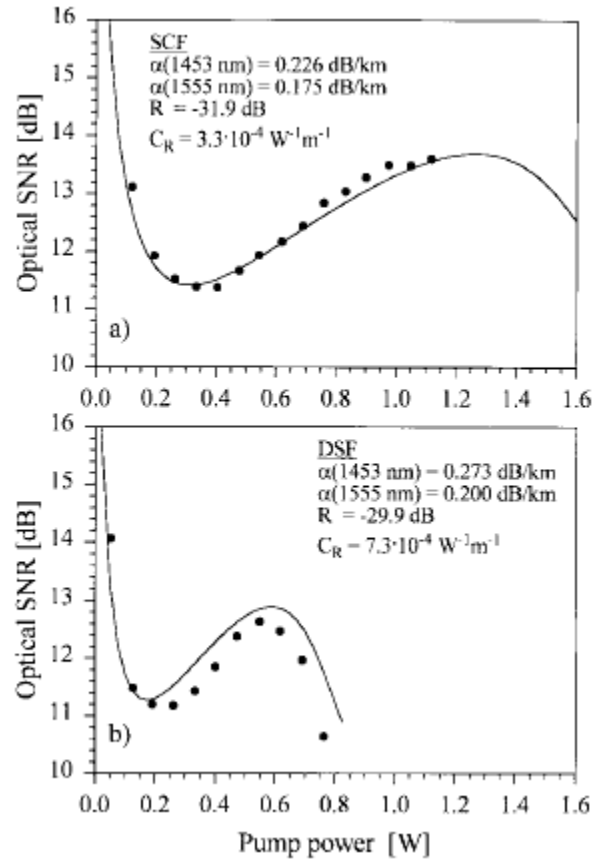


**Figure 6.5.** Theoretical (solid lines) and experimental results of OSNR inside SCF and DSF when operated as a FRA for various pump powers [57]

## 6.2 Application of Numerical Model

There exist a few publications by a Japanese group at NTT which has successfully drawn a tellurite glass composition into a fiber and performed tests to screen the performance as a FRA [25,52]. The published parameters from these experiments have enabled a numerical model to be written and used to compare the noise performance measurements of a potential tellurite based fiber as compared to a typical silica fiber. The most important parameters obtained from the tellurite FRA are an absorption coefficient and a small-signal Raman gain spectrum obtained from both a single pump

source and from a multi-wavelength bidirectional pumping scheme. Unfortunately, no Rayleigh scattering information on this composition or fiber geometry has been published, so theoretical calculations are needed to give reasonable approximations for the required Rayleigh scattering parameters. The small signal and multi-wavelength pumping results for the experimental fiber are used as verification that the numerical modeling is working properly. The goal of the following numerical model is to determine if high material Raman gain glasses can provide any advantage in an optical network system environment over the silica-based FRAs which are currently available.

The work of M. E. Lines was used in order to obtain the approximate Rayleigh scattering coefficient parameters for the tellurite composition [5]. The scattering losses  $\alpha(scat)$  can be recast in the form  $\alpha(scat) = B(scat)/\lambda^4$  to obtain a wavelength independent scattering amplitude. The value of  $B(scat)$  is scaled to 1  $\mu\text{m}$ . The sources of  $B(scat)$  are then decomposed into Rayleigh, Brillouin, and Raman components of the form  $B(scat) = B_\rho(Rayl) + B(Brill) + B(Ram)$ . Each component of  $B(scat)$  is then defined in terms of other parameters in Equation 6.17

$$\begin{aligned}
 B_\rho(Rayl) &= 5 \times 10^{-5} n^8 p^2(T_F) [K_T(T_F) - K_S(T_F)] T_F \\
 B(Brill) &= 5 \times 10^{-5} n^8 p^2(T) K_S(T) T \\
 B(Ram) &= 4\pi\lambda^4 \int_0^\infty \sigma_0(\omega_R) \coth\left(\frac{\hbar\omega_R}{KT}\right) d\omega_R
 \end{aligned} \tag{6.17}$$

where  $n$  is the refractive index (dimensionless),  $p$  is the photoelastic constant (dimensionless),  $T_F$  is the glass fixation temperature (in Kelvin),  $K_T$  and  $K_S$  are the static-isothermal and high-frequency adiabatic compressibilities (in units of  $10^{-12} \text{ cm}^2/\text{dyn}$ ),  $T$  is taken as room temperature or 300 Kelvin, and  $\sigma_0(\omega_R)$  is the Raman cross-section. An approximation is made that  $p(T_F) \sim p_{12}(T)$  where  $p_{12}(T)$  can be found from room

temperature Brillouin measurements.  $K_S(T)$  can also be found from room temperature Brillouin measurements and the approximation  $K_T(T_F) = 3K_S$  for  $T = 300$  Kelvin holds within 25% for most oxide glasses studied. Armed with these formulas, fused silica yields a value of  $B(scatter) = 0.69$  dB/km/ $(\mu\text{m})^4$ . Scaled to a carrier wavelength of  $1.55 \mu\text{m}$  a loss coefficient of  $0.12$  dB/km was calculated, which is remarkably close to that measured for current silica based fibers. Utilizing the formula for Rayleigh scattering loss  $B_\rho(Rayl)$  in Equation 8.16, a reasonable estimate for the Rayleigh scattering loss for tellurite glass near the C-band was obtained. Assuming an index of refraction of  $n = 2$ ,  $K_S(T) \sim 4.5$ ,  $p_{12} \sim 0.2$  [58], and a glass fixation temperature  $T_F \sim 700$  Kelvin yields a value of  $B_\rho(Rayl) = 3.22$  dB/km/ $(\mu\text{m})^4$ . Scaled to a carrier wavelength of  $1.55 \mu\text{m}$  a Rayleigh scattering coefficient  $\alpha(Rayl) = 0.56$  dB/km was finally estimated.

Although the Rayleigh scattering coefficient for the tellurite glass is now available, only a small fraction of the power lost due to Rayleigh scattering gets coupled into a supported guided mode of the FRA. Streckert et al showed the capture fraction of Rayleigh scattered light is given by

$$\eta = \frac{3\lambda^2}{8\pi n^2} (A_{eff})^{-1}, \quad (6.18)$$

which is identical to the result found later by Stolen regarding the capture fraction of spontaneous Raman emission being captured into a guided mode of a fiber [59,60]. For a tellurite fiber with an effective core area  $A_{eff} = 20 \mu\text{m}^2$  and a carrier wavelength of  $1.55 \mu\text{m}$ , a capture fraction of  $0.00358$  is obtained and used in the subsequent calculations.

With all of the necessary parameters available to perform the *projected* noise analysis of a tellurite FRA, the numerical model is described next and the simulation parameters are developed. The exact programming syntax is located in Appendix A.

In brief summary, the program allows any arbitrary material Raman gain curve to be input via text files. The Raman gain values are normalized to 1  $\mu\text{m}$  pumping to closely match the data taken from the Raman gain measurement apparatus described in Chapter 3. Any combination of pumps and signals can be input, regardless of wavelength, channel separation, or power. The pumps and signals are then propagated by directly solving the coupled nonlinear differential equations without using the undepleted pump approximation. For co-propagating pumps and signals, this is a simple task as ordinary differential equation (ODE) solvers are built into modern programming interpreters such as MATLAB. In the case of counter-propagating pumps (with respect to the signals) or bi-directionally pumped systems, the relatively simple problem of solving a one-point boundary value problem with an ODE solver becomes more complex by the need to now solve a two-point boundary value problem.

This is accomplished by assuming reasonable guesses for the final values of the counter-propagating pumps (effective “input” conditions to propagate the pump in the “forward” direction in the ODE solver) and then developing a relaxation routine to converge to the appropriate solution for the pump wave. The relaxation routine compares the answer the ODE solver supplies at the end of the fiber to the assumed input power of the pump by the user – these values are set to a tolerance level of less than 1% deviation in most cases. If the tolerance level is exceeded, the program adjusts the input conditions to the ODE solver (the final counter-propagating pump values) and solves the entire set of pump and signal waves once again. The relaxation routine once again compares output values from the fiber to the user-specified input pump powers for the counter-propagating pumps and repeats the process if the tolerance is exceeded. As an example,



given reasonable input guesses for pump values for a four pump (3 counter-propagating, one co-propagating) bidirectionally pumped, 50 channel tellurite FRA, convergence for pump values is calculated in less than 500 iterations which takes less than one minute on a 3.0 GHz Pentium 4 personal computer. Since reported tellurite FRAs usually are ~ 250 meters in length, the resolution of the pump and signal powers for these simulations are determined every meter, while silica-based fibers have solution sets with resolutions of 10 - 20 meters.

Once the solution for pump and signal powers is obtained, the noise analysis of the FRA can be determined. The two noise factors were solved for independently – that is, the OSNR due to double Rayleigh signal scattering was independently solved from the problem of OSNR degradation due to double Rayleigh scattering of the ASE.

For the case of OSNR degradation due to double Rayleigh signal scattering, the ASE source is set to zero in Equation 6.1 in order to determine precisely how much OSNR degradation is due to Rayleigh crosstalk. The solution of pump and signal powers along the length of the fiber is sent to the ODE routine, one step at a time, which numerically solves the forward and backward signal powers along the segment of the fiber. A two-point boundary value problem must be solved for each signal to be analyzed with the boundary conditions set as follows: *for the first segment*, the forward propagating Rayleigh scattered term is set to zero at the input of the fiber and a reasonable guess is made to the “output” of the backward propagating Rayleigh scattered term (the input condition to the ODE routine) along with the solution for pump and signal powers for the first segment in the solution set for the pumps and signals. The solution given by the ODE routine is then fed back into the ODE routine given the input

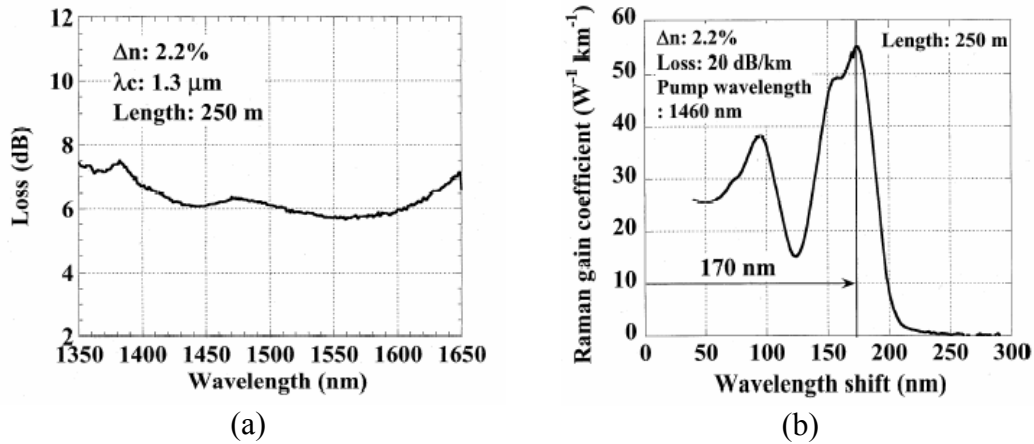
conditions for the noise terms and the new input pump and signal powers for the next segment of the fiber. For example, if the solution set for the pumps and signals in a tellurite FRA has 250 points (1 point for each meter of propagation), the ODE routine is called 250 times in order to obtain a final value for the effective “input” for the backward propagating Rayleigh scattered power. Once this effective “input” (output from the ODE) is found, it is compared to a threshold condition and the effective “output” (input to the ODE) to the *first* segment of fiber is adjusted accordingly. The tolerance on the boundary conditions is  $10^{-15}$  Watt which corresponds to  $\sim 10^5$  photons and much less than the input signal power  $\sim 10^{-6}$  Watt. For a FRA with numerous signal channels ( $< 20$ ), this process can take hours to converge to a solution, but it consistently converges. For a single channel and an arbitrary number of pumps, the process takes less than two minutes to converge to a solution.

In order to solve for the ASE related noise terms, the ODE routine and the ASE related noise terms are solved in a similar manner as the double Rayleigh signal noise powers. The threshold for the effective “input” of the backward traveling ASE noise terms is set to  $10^{-22}$  Watt, which is approximately two orders of magnitude smaller than the energy in one photon  $h\nu \sim 10^{-20}$  Watt – this sets a stringent boundary condition that the initial condition approximates zero. The input parameters for the calculations are presented in Table 6.1.

**Table 6.1.** Parameters used to obtain OSNR estimates for tellurite and silica FRAs

	Length (meters)	$A_{\text{eff}}$ ( $\mu\text{m}^2$ )	Loss (dB/km)	$g_{\text{RG}}$ ( $10^{-13}$ m/W) @ 1 $\mu\text{m}$ pump	$\Delta\nu$ (THz)	Rayleigh backscatter ( $\text{m}^{-1}$ )
Tellurite	250	20	20.4	43	21.3	$4 \times 10^{-6}$
Silica	7,000	20	0.2	1	13.2	$2.3 \times 10^{-7}$

Figure 6.6 (a) shows the absorption spectrum and Figure 6.6 (b) shows the small-signal Raman gain coefficient – defined in  $(W \cdot km)^{-1}$  in order to remove effective area considerations – for a well studied tellurite composition. The authors speculated that the peak Raman gain coefficient of this composition is 16 times higher than the material peak Raman gain coefficient of silica [25].



**Figures 6.6 (a) & (b).** Loss spectrum and small-signal Raman gain coefficient for composition  $78TeO_2 - 5ZnO - 12Li_2O - 5Bi_2O_3$  [25]

The parameters for the silica FRA were chosen to duplicate the amount of net Raman gain available for a given pump power. The effective area was kept at  $20 \mu m^2$  in order to ensure Rayleigh scattering between the two different materials was not affected by the  $(A_{eff})^{-1}$  dependence of captured Rayleigh scattered power by the fiber. In order to do this, the silica fiber was chosen to be a TrueWave<sup>®</sup> RS fiber from Lucent Technologies with the core size reduced to  $20 \mu m^2$  and the Rayleigh backscatter coefficient was increased accordingly. The results were obtained from near transparency for the silica fiber (negative gain for the tellurite fiber due to higher absorption) to

approximately 40 dB of net Raman gain (for the tellurite fiber). The results are shown in Figure 6.7.

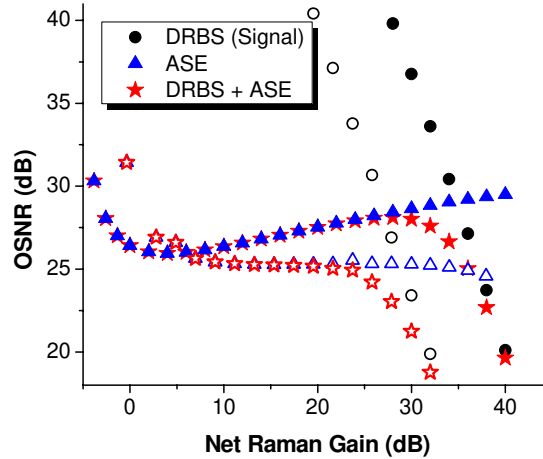


**Figure 6.7.** Theoretical improvement in OSNR of a tellurite FRA vs. silica FRA. Open symbols represent the silica FRA, filled symbols represent the tellurite FRA

In Figure 6.7, the triangular symbols represent the OSNR due to ASE and its double Rayleigh scattered powers, the circles represent the OSNR due solely to double Rayleigh signal scattering, and the stars represent the overall OSNR due to the combination of both noise sources. The silica FRA data are open symbols, while the tellurite FRA are filled symbols. The first conclusion that may be drawn is that the tellurite FRA shows a significant OSNR improvement at net Raman gains starting around 20 dB – at this Raman gain, almost a 3 dB OSNR improvement is projected with the tellurite composition. For the silica FRA, Rayleigh crosstalk becomes the most detrimental factor in the OSNR for a fiber length of only 7 km – most silica FRAs use fiber lengths longer than this in order to provide the appropriate dispersion compensation as well. This result also supports the notion that silica FRAs suffer from additional power penalty when operating above 20 dB of net Raman gain. Figure 6.8 is

experimental evidence that this is indeed the case with the silica FRA, and also provides some insight into the results obtained for the tellurite FRA.

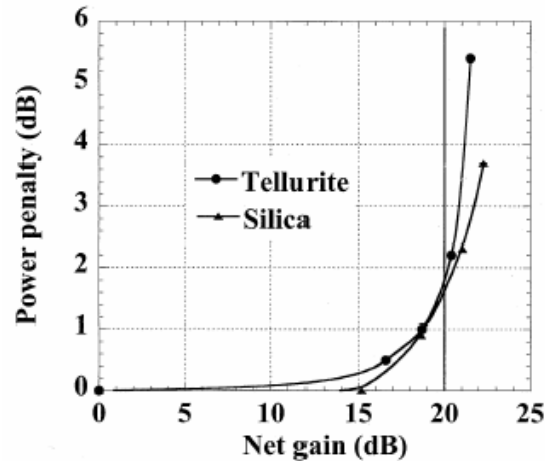


**Figure 6.8.** Power penalty for different amounts of net Raman gain for tellurite and silica FRAs [25]

It has been shown that the optical-signal-to-DRS ratio at the output of the Raman amplifier can be simply related to the receiver penalty. Figure 6.8 suggests that the experimental tellurite fiber suffers from much stronger Rayleigh scattering losses than used in the numerical model [25]. In silica-based fibers, it has been shown that the majority of loss when going to shorter wavelengths than the optical network wavelengths is caused by Rayleigh scattering, and the analysis employed by Lines provides a very reasonable formula that agrees well with experiments [5]. Silica fibers have also experienced decades of refinement in the manufacturing process in order to increase the purity of the material and reduce waveguide losses. Therefore, it is reasonable to speculate the experimental tellurite fiber suffers from additional scattering losses etc. and is not a function of the material parameters – more refinement in the manufacturing process is needed in order to validate this assumption.

### **6.3 *Considerations for Fiber Design Parameters***

No analytical solution exists in order to meet the design goals for a flat Raman gain signal profile with a given amount of net Raman gain from a FRA of these new materials. Since the Raman gain coefficients are significantly higher than fused silica, the proper design of a FRA needs to include the effects of higher frequency signal channels acting as pumps for lower frequency signal channels. The use of the undepleted pump approximation in simulations may yield significant differences from experimental results. It is recommended that the coupled nonlinear differential equations be solved numerically in order to properly simulate what a given net Raman gain profile will be.

## CHAPTER SEVEN: SUMMARY AND CONCLUSIONS

The contributions from this thesis have been instrumental, experimental and numerical. The overall goals as stated in the introduction, namely the direct measurement of Raman gain coefficients in new glasses, have been satisfied.

### ***7.1 Instrumentation Development***

A new experimental apparatus has been built which has made it possible to measure Raman gain directly in glass samples of millimeter thickness with a 1064 nm wavelength pump beam. This method has proven useful for absolute measurements of Raman gain. Subsidiary measurements of spontaneous Raman scattering were used to evaluate the depolarization ratio in the glasses as a function of wavelength. Although in principle this ratio could be measured with additional nonlinear optical measurements by rotating the plane of polarization of the incident beam, it proved more convenient to use the spontaneous Raman data.

In parallel, the theory of Raman gain has been extended to the nonlinear optical evaluation of Raman gain using pulsed lasers with weakly focused beams.

### ***7.2 Broadband Glasses***

In a search for glasses with better Raman gain properties than fused silica, this apparatus was used to characterize a variety of glass phosphate families. It was found that phosphate glasses give far superior bandwidths (up to a factor of five larger) than fused

silica (several THz). Bandwidths in excess of 40 THz were obtained in the glass family  $[(100-x)\text{NaPO}_3-x\text{Na}_2\text{B}_4\text{O}_7]:\text{TiO}_2/\text{Nb}_2\text{O}_5=1$  with  $x$  ranging for 5% to 13%. The spectral uniformity over this bandwidth was flat to  $\pm$  a few (1-2) dB and the Raman gain coefficient was 1.2 to 2.5 times that of fused silica.

Binary phosphate-niobate glasses in the family  $(100-x)\text{NaPO}_3 - x\text{Nb}_2\text{O}_5$  had gain spectral uniformity of  $\pm$  3dB with improved average Raman gain coefficients of order 3 - 10 times that of fused silica. Adding cations such as  $\text{Na}^+$ ,  $\text{K}^+$ ,  $\text{Ca}^{2+}$  and  $\text{Ba}^{2+}$  as modifiers of the glass matrix improved the peak Raman gain coefficients leading to values an order of magnitude larger than a fused silica, but with dominant Raman lines and poor gain uniformity.

In an effort to improve the uniformity of the Raman gain in such glasses, especially in the frequency shift region 11 - 15 THz where a dip frequently occurs, antimony in the form of  $\text{Sb}_2\text{O}_3$  was added to the phosphate glasses. In contrast to the observations made by spontaneous Raman scattering at a 633 nm pump wavelength, the direct NLO measurements of Raman gain did not find a corresponding improvement in the  $\Delta\nu = 11 - 15$  THz region. Although this potential discrepancy is not understood at this time, it may be that the Raman scattering experiments were performed too close to some antimony absorption feature.

### **7.3 Chalcogenide Glasses**

In response to reports of very large Raman gain coefficients a few hundred times that of fused silica measured in chalcogenide glass fibers, a number of chalcogenide glasses were investigated with the NLO apparatus. The best results were obtained in



18Ge – 5Ga – 7Sb – 70S glass which exhibited a peak Raman gain coefficient 70 times that of fused silica. Photodamage becomes a serious issue when selenium replaced the sulfur in such glasses so that only the peak gain coefficients could be measured in other glasses and the maximum coefficient found was 80 times fused silica in 18Ge – 5Ga – 7Sb–65S – 5Se.

#### **7.4 Tellurite Glasses**

Tellurite-based glass families are known to have very large third order nonlinear optical susceptibilities and it was found that they also had very large Raman gains. Several different families based on tellurite glass were investigated in order to determine the effect of adding a variety of highly polarizable constituents, for example additional Lewis  $ns^2$  lone pair species such as  $Tl^+$ ,  $Pb^{2+}$ , or  $Bi^{3+}$  and/or  $d^0$  ions such as  $Ti^{4+}$ ,  $Nb^{5+}$ , and  $W^{6+}$  to the tellurite glass. The presence of Lewis  $ns^2$  lone pair electrons in the electronic configuration, such as in the case of Te, Tl, and Pb, can also further enhance the nonlinear response of the material due to the strong coupling of the electric field to these free pairs of electrons. In fact, these families did exhibit the largest Raman gain coefficients of any oxide family investigated to date, 30 - 50 times that of the peak in fused silica.

The binary glass system  $(100-x)TeO_2 - xTlO_{0.5}$  was investigated with  $x = 20, 25, 30, 40,$  and  $50$ . For the composition  $50TeO_2 - 50TlO_{0.5}$  a peak Raman gain coefficient exceeding 50 times fused silica was measured. The replacement of some fraction of the thallium oxide by lead oxide increased the damage threshold of these glasses at the expense of a reduction of the Raman gain coefficient to 30 – 50 times that of fused silica,

depending on the concentration details. Yet another glass family formed by adding titanium oxide,  $(100-x-y)\text{TeO}_2 - x\text{TiO}_2 - y\text{TlO}_{0.5}$ , was investigated to determine how the spectral shape and intensity differed from the binary  $\text{TeO}_2 - \text{TlO}_{0.5}$  oxide glasses. The addition of  $\text{TiO}_2$  to the binary glass resulted in decreased Raman gain near  $\Delta\nu = 21.3$  THz but increased Raman gain near  $\Delta\nu = 13.5$  THz.

Additional investigations were performed on the glass family  $(100-x-y)\text{TeO}_2 - x\text{TiO}_2 - y\text{Bi}_2\text{O}_3$ . The  $\text{Bi}_2\text{O}_3$  was added since tellurite glass with  $\text{Bi}_2\text{O}_3$  has been shown to possess the highest values of  $n_2$  among all tellurite glass. These changes ultimately reduced the peak Raman gain coefficients down to the 25 - 30 times fused silica range. However, the gain uniformity was substantially improved to  $\pm 3$  dB over a bandwidth of  $\sim 24$  THz.

Raman gain measurements were also made on three tellurite glasses which incorporated only  $d^0$  ions, (a)  $85\text{TeO}_2 - 15\text{WO}_3$ , (b)  $85\text{TeO}_2 - 10\text{Nb}_2\text{O}_5 - 5\text{MgO}$ , and (c)  $90\text{TeO}_2 - 10\text{TiO}_2$ . Of these, (c) ( $90\text{TeO}_2 - 10\text{TiO}_2$ ) provides the highest peak Raman gain approaching  $(45 \pm 3) \times 10^{-13}$  m/W near the  $\Delta\nu = 20$  THz resonance.

In summary, for the tellurites, indeed these glasses had very large Raman gain coefficients with a peak value in the glass  $50\text{TeO}_2 - 50\text{TlO}_{0.5}$  about 52 times that of fused silica. Furthermore, discrepancies between Raman gain coefficients measured by spontaneous Raman scattering in the green region of the spectrum (515 nm) and by the apparatus developed here which operated with a pump wavelength of 1064 nm were resolved by showing that the green data were obtained for a resonantly enhanced Raman susceptibility.

## ***7.5 Numerical Simulations***

The Raman gain data for a specific tellurite glass was used as the model for numerical simulations of Raman amplification. Included in the computer modeling were linear loss; Raman gain with multiple pumps and signals; forward and/or backward propagating pump beams; forward, backward and double Rayleigh scattering; noise properties of amplifiers; excess noise, etc. This led to a comparison of the optical signal-to-noise ratio for different Raman gains in a tellurite and silica fiber. The first conclusion that may be drawn is that the tellurite FRA shows a significant OSNR improvement at net Raman gains starting around 20 dB – at this Raman gain, almost a 3 dB OSNR improvement is projected for the tellurite composition. For the silica FRA, Rayleigh crosstalk becomes the most detrimental factor in the OSNR for a fiber length of only 7 km – most silica FRAs use fiber lengths longer than this in order to provide the appropriate dispersion compensation as well. This modeling result also supports the notion that silica FRAs suffer from additional power penalty when operating above 20 dB of net Raman gain.

## ***7.6 Suggestions for the Future***

It appears that the possible glass families with most promise have now been scoped out. Some optimization of the glasses is still needed, primarily in the areas of spectral flatness of the Raman gain. The possibilities are very real that with glass engineering it might be possible to obtain very broad bandwidths with flatness of  $\pm 1$  dB

over spectral ranges of 40 THz. The trends already discussed in this work have certainly come close to this ideal making further optimization very promising.

The question of loss still needs to be addressed near 1550 nm for some of the broadband glass compositions. It does appear promising that low losses can be achieved, perhaps even approaching fused silica since the broadband glasses have absorption band edges at shorter wavelengths than the visible. But questions such as concentration fluctuations, which can lead to significant scattering losses, need to be addressed in such glasses.

The high gain glasses are promising for short haul applications such as “Raman in a box”. However again it is important to evaluate the limits on propagation loss.

But the biggest issue is whether high quality, reproducible fibers can be drawn from some of these exotic glasses. The pertinent glass parameters such as the temperature difference between the crystallization temperature ( $T_x$ ) and the glass transition temperature ( $T_g$ ) determines the thermal stability of the glass appear promising. It becomes the next crucial step to try making fibers from optimized glasses. This is the only way that some of the system issues associated with the actual applications of such fibers can be assessed.

## **APPENDIX A: COMPUTER CODE USED IN CHAPTER 6**

```

% Created by Robert Stegeman 02-23-2005

% Program to generate gain curve evolution for any glass
% This program uses any number of pump sources at random frequencies
% and DOES account for gain tilt
% This program requires two single column files
% One file should be named "gain.txt" and the other "shift.txt"
% "gain.txt" must have Raman gain values of (yy) x 10(-13) (m/W)
% "shift.txt" must have frequency values of (zz) THz
% *** EACH ROW OF GAIN.TXT AND SHIFT.TXT MUST CORRESPOND TO EACH OTHER
% *** THERE MUST BE NO BLAN K ROWS IN EITHER FILE
% These files need to be ASCII format
% The length of gain.txt and shift.txt are arbitrary
% The length of BOTH files must be identical

function [t,y] = RG4_DRS

clear all;
format long e;

Planck = 6.626e-34;
k_boltz = 1.38e-23;
Temp = 300;
dv = 100e9;
A1 = input('Enter the fiber effective area in microns (squared) >> ');
A = A1*10;
alpha1 = input('Enter the absorption coefficient in dB/km >> ');
alpha = alpha1/4.343/1000;

fiber_length = input('Enter the length of the fiber (meters) >> ');
step_size = 1;
num_of_chans = input('Enter the number of channels >> ');
input_chan_power = input('Enter the channel power (all channels will have identical input powers) (mW) >> ');
input_chan_power = input_chan_power*1e-3; % convert to Watts

for i=1:1:num_of_chans
    pc(i) = input_chan_power;
end

for i=1:1:num_of_chans
    input_chan_wavelength = input('Enter the wavelength of channel (in nanometers) >> ');
    wc(i) = input_chan_wavelength;
    fc(i) = 300000/wc(i);
end

num_of_pumps = input('Enter the number of pumps >> ');

for i=1:1:num_of_pumps
    input_pump_wavelength = input('Enter the wavelength of pump (in nanometers) >> ');
    wp(i) = input_pump_wavelength;
    fp(i) = 300000/wp(i);
    pump_direction = input('Enter 1 for co-propagating, enter 2 for counter-propagating >> ');
    pd(i) = pump_direction;
    input_pump_power = input('Enter the power for pump (mW) >> ');
    pp(i) = input_pump_power/1000;
    target_pump(i) = pp(i);
    if pd(i) ~= 1
        pp(i) = target_pump(i)/100 *i;
    end
end

num_of_signals = num_of_pumps + num_of_chans;

for i=1:1:num_of_pumps
    freq(i) = fp(i);
end

for i=num_of_pumps+1:1:num_of_signals
    freq(i) = fc(i - num_of_pumps);
end

```

```

for i=1:1:num_of_pumps
    power(i) = pp(i);
    wavelength(i) = wp(i)/1000;
    alpha(i) = alpha/wavelength(i);
end

for i=num_of_pumps+1:1:num_of_signals
    power(i) = pc(i-num_of_pumps);
    wavelength(i) = wc(i-num_of_pumps)/1000;
    % alpha(i) = alpha/wavelength(i);
    pd(i) = 1;
end

for i=1:1:num_of_signals
    y0(i) = power(i);
    S(i) = 3*((wavelength(i)*1e-6)^2)/8/pi/(1.46)^2/(A1*1e-12);
    % alpha(i) = alpha2
end

gain = importdata('silicagain.txt','t');
shift = importdata('silicashift.txt','t');
length = numel(shift);
gain(length + 1) = 0;
shift_end = shift(length);
shift_begin = shift(1);
shift_spacing = (shift_end - shift_begin)/length;

for chan=1:1:num_of_signals
    for j=1:1:num_of_signals
        h=0;
        gain_shift(chan,j) = length + 1;
        gain_minus(chan,j) = 0;
        gain_plus(chan,j) = 0;
        noise_minus(chan,j) = 0;
        noise_plus(chan,j) = 0;
        if chan ~= j
            freq_shift(chan,j) = abs(freq(chan) - freq(j));
            for k=1:1:length
                if h == 0
                    if (freq_shift(chan,j) - shift(k)) < shift_spacing
                        gain_shift(chan,j) = k;
                        h = 1;
                    end
                end
            end
        end
        if freq(chan) > freq(j)
            gain_minus(chan,j) = -freq(chan)/freq(j)*gain(gain_shift(chan,j))/A/1.8/wavelength(chan);
            noise_minus(chan,j) =
            gain_minus(chan,j)*1.8*Planck*freq(j)*1e12*(1+1/(exp(1e12*freq_shift(chan,j)*Planck/k_boltz/Temp)-1))*dv;
        end
        if freq(chan) < freq(j)
            gain_plus(chan,j) = gain(gain_shift(chan,j))/A/1.8/wavelength(chan);
            noise_plus(chan,j) =
            gain_plus(chan,j)*1.8*Planck*freq(chan)*1e12*(1+1/(exp(1e12*freq_shift(chan,j)*Planck/k_boltz/Temp)-1))*dv;
        end
    end
end
end
% gain_shift
% gain_minus(1,2)
% gain_plus(1,2)
% noise_plus(1,2)
% noise_minus(1,2)

noise = 0;
on_off = 0;
tspan = linspace(1,fiber_length,fiber_length/step_size);
for j=1:1:num_of_signals
    for i=1:1:fiber_length/step_size

```

```

        y_power(i,j) = 0;
    end
end
loop = 1;
end_loop = 0;
do_loop = 0;
pe = 0;
DRS = 0;
while loop <= 5000 && end_loop ~= 1
    options = odeset('Vectorized','on'); %Set options
    [t,y] =
ode45(@f,tspan,y0,options,noise,alpha,num_of_signals,gain_plus,gain_minus,noise_minus,noise_plus,pd,on_off,num_of_pumps,y_p
ower,dv,S,fiber_length,DRS); % Call solver
    for i=1:1:num_of_pumps
        y01(i) = y0(i);
        if pd(i) == 2
            pump_error(loop,i) = y(numel(y(:,1)),i) - target_pump(i);
            if abs(pump_error(loop,i)) > target_pump(i)*0.002 % 2e-3 tolerance
                y0(i) = y0(i)*exp(-pump_error(loop,i)/(i^1.22));
            end
            do_loop(i) = y01(i) - y0(i);
            pe(loop,i) = (target_pump(i) + pump_error(loop,i))/target_pump(i)*100;
        else pe(loop,i) = 100;
        end
    end
    pump_loop=[sum(do_loop) loop]
    loop = loop + 1;
    if sum(do_loop) == 0
        end_loop = 1;
    end
end
end

% numel(y(:,1));

for i=1:1:numel(y(:,1))
    for j=1:1:num_of_signals
        y1(i,j) = y(i,j); % vector for pumps and channels
        gain_input(i,j) = 10*log10(y1(i,j)/y1(1,j));
        if j <= num_of_pumps
            yp(i,j) = y1(i,j)*1000;
        else y2(i,j-num_of_pumps) = y1(i,j); % net power vector for channels only !!
        end
    end
end

for i=1:1:num_of_pumps
    final_pump(i) = yp(numel(y1(:,1)),i);
end
num_of_loops = loop-1;

on_off = 1;
options = odeset('Vectorized','on'); %Set options
[t,y] =
ode45(@f,tspan,y0,options,noise,alpha,num_of_signals,gain_plus,gain_minus,noise_minus,noise_plus,pd,on_off,num_of_pumps,y_p
ower,dv,S,fiber_length,DRS); % Call solver

for j=1:1:num_of_signals
    for i=1:1:numel(y1(:,1))
        y3(i,j) = y(i,j); % on-off vector for pumps and channels
    end
end

for j=1:1:num_of_chans
    for i=1:1:numel(y1(:,1))
        y4(i,j) = y3(i,j+num_of_pumps); % on-off net power vector for channels only !!
        gain_onoff(i,j) = 10*log10(y2(i,j)/y4(i,j)); % on-off gain signals
        gain1(i,j) = 10*log10(y2(i,j)/y2(1,j)); % net gain for pumps and signals
    end
end
end

```



```

10*log10(y2(numel(y1(:,1)),:)/y2(1,:))
pause(1);

DRS_input_noise = 5.2688e-4;
DRS_target_noise = 1e-15;           % about 1% of average photon energy

for i=1:1:num_of_pumps
    if pd(i) == 1
        y0_temp(i) = 0;
        pd_temp(i) = 1;
    else y0_temp(i) = target_pump(i)/1e5*i;
        pd_temp(i) = 2;
    end
end

k = 1;
y0(k) = 0;
pd(k) = 1;
y0(k+1) = 2.566014839782771e-008;
pd(k+1) = 2;
k=k+2;

% for i=1:1:num_of_pumps
%   for j=1:1:2
%       if j == 1
%           pd(k) = pd_temp(i);
%           y0(k) = y0_temp(i);
%           k=k+1;
%       end
%       if j == 2
%           if pd(k-1) == 1
%               pd(k) = 7.830215688117210e-005;
%               k=k+1;
%           else pd(k) = 1;
%               y0(k) = 0;
%               k=k+1;
%           end
%       end
%   end
% end
factor=[1.377970735458501e-009 3.300591520341234e-005 2.564028382320702e-003 4e-002 6.163767186142804e-004];
noise_factor=[4.9e-20];
for i=1:1:num_of_chans
    pd(k) = 1;
    y0(k) = 0;
    pd(k+1) = 2;
    y0(k+1) = factor(i);
    k=k+2;
end
y0=y0;

DRS = 1;
on_off = 2;
DRS_loop = 1;
DRS_end_loop = 0;
do_loop_DRS = 0;
alpha = alpha./10;
gain_plus = gain_plus./10;
noise_plus = noise_plus./10;
tspan = linspace(1,step_size,10);
DRS_loop_end = 1000;
DRS_signal_threshold = 1e-8;
while DRS_loop <= DRS_loop_end && DRS_end_loop == 0
    nl = 1;
    while nl <= numel(y1(:,1))
        for j=1:1:num_of_signals
            y_power(j) = y1(nl,j);
        end
        for j=1:1:2*num_of_signals
            DRS_input(nl,j) = y0(j);
        end
    end
end

```

```

end
options = odeset('Vectorized','on'); %Set options
[t,y] =
ode45(@f,tspan,y0,options,noise,alpha_num_of_signals,gain_plus,gain_minus,noise_minus,noise_plus,pd,on_off,num_of_pumps,y_p
ower,dv,S,fiber_length,DRS); % Call solver
for j=1:1:2*num_of_signals
    y0(j) = y(numel(y(:,1)),j);
    y_DRS(nl,j) = y(numel(y(:,1)),j);
end
nl = nl + 1;
end
for i=2*num_of_pumps+1:1:2*num_of_signals
    do_loop_DRS(i) = 0;
    y0_DRS(DRS_loop,i) = DRS_input(1,i);
end
for i=1:1:2*num_of_pumps
    if pd(i) == 1
        y0(i) = y0_DRS(1,i);
    else DRS_error(DRS_loop,i) = y_DRS(numel(y1(:,1)),i);
        if abs(DRS_error(DRS_loop,i)) > DRS_target_noise
            if abs(DRS_error(DRS_loop,i)) > 1e-3
                if DRS_error(DRS_loop,i) < 0
                    y0(i) = y0_DRS(DRS_loop,i)*1.05;
                else y0(i) = y0_DRS(DRS_loop,i)/1.05;
                end
            else y0(i) = y0_DRS(DRS_loop,i)*exp(-DRS_error(DRS_loop,i)*1e2);
            end
            else y0(i) = DRS_input(1,i);
            end
            DRS_ne1(DRS_loop,i) = (DRS_target_noise + DRS_error(DRS_loop,i))/DRS_target_noise*100;
            do_loop_DRS(i) = abs(y0_DRS(DRS_loop,i) - y0(i));
        end
    end
    for i=2*num_of_pumps+1:1:2*num_of_signals
        if pd(i) == 1
            y0(i) = y0_DRS(1,i);
        else DRS_error(DRS_loop,i) = y_DRS(numel(y1(:,1)),i);
            if abs(DRS_error(DRS_loop,i)) > DRS_target_noise
                if abs(DRS_error(DRS_loop,i)) > DRS_signal_threshold
                    if DRS_error(DRS_loop,i) < 0
                        y0(i) = y0_DRS(DRS_loop,i)*1.05;
                    else y0(i) = y0_DRS(DRS_loop,i)/1.05;
                    end
                end
            elseif i == 4
                y0(i) = y0_DRS(DRS_loop,i)*exp(-DRS_error(DRS_loop,i)*1e7);
            else y0(i) = y0_DRS(DRS_loop,i)*exp(-DRS_error(DRS_loop,i)*5e7);
            end
            else y0(i) = DRS_input(1,i);
            end
            DRS_ne1(DRS_loop,i) = (DRS_target_noise + DRS_error(DRS_loop,i))/DRS_target_noise*100;
            do_loop_DRS(i) = abs(y0_DRS(DRS_loop,i) - y0(i));
        end
    end
    % for i=1:1:2*num_of_pumps
    % y0(i) = y0_DRS(1,i);
    % end
    DRS_noise_loop=[sum(do_loop_DRS) DRS_loop];
    if sum(do_loop_DRS) == 0 && DRS_loop > 1
        DRS_end_loop = 1;
        noise_inputs = [pd; DRS_input(1,:)];
    end
    DRS_loop

ii = 1;
for i=1:1:2*num_of_signals
    if pd(i) == 2
        DRS_iteration(ii) = y0(i);
        DRS_error_iteration(ii) = DRS_error(DRS_loop,i);
        ii = ii + 1;
    end
end

```

```

end

iteration_DRS = [DRS_iteration; DRS_error_iteration]
% iteration1 = [y0; noise_error(loop_noise,:)]
DRS_loop = DRS_loop + 1;
end

k = 1;
DRS_start = 1;
for j=1:1:numel(y(1,:))
    for i=DRS_start+1:1:DRS_loop
        if y0(j) ~= 0
            DRS_ne(i-DRS_start,k) = DRS_ne1(i-DRS_start,j);
        end
    end
    k=k+1;
end

% noise_factor=[1.853000336219660e-007 1.470704458239012e-006 9.009603919383367e-006 2.275341691692313e-005
4.991491603919993e-006];

for i=1:1:2*num_of_pumps
    y0(i) = 0;
end

k = 2*num_of_pumps+1;
for i=1:1:num_of_chans
    y0(k)=0;
    y0(k+1)=noise_factor(i);
    k=k+2;
end

DRS = 0;
noise = 1;
loop_noise = 1;
loop_noise_loop = 1000;
end_loop_noise = 0;
target_noise = 1e-22;
while loop_noise <= loop_noise_loop && end_loop_noise == 0
    nl = 1;
    while nl <= numel(y1(:,1))
        for j=1:1:num_of_signals
            y_power(j) = y1(nl,j);
        end
        for j=1:1:2*num_of_signals
            y0_input(nl,j) = y0(j);
        end
        options = odeset('Vectorized','on'); %Set options
ode45(@f,tspan,y0,options,noise,alpha,num_of_signals,gain_plus,gain_minus,noise_minus,noise_plus,pd,on_off,num_of_pumps,y_p
ower,dv,S,fiber_length,DRS); % Call solver
        for j=1:1:2*num_of_signals
            y0(j) = y(numel(y(:,1)),j);
            y_noise(nl,j) = y(numel(y(:,1)),j);
        end
        nl = nl + 1;
    end
    for i=1:1:2*num_of_signals
        do_loop_noise(i) = 0;
        y01(loop_noise,i) = y0_input(1,i);
    end
    for i=2*num_of_pumps+1:1:2*num_of_signals
        if pd(i) == 1
            y0(i) = y0_input(1,i);
        else noise_error(loop_noise,i) = y_noise(numel(y1(:,1)),i);
            if abs(noise_error(loop_noise,i)) > target_noise
                if noise_error(loop_noise,i) < 0
                    if abs(noise_error(loop_noise,i)) > 1e-10
                        y0(i) = y01(loop_noise,i)*1.1;
                    else y0(i) = y01(loop_noise,i)*exp(-noise_error(loop_noise,i)*1e12); % make "larger"
                end
            end
        end
    end
end

```

```

        end
    end
    if noise_error(loop_noise,i) > 0
        if abs(noise_error(loop_noise,i)) > 1e-10
            y0(i) = y01(loop_noise,i)/1.1;
        else y0(i) = y01(loop_noise,i)*exp(-noise_error(loop_noise,i)*1e12); % make "smaller"
        end
    end
    else y0(i) = y0_input(1,i);
    end
    ne1(loop_noise,i) = (target_noise + noise_error(loop_noise,i))/target_noise*100;
    do_loop_noise(i) = abs(y01(loop_noise,i) - y0(i));
end
end
for i=1:1:2*num_of_pumps
    y0(i) = y0_input(1,i);
end
noise_loop=[sum(do_loop_noise) loop_noise];
if sum(do_loop_noise) == 0 && loop_noise > 1
    end_loop_noise = 1;
end
end
loop_noise

ii = 1;
for i=2*num_of_pumps+2:2:2*num_of_signals
    y0_iteration(ii) = y0(i);
    noise_error_iteration(ii) = noise_error(loop_noise,i);
    ii = ii + 1;
end

noise_iteration = [y0_iteration; noise_error_iteration]
% iteration1 = [y0; noise_error(loop_noise,:)]
loop_noise = loop_noise + 1;
end
num_of_noise_loops = loop_noise-1
% summation=[y01(:,:); noise_error(:,:)]
% y(numel(y(:,1)),:)

% ne = 50;
k = 1;
ne_start = 1;
for j=2*num_of_pumps+1:1:numel(y(1,:))
    for i=ne_start+1:1:loop_noise
        if y0(j) ~= 0
            ne(i-ne_start,k) = ne1(i-ne_start,j);
        end
    end
    end
    k=k+1;
end
for j=1:1:2*num_of_signals
    for i=ne_start:1:loop_noise-1
        if y0(j) ~= 0
            ne(i,k) = ne1(i,j);
        end
    end
    end
    k=k+1;
end
end

for i=1:1:numel(y1(:,1))
    k = 1;
    for j=1:1:num_of_signals
        noise_power1(i,j) = y_noise(i,k) + y_noise(i,k+1);
        DRS_noise_power1(i,j) = y_DRS(i,k) + y_DRS(i,k+1);
        k=k+2;
    end
end
end

for j=1:1:num_of_chans
    for i=1:1:numel(y1(:,1))
        noise_power(i,j) = noise_power1(i,j+num_of_pumps);
    end
end

```

```

        noise_power_dbm(i,j) = 10*log10(noise_power(i,j)/1e-3);
        DRS_noise_power(i,j) = DRS_noise_power1(i,j+num_of_pumps);
        DRS_noise_power_dbm(i,j) = 10*log10(DRS_noise_power(i,j)/1e-3);
    end
end
for j=1:1:num_of_pumps
    for i=1:1:numel(y1(:,1))
        DRS_noise_power_pump(i,j) = DRS_noise_power1(i,j);
        DRS_noise_power_pump_dbm(i,j) = 10*log10(DRS_noise_power(i,j)/1e-3);
    end
end
% noise_power(numel(y1(:,1)),:)

for j=1:1:num_of_chans
    for i=1:1:numel(y1(:,1))
        SNR_ASE(i,j) = 10*log10(y2(i,j)/noise_power(i,j));
        DRS_SNR(i,j) = 10*log10(y2(i,j)/DRS_noise_power(i,j));
        SNR_total(i,j) = 10*log10(y2(i,j)/(noise_power(i,j)+DRS_noise_power(i,j)));
    end
end

% final_pump = final_pump'
pump_power=[pp(1)*1000; final_pump]
inputs=[y0_DRS(DRS_loop-1,4); y01(loop_noise-1,4)]
power_info=[y2(numel(y1(:,1)),:); 10*log10(y2(numel(y1(:,1)),:)/y2(1,:)); noise_power(numel(y1(:,1)),:);
DRS_noise_power(numel(y1(:,1)),:)]
SNR_info=[SNR_ASE(numel(y1(:,1)),:); DRS_SNR(numel(y1(:,1)),:); SNR_total(numel(y1(:,1)),:)]
num_of_loops
pump_info = [num_of_loops final_pump]
final_pump

fiber = linspace(1,fiber_length,numel(y1(:,1)));
fiber = fiber.';
% size(yp)
% size(y2)
p=linspace(wc(1),wc(num_of_chans),num_of_chans);
if pe ~= 0
    loop_plot=linspace(1,loop,numel(pe(:,1)));
    loop_plot = loop_plot.';
end
loop_plot_noise=linspace(ne_start,loop_noise-1,(numel(ne(:,1))));
loop_plot_noise = loop_plot_noise.';
% size(pe)
% size(loop_plot)

% figure;
% plot(fiber,yp(:,:));
% xlabel('Fiber length (meters)');
% ylabel('Pump power (mW)');
% legend('p1','p2','p3','p4');
%
% if num_of_pumps ~= 1
%     if num_of_pumps == 1 && pd(1) == 1
%         k=1;
%     else figure;
%         plot(loop_plot,pe(:,:));
%         axis tight;
%         xlabel('Iteration');
%         ylabel('Pump Percent accuracy');
%         legend('p1','p2','p3','p4');
%     end
% end

% figure;
% plot(loop_plot_noise,ne(:,:));
% xlabel('Iteration');
% ylabel('ASE noise percent accuracy');
%
% figure;

```

```

% plot(loop_plot_noise,ne(:,:));
% axis([ne_start numel(ne(:,1)) -1000 1000]);
% xlabel('Iteration');
% ylabel('Signal Percent accuracy (zoomed)');
% legend('1','2','3','4','5');
%
% figure;
% plot(fiber.gain1(:,:));
% xlabel('Fiber length (meters)');
% ylabel('Gain (dB)');
% % legend('s1','s2','s3','s4','s5','s6','s7','s8','s9','s10');
% % legend('1','2','3','4','5','6','7','8','9','10','11','12','Location','South');
%
% figure;
% plot(fiber.gain_onoff(:,:));
% xlabel('Fiber Length (meters)');
% ylabel('On-Off gain (dB)');
%
% figure;
% plot(fiber.y2(:,:));
% xlabel('Fiber length (meters)');
% ylabel('Signal power');
% % legend('s1','s2','s3','s4','s5','s6','s7','s8','s9','s10');
%
% figure;
% grid on;
% mesh(p.fiber.gain1(:,:));
% xlabel('Wavelength (nm)');
% ylabel('Fiber length (meters)');
% zlabel('Gain (dB)');
% view(0,90);
%
% figure;
% grid on;
% mesh(p.fiber.gain1(:,:));
% xlabel('Wavelength (nm)');
% ylabel('Fiber length (meters)');
% zlabel('Gain (dB)');
%
% figure;
% plot(p.gain1(numel(y1(:,1)),:),'o-');
% xlabel('Wavelength (nm)');
% ylabel('Gain (dB)');
%
% figure;
% plot(p.gain_onoff(numel(y1(:,1)),:),'o-');
% xlabel('Wavelength (nm)');
% ylabel('On-off gain (dB)');
%
% figure;
% plot(p.noise_power_dbm(fiber_length,:),'o-');
% xlabel('Wavelength (nm)');
% ylabel('Noise power (dBm)');
% % %
% figure;
% %
semilogy(fiber.noise_power(:,1),fiber.noise_power(:,2),fiber.noise_power(:,3),fiber.noise_power(:,4),fiber.noise_power(:,5),'o',fiber,n
oise_power(:,6),'o',fiber.noise_power(:,7),'o',fiber.noise_power(:,8),'o');
% plot(fiber.noise_power_dbm(:,:));
% xlabel('Fiber length (m)');
% ylabel('Noise power (dBm)');
% legend('1','2','3','4','5','Location','Best');
%
% figure;
% plot(fiber.DRS_SNR(:,:));
% ylabel('SNR (dB)');
% xlabel('Fiber length (m)');
% %
% figure;
% plot(p.DRS_SNR(numel(y1(:,1)),:),'o-');

```

```

% ylabel('SNR at output (dB)');
% xlabel('Wavelength (nm)');
%
% figure;
% plot(fiber,SNR_total(:,:));
% ylabel('SNR (dB)');
% xlabel('Fiber length (m)');
% %
% figure;
% plot(p,SNR_total(numel(y1(:,1)),:),'o-');
% ylabel('SNR at output (dB)');
% xlabel('Wavelength (nm)');

% -----
% Here we solve define the differential equations
% -----

function dydt =
f(t,y_noise,alpha,num_of_signals,gain_plus,gain_minus,noise_minus,noise_plus,pd,on_off,num_of_pumps,y_power,dv,S,fiber_length,
DRS)

power_transfer = zeros(1,size(y,2));

if on_off == 0
    for chan=1:1:num_of_signals
        power_transfer(chan) = 0;
        for j=1:1:num_of_signals
            if chan ~= j
                if chan < j
                    power_transfer(chan) = power_transfer(chan) + gain_minus(chan,j)*y(j,:);
                else power_transfer(chan) = power_transfer(chan) + gain_plus(chan,j)*y(j,:);
                end
            end
        end
        if pd(chan) == 1
            dydt(chan,:) = y(chan,)*(-alpha + power_transfer(chan));
        else dydt(chan,:) = y(chan,)*(alpha - power_transfer(chan));
        end
    end
end

if on_off == 1
    for chan=num_of_pumps+1:1:num_of_signals
        power_transfer(chan) = 0;
        for j=num_of_pumps+1:1:num_of_signals
            if chan ~= j
                if chan < j
                    power_transfer(chan) = power_transfer(chan) + gain_minus(chan,j)*y(j,:);
                else power_transfer(chan) = power_transfer(chan) + gain_plus(chan,j)*y(j,:);
                end
            end
        end
        if pd(chan) == 1
            dydt(chan,:) = y(chan,)*(-alpha + power_transfer(chan));
        else dydt(chan,:) = y(chan,)*(alpha - power_transfer(chan));
        end
    end
end

if noise ~= 0
    for chan=1:1:num_of_signals
        power_transfer(chan) = 0;
        noise_transfer_plus(chan) = 0;
        for j=1:1:num_of_signals
            if chan ~= j
                if chan < j
                    % power_transfer(chan) = power_transfer(chan) + gain_minus(chan,j)*y1(:,j);
                    % noise_transfer_minus(chan) = noise_transfer_minus(chan) + noise_minus(chan,j)*y1(:,chan);
                    else power_transfer(chan) = power_transfer(chan) + gain_plus(chan,j)*y_power(j);
                    noise_transfer_plus(chan) = noise_transfer_plus(chan) + noise_plus(chan,j)*y_power(j);
                end
            end
        end
    end
end

```

```

        end
    end
end
end
end
% power_transfer
% noise_transfer_plus

chan = 1;
for i=1:1:num_of_signals
    if pd(chan) == 1
        dydt(chan,:) = -alpha*y(chan,:) + power_transfer(i)*y(chan,:) + noise_transfer_plus(i) + 2.3e-6*y(chan+1,:);
        dydt(chan+1,:) = -1*(-alpha*y(chan+1,:) + power_transfer(i)*y(chan+1,:) + noise_transfer_plus(i) + 2.3e-6*y(chan,:));
        chan = chan + 2;
    else dydt(chan,:) = -1*(-alpha*y(chan,:) + power_transfer(i)*y(chan,:) + noise_transfer_plus(i) + 2.3e-6*y(chan+1,:));
        dydt(chan+1,:) = -alpha*y(chan+1,:) + power_transfer(i)*y(chan+1,:) + noise_transfer_plus(i) + 2.3e-6*y(chan,:);
        chan = chan + 2;
    end
end
end
end

if DRS ~= 0
    for chan=1:1:num_of_signals
        power_transfer1(chan) = 2.3e-6*y_power(chan);
        power_transfer(chan) = 0;
        for j=1:1:num_of_signals
            if chan ~= j
                if chan > j
                    power_transfer(chan) = power_transfer(chan) + gain_plus(chan,j)*y_power(j);
                end
            end
        end
    end
end
end
% power_transfer
% noise_transfer_plus

chan = 2*num_of_pumps+1;
for i=num_of_pumps+1:1:num_of_signals
    if pd(chan) == 1
        dydt(chan,:) = -alpha*y(chan,:) + power_transfer(i)*y(chan,:) + 2.3e-6*y(chan+1,:);
        dydt(chan+1,:) = -1*(-alpha*y(chan+1,:) + power_transfer(i)*y(chan+1,:) + 2.3e-6*y(chan,:) + power_transfer1(i));
        chan = chan + 2;
    else dydt(chan,:) = -1*(-alpha*y(chan,:) + power_transfer(i)*y(chan,:) + 2.3e-6*y(chan+1,:));
        dydt(chan+1,:) = -alpha*y(chan+1,:) + power_transfer(i)*y(chan+1,:) + 2.3e-6*y(chan,:) + power_transfer1(i);
        chan = chan + 2;
    end
end
end
end
end

```



## LIST OF REFERENCES

- [1] <http://www.lucent.com/press/0501/010529.nsb.html>
- [2] M. Islam, “*Raman Amplifiers for Telecommunications 2: Sub-Systems and Systems*” (Springer, 2004)
- [3] M. E. Lines, “Absolute Raman intensities in glasses: I. Theory”, *Journal of Non-Crystalline Solids* **89**, 143–162 (1987)
- [4] M. E. Lines, “Absolute Raman intensities in glasses: II. Germania-based heavy metal oxides and global criteria”, *Journal of Non-Crystalline Solids* **89**, 163–180 (1987)
- [5] M. E. Lines, “Raman-gain estimates for high-gain optical fibers”, *Journal of Applied Physics* **62**, 4363-4370 (1987)
- [6] A. E. Miller, K. Nassau, K. B. Lyons, and M. E. Lines, “The intensity of Raman scattering in glasses containing heavy metal oxides”, *Journal of Non-Crystalline Solids* **99**, 289–307 (1988)
- [7] M. E. Lines, “Scattering losses in optic fiber materials. I. A new parametrization”, *Journal of Applied Physics* **55**, 4052–4057 (1984)
- [8] M. E. Lines, “Scattering losses in optic fiber materials. II. Numerical estimates”, *Journal of Applied Physics* **55**, 4058–4063 (1984)
- [9] M. Islam, “*Raman Amplifiers for Telecommunications 1: Physical Properties*” (Springer, 2004)
- [10] [http://www.mpbcc.ca/raman\\_pump/raman\\_oem.html](http://www.mpbcc.ca/raman_pump/raman_oem.html)
- [11] R. Stolen, private communication

- [12] F.L. Galeener, J.C. Mikkelsen, Jr., R.H. Geils, and W. J. Mosby, "The relative Raman cross sections of vitreous SiO<sub>2</sub>, GeO<sub>2</sub>, B<sub>2</sub>O<sub>3</sub>, and P<sub>2</sub>O<sub>5</sub>", Applied Physics Letters **32**, 34-36 (1978)
- [13] Z. Pan, S. H. Morgan, and B. H. Long, "Raman scattering cross-sections and non-linear optical response of lead borate glasses", Journal of Non-Crystalline Solids, **185**, 127-134 (1995)
- [14] R. Stegeman, L. Jankovic, H. Kim, C. Rivero, G. Stegeman, K. Richardson, P. Delfyett, Y. Guo, A. Schulte, T. Cardinal, "Tellurite glasses with peak absolute Raman gain coefficients up to 30 times that of fused silica", Optics Letters **28**, 1126-1128 (2003)
- [15] G. Dai, F. Tassone, A. Li Bassi, V. Russo, C.E. Bottani, F. D'Amore, "TeO<sub>2</sub>-based glasses containing Nb<sub>2</sub>O<sub>5</sub>, TiO<sub>2</sub>, and WO<sub>3</sub> for discrete Raman fiber amplification", Photonics Technology Letters **16**, 1011-1013 (2004)
- [16] C. Rivero, K. Richardson, R. Stegeman, G. Stegeman, T. Cardinal, E. Fargin, M. Couzi, V. Rodriguez, "Quantifying Raman Gain Coefficients in Tellurite Glasses", Journal of Non-Crystalline Solids **345&346**, 396-401 (2004)
- [17] R.E. Slusher, G. Lenz, J. Hodelin, J. Sanghera, L.B. Shaw, and I.D. Aggarwal, "Large Raman gain and nonlinear phase shifts in high-purity As<sub>2</sub>Se<sub>3</sub> chalcogenide fibers", Journal Optical Society of America B **21**, 1146-1155 (2004)
- [18] R. Stegeman, C. Rivero, K. Richardson, G. Stegeman, P. Delfyett, Y. Guo, A. Pope, A. Schulte, T. Cardinal, P. Thomas, and J-C Champarnaud-Mesjard, "Raman gain measurements of thallium-tellurium oxide glasses", Optics Express **13**, 1144-1149 (2005)

- [19] C. Rivero, K. Richardson, R. Stegeman, G. Stegeman, T. Cardinal, E. Fargin, and M. Couzi, “Characterization of the Performance Parameters of Some New Broadband Glasses for Raman Amplification”, *Glass Technology* **46**, 80-84 (2005)
- [20] V.G. Plotnichenko, V. V. Koltashev, V. O. Sokolov, E. M. Dianov, I. A. Grishin and M. F. Churbanov, “Raman band intensities of tellurite glasses”, *Optics Letters* **30**, 1156-1158 (2005)
- [21] G. Senthil Murugan, T. Suzuki, and Y. Ohishi, “Tellurite glasses for ultrabroadband fiber Raman amplifiers”, *Applied Physics Letters* **86**, 161109–161111 (2005)
- [22] C. Rivero, R. Stegeman, D. Talaga, M. Couzi, T. Cardinal, K. Richardson, and G. Stegeman, “Resolved discrepancies between visible spontaneous Raman cross-section and direct near-infrared Raman gain measurements in TeO<sub>2</sub>-based glasses”, *Optics Express* **13**, 4759-4769 (2005)
- [23] R.H. Stolen and E.P. Ippen, “Raman gain in optical waveguides”, *Applied Physics Letters* **22**, 276-278 (1973)
- [24] D. Mahgerefteh, D. L. Butler, J. Goldhar, B. Rosenberg, and G. L. Burdge, “Technique for measurement of the Raman gain coefficient in optical fibers”, *Optics Letters* **21**, 2026-2028 (1996)
- [25] A. Mori, H. Masuda, K. Shikano, and M. Shimizu, “Ultra-wide-band tellurite-based fiber Raman amplifier, *Journal of Lightwave Technology* **21**, 1300-1306 (2003)

- [26] R. Stegeman, C. Rivero, G. Stegeman, K. Richardson, P. Delfyett, L. Jankovic, and H. Kim, "Raman gain measurements in bulk glass samples", *Journal Optical Society of America B* **22**, 1861-1867 (2005)
- [27] M.E. Lines, "Influence of d orbitals on the nonlinear optical response of transparent transition-metal oxides", *Physical Review B* **43**, 11978-11990 (1991)
- [28] T. Cardinal, K. A. Richardson, H. Shim, A. Schulte, R. Beatty, K. Le Foulgoc, C. Meneghini, J. F. Veins, and A. Villeneuve, "Non-linear optical properties of chalcogenide glasses in the system As-S-Se", *Journal of Non-Crystalline Solids* **256&257**, 353-360 (1999)
- [29] J. M. Harbold, F. Ö. Ilday, F. W. Wise, and B. G. Aitken, "Highly nonlinear Ge-As-Se and Ge-As-S-Se glasses for all-optical switching", *Photonics Technology Letters* **14**, 822-824 (2002)
- [30] M. Dutreilh-Colas, P. Thomas, J.C. Champarnaud-Mesjard, and E. Fargin, "New TeO<sub>2</sub> based glasses for nonlinear optical applications: study of the Tl<sub>2</sub>O – TeO<sub>2</sub> – Bi<sub>2</sub>O<sub>3</sub>, Tl<sub>2</sub>O – TeO<sub>2</sub> – PbO, and Tl<sub>2</sub>O – TeO<sub>2</sub> – Ga<sub>2</sub>O<sub>3</sub> systems", *Physics and Chemistry of Glasses* **44**, 349-352 (2003)
- [31] R. W. Hellwarth, "Theory of stimulated Raman scattering", *Physical Review* **130** 1850-1852 (1963)
- [32] F. A. Hopf and G. I. Stegeman, in *Applied Classical Electrodynamics, Volume 2: Nonlinear Optics*, (Wiley Interscience, New York, 1986)
- [33] F. A. Hopf and G. I. Stegeman, in *Applied Classical Electrodynamics, Volume 1: Linear Optics*, (Wiley Interscience, New York, 1986)

- [34] C. Rivero, "High gain/broadband oxide glasses for next generation Raman amplifiers", PhD Thesis, University of Central Florida (2005)
- [35] R.W. Boyd, "Nonlinear Optics", (Academic Press, Elsevier Science, USA, 1992)
- [36] Y.R. Shen, "The Principles of Nonlinear Optics", (John Wiley & Sons, Inc., 1984)
- [37] D. Heiman, R.W. Hellwarth, and D.S. Hamilton, "Raman scattering and nonlinear refractive index measurements of optical glasses", *Journal of Non-Crystalline Solids* **34**, 63-79 (1979)
- [38] Y. Kato and H. Takuma, "Absolute Measurement of Raman-Scattering Cross Sections in Liquids", *Journal Optical Society of America* **61**, 347-350 (1971)
- [39] Y. Kato and H. Takuma, "Experimental Study on the Wavelength Dependence of the Raman Scattering Cross Sections", *Journal of Chemical Physics* **54**, 5398-5402 (1971)
- [40] F. Yoshino, S. Polyakov, G.I. Stegeman, and M. Liu, "Nonlinear Refraction and Absorption from 1300 to 2200 nm in Single Crystal Polymer poly [bis (p-toluene sulfonate)] of 2, 4-hexadiyne-1, 6-diol (PTS)", *Quantum Electronics and Laser Science QELS Postconference Digest, QTuG43* (2003)
- [41] R. H. Stolen, J. P. Gordon, W. J. Tomlinson, and H. A. Haus, "Raman response function of silica-core fibers", *Journal Optical Society of America B* **6**, 1159-1166 (1989)
- [42] <http://www.ekspla.com/en/main/products/en/main/products/17/19?PID=18>
- [43] <http://www.ekspla.com/en/main/products/en/main/products/17/21?PID=441>
- [44] <http://www.newport.com/Optics/Beamsplitters/1/3546/product.aspx>

- [45] <http://www.jobinyvon.com/usadivisions/OSD/legacymonos.htm>
- [46] <http://www.judsontechnologies.com/germanium.htm>
- [47] T. Cardinal, E. Fargin, G. Le Flem, and S. Leboiteux, “Correlation between structural properties of Nb<sub>2</sub>O<sub>5</sub>-NaPO<sub>3</sub>-Na<sub>2</sub>B<sub>4</sub>O<sub>7</sub> glasses and non-linear optical activities”, *Journal of Non-Crystalline Solids* **222**, 228-234 (1997)
- [48] T. Sekiya, N. Mochida, A. Ohtsuka, and M. Tonokawa, “Raman spectra of MO<sub>1/2</sub> – TeO<sub>2</sub> (M = Li, Na, K, Rb, Cs and Tl) glasses”, *Journal of Non-Crystalline Solids*, **144**, 128-144 (1992)
- [49] J. F. Baugher and P. J. Bray, “\_\_\_”, *Physics and Chemistry of Glasses* **10** (1969)
- [50] A. Berthereau, E. Fargin, A. Villezusanne, R. Olazcuaga, G. Le Flem, and L. Ducasse, “Determination of Local Geometries around Tellurium in TeO<sub>2</sub>-Nb<sub>2</sub>O<sub>5</sub> and TeO<sub>2</sub>-Al<sub>2</sub>O<sub>3</sub> Oxide Glasses by XANES and EXAFS: Investigation of Electronic Properties of Evidenced Oxygen Clusters by Ab Initio Calculations”, *Journal of Solid State Chemistry* **126**, 143-151 (1996)
- [51] L.A. Farrow and E.M. Vogel, “Raman spectra of phosphate and silicate glasses doped with the cations Ti, Nb and Bi”, *Journal of Non-Crystalline Solids* **143**, 59-64 (1992)
- [52] A. Mori, H. Masuda, K. Shikano, K. Oikawa, K. Kato, and M. Shimizu, “Ultra-wideband tellurite-based Raman fibre amplifier”, *Electronics Letters* **37**, 1442-1443 (2001)
- [53] H. Kidorf, K. Rottwitt, M. Nissov, M. Ma, and E. Rabarijaona, “Pump interactions in a 100-m bandwidth Raman amplifier”, *Photonics Technology Letters* **11**, 530-532 (1999)

- [54] R. G. Smith, "Optical power handling capacity of low loss optical fibers as determined by stimulated Raman and Brillouin scattering", *Applied Optics* **11**, 2489-2494 (1972)
- [55] M. Nissov, K. Rottwitt, H. D. Kidorf, and M. X. Ma, "Rayleigh crosstalk in long cascades of distributed unsaturated Raman amplifiers", *Electronics Letters* **35**, 997-998
- [56] S. A. E. Lewis, S. V. Chernikov, and J. R. Taylor, "Characterization of double Rayleigh scatter noise in Raman amplifiers", *Photonics Technology Letters* **12**, 528-530 (2000)
- [57] P. B. Hansen, L. Eskildsen, A. J. Stentz, T. A. Strasser, J. Judkins, J. J. DeMarco, R. Pedrazzani, and D. J. DiGiovanni, "Rayleigh scattering limitations in distributed Raman pre-amplifiers", *Photonics Technology Letters* **10**, 159-161 (1998)
- [58] <http://www.newlightphotonics.com/teo2.html>
- [59] J. Streckert and F. Wilczewski, "Relationship between nonlinear effective core area and backscattering capture fraction for a single mode optical fiber", *Electronics Letters* **32**, 760-762 (1996)
- [60] R. H. Stolen, "Relation between the effective area of a single-mode fiber and the capture fraction of spontaneous Raman scattering", *Journal Optical Society of America B* **19**, 498-501 (2002)